KINETICS AND REVERSIBILITY OF PHASE TRANSFORMATIONS IN GROUP IVA ALLOY ANODES FOR SODIUM-BASED BATTERIES

ZHANG JIA

PhD

The Hong Kong Polytechnic University

2025

The Hong Kong Polytechnic University
Department of Electrical and Electronic Engineering

Kinetics and Reversibility of Phase Transformations in Group IVA Alloy Anodes for Sodium-based Batteries

Zhang Jia

A thesis submitted in partial fulfilment of the
requirements for the degree of Doctor of Philosophy

August 2024

CERTIFICATE OF ORIGINALITY

I hereby declare that this thesis is my own work and that, to the best of my knowledge and belief, it reproduces no material previously published or written, nor material that has been accepted for the award of any other degree or diploma, except where due acknowledgment has been made in the text.

___________________________________(Signed)

__________ZHANG Jia_______________(Name of student)

Abstract

Group IVA alloy elements i.e., Si, Ge, Sn, and Pb, have attracted great attention in SIBs due to their interesting sodium capability. However, their electrochemical performance, pertaining to both thermodynamics and kinetics, remains poorly understood. Herein this thesis systematically investigated sodiation-induced phase transformations in IVA alloy anodes using robust electrochemical and structural characterization techniques, aimed at shedding light on the mechanism and kinetics of electrochemically driven phase transformations, as well as important capacity degradation mechanisms.

The first part examined the sodiation of Si thin film electrodes. Common approaches including increasing temperature, incorporating other elements, and creating a porous structure are employed to enable Na insertion into Si, but the reversible capacity of Si is still limited. The unfavorable sodiation could be associated with poor electrical conductivity, sluggish kinetics, narrow interstitial space, weak silicon/sodium atomic interactions. Given such multifaceted challenges, further research in this direction was de-prioritized in favor of exploring other IVA elements.

The second part studied the mechanisms and kinetics of phase transformations in the initial sodiation of Ge electrodes. The sodiation of Ge is found to be kinetically limited. The higher-ordered phases such as Na_3Ge can form under kinetically favorable conditions (at higher temperatures or lower C-rates). Two-phase potentiostatic measurements reveal that the transformation of Ge to $NaGe_4$ proceeds by a one-dimension model and is controlled by diffusion whereas the rate-determining step for the $NaGe_4$/$Na_{1+x}Ge$ transformation is the reaction speed. Arrhenius methods are employed to investigate the temperature dependence on both phase transformations, giving activation energies of ~50 $kJ \cdot mol^{-1}$ and ~70 $kJ \cdot mol^{-1}$, respectively. Two schematic models are proposed to elucidate the sodiation mechanism of Ge.

The third part explored the (de-)sodiation kinetics of Sn foil electrodes by in-situ impedance technique. With the help of distribution of relaxation time (DRT) tools, we found that the cell impedance is dominated by diffusion and charge transfer resistance at low sodiation depth (i.e., DoD), whereas at high sodiation depth, the charge transfer resistance is dominant. Based on the frequency-dependent impedance imaginary part, the sodium diffusivity in Na_xSn is extracted to be 10^{-12}~10^{-18} $cm^2 \cdot s^{-1}$. Meanwhile, the diffusivity value is much lower at low DoDs than at high DoDs. These results indicate the transformations between the low-order Na-Sn phases are likely limited by diffusion and/or charge transfer kinetics, while the rate-determining steps for the high-order Na-Sn phase transformations are charge transfer.

The final part evaluated the reversibility of phase transformations in Pb foil electrodes comprehensively. The sodiation of Pb foils undergoes four phase transformations (Pb/$NaPb_3$, $NaPb_3$/Na_9Pb_4, Na_9Pb_4/$Na_{15}Pb_4$), which yields a specific capacity of ~460 mAh·g^{-1} (~1167 mAh·L^{-1}). When pursuing fully reversible capacities, the electrode stops functioning after only 3-4 cycles largely due to electrode physical damage. Further reversibility examination of each phase transformation indicates that the fastest capacity loss occurs in the NaPb/Na_9Pb_4 transformation, which is consistent with the observed structural damage (i.e., crack, voids). By bypassing this problematic phase transformation using a partial cycling protocol, the stability of Pb foil anodes is improved, giving 20 cycles with 85% capacity retention.

Table of Contents

Acknowledgments

I have experienced many difficult times during my Ph.D study, and I acknowledge that I could not have gone so far without the support and help of different people and parties.

Firstly, I am thankful to my research and thesis advisor, Prof. Steven BOLES from NTNU, for providing me with a lot of help and guidance during the whole Ph.D. study. His rich expertise and experience in the battery field inspired me a lot, especially when I was in a difficult time. Also, I appreciate Prof. BOLES for offering me an opportunity to do the research in his battery lab. The 5-month exchange study at NTNU not only enriched my life but also made me realize the significance of communicating and cooperating with researchers from different fields. Furthermore, I am grateful to my present chief supervisor Prof. Wei JIN for his help and respect for my research, and for providing me with financial support to do research after the thesis submission. Besides, many thanks to my co-supervisors Dr. Kwok-ho LAM, and Prof. Eric CHENG for their suggestions on my future career.

Secondly, I would like to express my deepest gratitude to Dr.Tianye ZHENG, not only for his patient guidance and enormous assistance in my research work, but also for his kindness, and encouragement, and for sharing with me many unforgettable memories. As a newcomer in the battery area, I was a bit lost and had no idea how to choose my research projects at the beginning of the Ph.D study. Dr ZHENG was so nice to teach me how to use the lab instruments and offered me many suggestions on the research project design. Also, during the research, Dr. ZHENG was always willing to discuss with me whenever I encountered problems and taught me the way of thinking, and how to resolve the problem utilizing the resources around me, which benefited me a lot. Meanwhile, his experience and understanding of electrochemical fundamentals and battery materials inspired me a lot. Except for his help in this research, he also taught me how to give a good presentation, how to develop story-telling ability, and how to deal with academic papers. Indeed, without his assistance, I could not complete my Ph.D studies smoothly, and my academic skills, logical thinking, and problem-solving abilities could not have been improved. Additionally, I thank him for his care as a good friend in my life, such as offering me advice on career development and reminding me of work-life balance.

Thirdly, I am truly grateful to my family for their unconditional support and care whenever what happens. Without their backup, I could not persist so far. Also, many thanks to my dear friends, Hui XIAO, Yang WANG, Rongxiang WANG, and Fan YANG, for comforting me when I feel pressured, encouraging me when I was frustrated, and giving me advice when I feel lost.

Lastly, I would like to express my gratitude to The Hong Kong Polytechnic University and NTNU (Norway), for offering me advanced instruments and financial support to explore the unknown.

List of Journal Papers

This thesis is based on the following papers on sodium-based systems, which are referred to in the text listed below.

1. **Jia Zhang**, Tianye Zheng, Eric Ka-wai Cheng, Kwok-ho Lam, Steven Boles, "Insights into the Sodiation Kinetics of Si and Ge Anodes for Sodium-Ion Batteries." Journal of The Electrochemical Society, 170.10 (2023): 100518. (**Chapters 3 and 4**)

   My contribution: I discussed the experimental plan with the supervisors and co-workers. I prepared the Si and Ge thin films using the magnetic sputtering method. I made coin cells, conducted electrochemical measurements and electrode material characterization, and analyzed the experimental results. I wrote the manuscript and revised it with the co-authors' input.

2. **Jia Zhang**, Tianye Zheng, Xiaoyang Guo, Hung Quoc Nguyen, Ka-wai Eric Cheng, Kwok-ho Lam, Daniel Rettenwander, Wei Jin, Steven Boles, "Identifying Problematic Phase Transformations in Pb Foil Anodes for Sodium-ion Batteries", Journal of The Electrochemical Society, accepted. (**Chapter 6**)

   My contribution: I preliminarily proposed the idea, made the experimental plan, and modified it after the discussion with the supervisors. I am also responsible for the assembly of half and full cells, the electrochemical measurements, electrode material characterization (using ex-situ XRD and SEM techniques), as well as the analysis of the experimental results. I wrote the manuscript and revised it with the co-authors' input.

3. **Jia Zhang**, Tianye Zheng, Eric Ka-wai Cheng, Kwok-ho Lam, Wei Jin, Steven Boles, "Understanding the Kinetic Limitation of Tin Foil Electrode for Sodium-ion Batteries by in-situ Electrochemical Impedance Spectroscopy", in preparation. (**Chapter 5**)

   My contribution: I preliminarily proposed the idea and made the experimental plan under the guidance of the supervisors. I made the three-electrodes cells for the in-situ impedance measurements to distinguish the impedance of the working electrode and characterized the electrode materials by ex-situ x-ray diffractometer and scanning electron microscopy. Also, I applied the distribution relaxation time technique for the interpretation of the impedance data, wrote the paper draft and revised it according to the co-worker's suggestions.

Papers Not Included in This Thesis

The electrochemical knowledge (particularly kinetic-related) in sodium-based systems is also extended to lithium-based systems, which results in the following publications.

1. **Jia Zhang**, Tianye Zheng, Kwok-ho Lam, Steven Boles, “Design considerations and cycling guidance for aluminum foil anodes in lithium-ion rechargeable cells.” Electrochimica Acta 456 (2023), 1424372.

   My contribution: I discussed the experimental results with the supervisors, and adjusted the experimental plan based on these results. I assembled the coin cells (half and full cells), did the galvanostatic measurements (e.g., GITT, GCD, EIS), and characterized the electrode composition. I also processed all the experimental data, plotted them, and analyzed these results. I wrote the manuscript and revised it with the co-authors’ input.

2. Tianye Zheng, **Jia Zhang**, Xiaoyang Guo, Wei Jin, Steven Boles , Unlocking room temperature formation of Li-rich phases in aluminum anodes for Li-ion batteries. Electrochimica Acta, 485 (2024), 144127.

   My contribution: I made the cells, conducted the electrochemical measurements, and did the electrode material characterization. I was involved in the discussion of experimental design and the result analysis.

3. Tianye Zheng, **Jia Zhang**, Wei Jin, Steven Boles, “Utilization of Li-rich phases in aluminum anodes for improved cycling performance through strategic thermal control”. ACS Applied Energy Materials, 6.3 (2023): 1845-1852.

   My contribution: I made the cells, conducted the electrochemical measurements, and did the electrode material characterization. I was involved in the discussion of experimental design and results analysis. I also reviewed the manuscript throughout the whole process.

List of abbreviations

ESSs	Energy Storage Systems
EV	Electrical Vehicle
PABs	Pb-acid Batteries
LIBs	Lithium-ion Batteries
SIBs	Sodium-ion Batteries
LFP	$LiFePO_4$
GCD	Galvanostatic Charge-Discharge
ICA	Incremental Capacity Analysis
EIS	Electrochemical Impedance Spectroscopy
CA	Chronoamperometry
DRT	Distribution Relaxation Time
EC	Ethylene Carbonate
DMC	Dimethyl carbonate
PC	Propylene Carbonate
NVP	$Na_3V_2(PO_4)_3$
PVDF	Polyvinylidene difluoride
NMP	N-Methyl-2-pyrrolidone
XRD	X-ray Diffraction
SEM	Scanning Electron Microscopy
DoD	Depth of Discharge
SoC	State of Charge
SEI	Solid Electrolyte Interface
CE	Coulombic Efficiency

Chapter 1: Literature Review

1. 1 Background

The growing environmental concerns (e.g., release of greenhouse gases and particular matters) and the exhaustion of fossil fuels drive the development of sustainable energy technologies, such as wind turbines, hydropower plants, and solar panels, etc [1]. A recent survey shows that the electricity generated from renewable sources, notably wind and photovoltaic, will reach up to 8300 TWh in 2021, roughly 30% of the total energy, which is expected to increase to 57% worldwide by 2030 so as to control the temperature rise below 2 degrees [2]. Although the deployment of these energy technologies greatly mitigates the dependence on the hydrocarbon energy source and thus reduces their environmental impacts, they face a major challenge of intermittence: the electricity production from renewable energy strongly depends on natural conditions (e.g., sunshine or wind). For instance, the electricity generation from solar panels can be kept at a nominal level only at noon but is inefficient at night; wind turbines produce less electricity in calm weather [3]. This intermittent feature of renewable energy resources can hardly guarantee a stable supply of electricity for households. As a result, energy storage systems (ESSs) are designed for storing and converting renewable energy to balance electricity generation and supply for different uses [2, 4].

Since the first introduction of ESSs in the early 19th century, a broad range of energy storage technologies has been developed, including thermal, mechanical, magnetic, electrical, and electrochemical energy storage systems [5]. Thanks to high energy efficiency, electrochemical energy storage and conversion systems (e.g., capacitor, battery, and fuel cell), which utilize reversible electrochemical reactions to store or convert chemical energy in the form of electrical energy, have attracted the greatest attention and have been widely applied in portable electronic, electrical/hybrid vehicle and stationary storage applications [6]. The following sub-session aims to briefly introduce the basic characteristics or different properties of the primary electrochemical energy storage technologies and their application.

1.1.1 Electrochemical Energy Storage Technology

Electrochemical capacitors, batteries, and fuel cells are the predominant electrochemical energy storage and conversion technologies [6], which are used in various specific applications relying on their performance characteristics. Figure 1.1 shows their difference in energy density, power density, and delivery time scale. Conventional capacitors (at the right-bottom) exhibit extremely high power density, i.e, capacitors can be fully charged or discharged in an extremely short time (normally the order of seconds), but their energy density is relatively low (~0.01-0.1 Wh·kg^{-1} [6]). This characteristic makes them applicable as electrical filters to smooth current fluctuation [7]. On the contrary, fuel cells (at the left upper) are featured by the high energy density of 200-1000 Wh·kg^{-1} [6] and relatively low power density, which can be used as a backup power source in buildings or power supply for electrical vehicles [8]. Batteries and super-capacitors are located between fuel cells and capacitors, which show comparatively higher power density than fuel cells and higher energy density than capacitors. Their applications range from portable electronic, and electrical vehicles, wind/solar powering, fast power regulation (supercapacitors) and stationary storage, etc [8, 9].

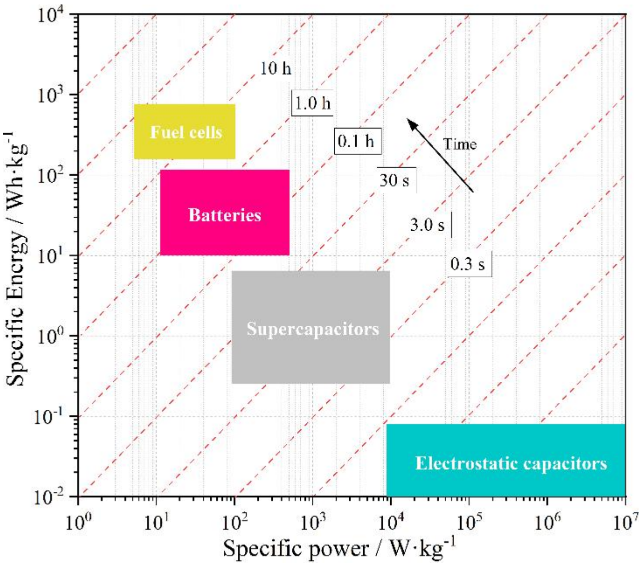

Figure 1.1 The comparison of energy and power density, delivery timescale of electrochemical energy storage and conversion devices [6].

In terms of batteries, four rechargeable battery chemistries, i.e., Pb-acid batteries (PABs), Ni-Cd batteries (NiCd), Ni-metal hydride (NiMH), and lithium-ion batteries (LIBs), have already been introduced over the past two century, with a tendency from the dense, toxic, low-energy batteries to light, green and higher-energy ones (as shown in Figure 1.2). Because of their low cost and high safety (Table 1.1), PABs are still the most adopted technology in modern life. For instance, around 70% of the global energy storage market are occupied by PABs in 2018 [10], with a revenue of 80 billion USD and a total production of 600 GWh. LIBs, which are featured by high energy density and good stability (Table 1.1), have soon become the most popular rechargeable battery in electrical vehicles and electronics since its first successful commercialization in 1991. But with the recently growing demand for more sustainable and high-performance battery technology (e.g., high specific energy, cyclability, high stability, and better safety [11]), the academic research appetite tends to move to develop the next-generation LIBs (e.g., Li-S, Li metal batteries) or other advanced batteries (Na-/Al/Mg-ion batteries, etc) (Figure 1.2) [11]. To date, while none of these advanced technologies have entered maturity [12], sodium-ion batteries (SIBs) have been the fastest-growing one over the past decade, resulting in the foundation of many companies that focus on developing SIBs products [11]. Herein, the thesis revolves around sodium-ion batteries with the hope to contribute to the SIBs development.

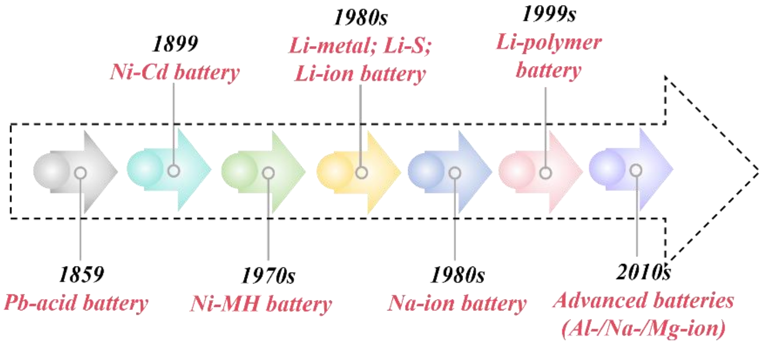

Figure 1.2 The timeline of the different battery technologies development [11].

Table 1.1 Comparison of different battery storage technologies [13, 14]

Characteristics	PABs	NiCd	NiMH	LIBs
Gravimetric energy density/Wh·kg^{-1}	25-50	30-80	40-110	80-250
Gravimetric power density /W·kg^{-1}	150-400	80-300	200-3000	200-2000
Energy cost/ Euro·kWh^{-1}	40-170	680-1300	170-640	500-2100
Working temperature / °C	18-45	-40-50	-30-70	20-65
cycles life /cycles	250-2000	1000-5000	300-1800	100-10000
Efficiency / %	63-90	60-90	50-80	75-97
Environmentally friendly	Low	Low	Low	High

1.1.2 The Development History of Sodium-Ion Batteries (SIBs)

As illustrated in Figure 1.3, the very early studies of the reversible sodium insertion into layered TiS_2 or other layered dichalcogenides in liquid electrolytes were reported in the early 1980s [3, 15], as inspired by the successful electrochemical intercalation of lithium in TiS_2 [16]. Unfortunately, due to the low working voltage of the TiS_2 cathode (~2.2 V vs. Na/Na^+) and the dendrite problem of the Na metal anode, the TiS//Li battery has little possibility of being used in practical application and thereby largely abandoned. To revolve the challenge from the cathode side, the research focus was then gradually moved to the layered transition metal oxides cathodes ($NaMO_2$, M=Co, Ni, Cr, Mn, Fe) [3, 17, 18], especially after Delmas et al. discovered the reversible electrochemical intercalation of Na into Na_xCoO_2, Na_xNiO_2, and Na_xMnO_2 (x<0.5) at around 3.0 V vs. Na/Na^+ [17, 19, 20], which are much higher than that of TiS_2. But for the anode sides, Li metal remained the choice until Scrosati et al proposed an intercalation-type anode as an alternative to Li metal in 1992 [3]. This pioneering work introduced the concept of the so-called rocket-chair battery. But different from the successful intercalation reactions of graphite with Li, the Na insertion into layered graphite or soft carbon was very challenging.

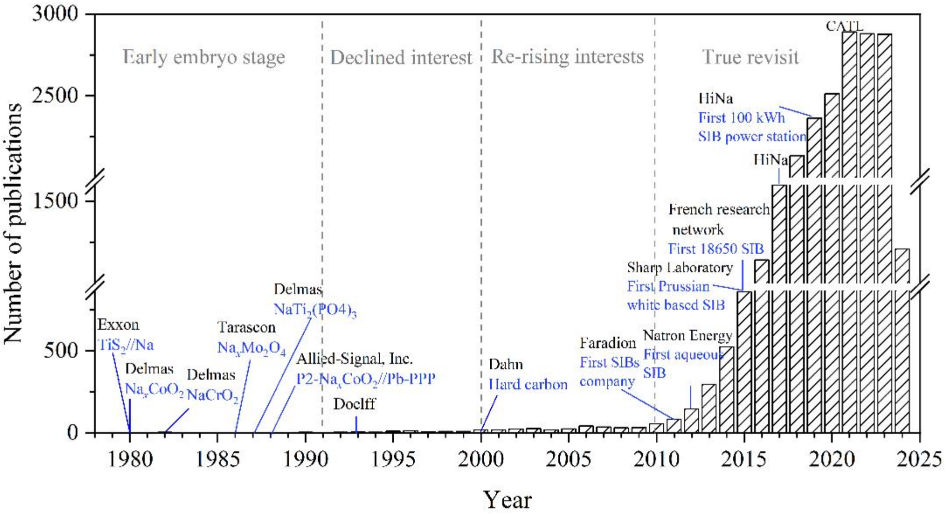

Figure 1.3 The number of published academic papers over the past 40 years, with the important findings or events related to SIBs included [21]. The publication number is collected from the Web of Science by searching the keyword 'sodium-ion batteries'. It should be noted that the number in 2024 is only considered the papers published from January to May.

Even worse, the successful commercialization of LIBs by Sony in 1991 had attracted almost all the researchers' attention. Consequently, there has been a dramatic decline in interest in SIB chemistry since then (Figure 1.3). An important turning point is the discovery of hard carbon by Dahn in 2000, which shows a relatively high capacity of ~300 $mAh{\cdot}g^{-1}$ via the Na intercalation mechanism and has a low sodium-intercalating voltage [22, 23]. This breakthrough indeed re-attracted some attention to the research of SIBs, but it did not trigger an explosion in research or rapid commercialization [16], probably because SIBs are not competitive with LIBs in terms of energy density and electrochemical performance, and thus there is no strong motivation to shift research focus from LIBs to SIBs. As evidenced by Figure 1.3, the number of publications related to SIBs grew slowly from 2000 to 2010. The true reviving of SIBs, supported by the sharp increase in the number of published SIB-related publications [3] [24], might start after the 2010s. It is generally assumed that the sudden rising interest in SIBs is mainly associated with the concern about the Li supply as a result of the growing demand for LIBs due to the thriving of electrical vehicles, and uneven Li source distribution geographically [3].

Since 2010, SIBs have experienced a rapid development in electrode materials, particularly in the cathode. Besides the previously mentioned layered metal oxides (NMO_2), another two families of polyanion compounds and Prussian blue analogs are also developed as potential cathodes [24]. However, little progress has been made in the research of SIBs anode: hard carbon has remained the primary anode since its discovery.

On top of the renaissance of SIBs in academia, the industry also witnesses an advance in the commercialization of SIBs. In 2011, the first NIB company Faradion (UK) was set up, opening the door to the formal commercialization of SIBs. Given the environmental impact of organic electrolytes, aqueous

Na-ion full batteries with Prussian blue analogs as cathode and anode were then manufactured by Natron Energy in 2013, giving a cycle life of 5000 times but low capacity [25]. In 2015, a new $NaMO_2$ cathode for SIBs was produced by Toyota (Japan) [26]. Also, the first 18650-type SIB with polyanion-based compound $Na_3V_2(PO_4)_2F_3$ cathode was launched in French in the same year [27]. By the end of 2015, the potential of Prussian white-type cathode ($Na_{1.92}Fe[Fe(CN)_6]$) in the large-scale production was proven [26, 28]. Subsequently, Navasis Energies, after the optimization of the electrode design, commercialized the Na-ion full batteries with $Na_xMnFe(CN)_6$ cathode, which displays an energy density of 100-130 $Wh{\cdot}kg^{-1}$ [25]. In 2017, a French battery company Tiamat was founded, with a focus on the cylindrical polyanionic-based SIB production [16]. It is reported that over 10000 SIB batteries have been made by Tiamat. In 2019, a Chinese company HiNa, established in 2017, launched a Na-ion full batteries with 150 $Wh{\cdot}kg^{-1}$ and a life span of 4000 cycles, using NMO_2 cathode and hard carbon anode [29]. Meanwhile, the first 100 kWh SIB energy storage power station was then launched in April this year [30]. More recently, CATL (China), the biggest battery manufacturing company, also announced that the SIBs with Prussian blue analogs -based cathode and hard carbon anode deliver an energy density as high as 160 $Wh{\cdot}kg^{-1}$ [25]. Overall, despite some success achieved over the past decade, the commercialization of SIBs is still in the early stage and requires more effort in the future.

1.1.3 Working Principle of SIBs

Analogous to lithium-ion batteries, sodium-ion batteries also store or convert energy through ion carrier insertion or extraction into/from the electrodes during the charge/discharge process, except for the different carrier ions. As is illustrated in Figure 1.4, each battery configuration consists of a cathode and anode in the liquid electrolyte which is separated by the polymer porous membranes. In general, the typical cathode materials are layer transition metal oxides, Prussian blue, and transition metal fluorophosphate, while the anode material is commonly carbon-based materials (e.g., hard carbon) that possess enough space to allow carrier ion intercalation. Upon discharge, Na ions will be extracted from the anode, then transported through the electrolyte, and finally inserted into the cathode, which causes the electric energy to be converted into chemical energy. Conversely, during the charging process, the storage of electrical energy is achieved by the migration of Na ions through the electrolyte to the carbonate materials. Hence the electrode reactions in a Na-ion battery with transition metal oxides cathode and hard carbon anode can be expressed as $NaMO_2 + C_6 \leftrightarrow Na_{1-x}MO_2 + Na_xC_6$ [31]. Following this mechanism, the battery can be cycled many times.

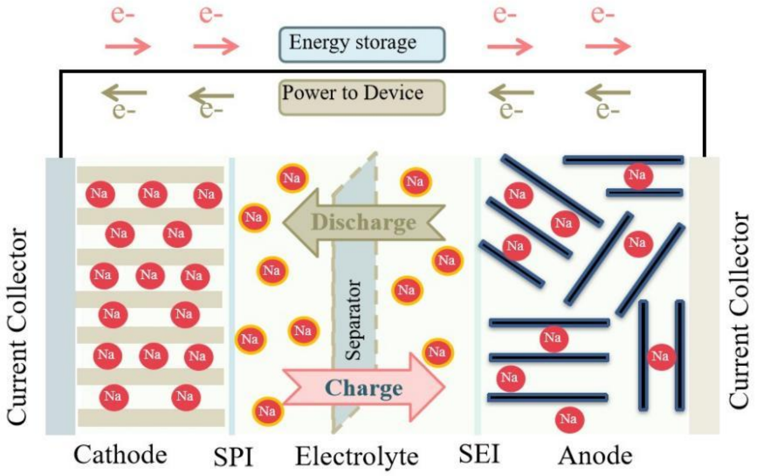

Figure 1.4 Schematic illustration of the working principle of sodium-ion batteries [30].

1.1.4 Application Prospects of SIBs

While the energy density of SIB is not comparable to LIB due to the larger size and weight of Na than Li, the material cost for SIB is cheaper (Table 1.2). On the other hand, in contrast to PAB, SIB performs superior in cycling stability, low- and high-temperature performance, and rate-capability, despite the slightly higher cost. These unique economic metrics and performance characteristics offer SIB great promise in the automotive industry and stationary applications as a complementary source for energy storage.

Table 1.2 Cost and performance comparison of SIBs, Pb-acid batteries (PABs), and LIBs [32]

Indicators	**PABs**	**SIBs** (Cu-Ni-Mn-O//hard carbon)	**LIBs** (LFP//Gr)
Cost (USD·Wh^{-1})	0.04-0.07	0.04-0.08	0.07-0.11
Energy density (Wh·kg^{-1})	30-40	100-150	130-170
Volumetric energy density(Wh·L^{-1})	40-120	~400	~700
Cycle life	<400	1000-5000	1000-5000
Low-temperature performance	poor	good	good
High-temperature performance	medium	good	good
Rate capability	1C	3C-5C	3C

In the field of electrical vehicles (EVs), where the driving range is directly impacted by the volumetric energy density of batteries [33]. Thereby, lower energy density SIBs (volumetric energy density of around 400 Wh·L^{-1}) cannot meet the high range requirement and are not as appealing as higher-energy density LIBs (volumetric one: approximately 700 Wh·L^{-1}) [16]. Nevertheless, this does not mean that SIBs cannot find suitable application scenario. In fact, in low-speed EVs, or electric bicycles, and four-wheeled microcars [16] with less demand on battery energy density, SIBs seem to be a good choice due to their cost advantage. For instance, HiNA (China) has pioneered the development of SIBs-powered low-speed EVs and bikes [29], and other companies like Faradion (UK) and Tiamat (France) are also devoted to producing e-scooters and e-bikes powered by SIBs [16].

In the grid-scale field, PABs have still been the most well-adapted choice for medium to large-scale energy storage systems at present, while the rapid development of Li-ion batteries in past decades makes them quite competitive in emerging large-scale energy storage applications [34]. However, both technologies are facing their bottlenecks with the relatively low energy density of the former and the uneven Li source distribution of the latter. This situation seems to offer an opportunity for low-cost SIBs with moderate volumetric energy density, especially in large-scale grid-scale fields, where cost rather than energy is the critical requirement.

1.2 Review of SIBs Anode Materials

Despite the above-mentioned advantages and application prospects, the development of SIBs also faces big challenges, one of which comes from the anode side. In this part, we will review the present potential SIB anode candidates, with an emphasis on their advantages and challenges, to provide an overview of the research gap for SIB anodes.

1.2.1 Graphite

Graphite carbon, the most successfully commercialized anode material in LIBs, can hardly store sodium, i.e., only limited Na storage capacity (~20 $\text{mAh}\cdot\text{g}^{-1}$) is obtained. The unfavorable intercalation behavior was often attributed to the larger size of Na atoms (ca. 0.102 nm), which makes Na atoms challenging to insert into the limited interlayer spacing of graphite (ca. 0.335 nm). But this explanation is debatable, given that the K ion or other alkali ions (e.g., Cs^+, Rb^+) with a larger radium (than Na) can be stored in graphite to form intercalation compounds (e.g., KC_8) [35-37]. Theoretical studies imply that the thermodynamically unstable sodium-intercalated graphite compounds could be the possible reason for unfavorable Na-storage behavior of graphite because both NaC_6 and NaC_8 have positive enthalpies of formation [37, 38]. The binding energy between the graphene layers of NaC_6 is calculated to be the lowest compared to that of LiC_6 and KC_6, largely explaining the instability of sodiated graphite. The Van der Walls force between graphene layers may be too low to hold the overall structure of the sodiated graphite [39]. Jache and Adelhelm reported a breakthrough that the graphite could obtain a reversible capacity of over 100 $\text{mAh}\cdot\text{g}^{-1}$ in ethers electrolyte through the intercalation of solvated Na ion ('Co-intercalation') to form a *t*-graphite-intercalation compound (*t*-GIC) in 2014 [40]. Advanced experimental tools confirm the reaction mechanism $Na(solv)_n + x \cdot C + e^- \xleftrightarrow{\text{intercalation}} Na(solv)_n C_x$ and that the reversibility of the co-intercalation reaction was surprisingly high [38], which reignites the research interests in graphite and makes it a potential SIB anode.

Advantages: While graphite cannot achieve a capacity comparable to hard carbon, it shows a high rate-capability because of the fast kinetics of solvated ions intercalation [38]. The weak interaction between solvated ions and graphite, no need for desolvation during the co-intercalation reaction, combined with the marginal formation of the SEI layer on the interface are assumed to be responsible for the fast diffusion of solvated ions in graphite [41, 42]. In addition, graphite exhibits superior cycling stability and high coulombic efficiency. As supported, many literatures reported that the graphite electrode can always survive more than 1000 cycles [43-47]. These unique advantages endow graphite with great potential to be used in high-power energy devices.

Challenges: However, some challenges still need to be resolved. First, the uncompetitive specific capacity (normally 100-150 $mAh\cdot g^{-1}$) and its high average sodium-intercalating voltage (0.6-0.8 V vs. Na/Na^+) [44, 45, 48], will result in unappealing energy density. Second, the graphite electrode generally suffers from a large volume expansion of 70-100% during the (dis-)charge [49], which is detrimental to the cycling stability [39]. Meanwhile, more electrolytes should be needed in graphite-based SIB since the solvent is also involved in the co-intercalation reactions, which will increase the material cost. Third, the co-intercalation reaction seems to occur only in specific solvents (e.g., ether), and its mechanism remains elusive [50]. Finally, there remains debate about the stability and formation mechanism of SEI in graphite/electrolyte interface [38]. Overall, the research on graphite is still in its infancy stage, and many issues need further exploration.

1.2.2 Hard carbon

Hard carbon (HC), a well-known non-graphitizable carbon, is well-adopted as a potential SIB anode owing to its abundance and environmental benignity. Different from graphite, sodium ions can intercalate into the graphite layer, fill in the nanopores between randomly stacked layers, and be absorbed in the defect sites of HC, yielding a high initial specific capacity (ca. 300 $mAh\cdot g^{-1}$) [51]. These various behaviors of ion storage contribute to a typical galvanostatic discharge-charge profile of hard carbon featured by a sloping region and a large plateau region [51]. Over the past years, many efforts have been made to understand the sodium storage mechanism of hard carbon [52]. At present, four prevailing sodium storage mechanisms are proposed: the 'intercalation-filling' model [22], the 'absorption-intercalation' model [53, 54], the 'absorption-filling model [55, 56], and the '3-stage' model [57]. However, there remains controversy regarding whether the sodium storage behavior in sloping (or plateau) regions is the result of sodium intercalation, absorption, or filling. Hence further investigations are still required into this issue.

Advantages: Since the ratio between Na and C of the stable sodium-embedded compounds (NaC_8) is low (i.e., 1:8), the volume change is limited during cycling, which enables hard carbon with superior cycling stability. Moreover, the low average redox potential (~0.1 V vs. Na/Na^+) of hard carbon gives a high working voltage of full cells, which can maximize the energy density. In addition, the disorder structure of hard carbon, featuring by high content of voids and defects, expanded interlayer space, and high concentration of heteroatoms, facilitates the Na transport and charge transfer process, which endows hard carbon with the potential of fast-charging capability. These performance metrics, combined with sustainability and their cost advantage in raw materials, support hard carbon as the most promising SIB anode for practical applications.

Challenges: While hard carbon benefits from low volume change, the low stoichiometric ratio of the Na_xC compound also limits its specific capacity. Furthermore, the initial coulombic efficiency (ICE) of hard carbon is extraordinarily low (~40%), since a large amount of sodium ions are irreversibly inserted into the defect sites, or consumed due to the electrolyte breakdown [58]. This causes hard carbon to normally deliver a much lower reversible capacity (e.g., ca. 150 $mAh \cdot g^{-1}$), limiting the energy density [52, 59]. Meanwhile, the cycle life of hard carbon, normally 200-300 cycles [60], is also far from satisfactory. Additionally, from a safety dimension, Na deposition can hardly be prevented due to the low sodiation potential of hard carbon electrodes, especially under fast charging conditions and/or low temperatures. Further, the industrial production of hard carbon often requires high-temperature carbonization in an inert atmosphere, which is complicated and energy-consuming [61].

1.2.3 Alloying Anodes

Alloy elements have recently attracted enormous attention because they are expected to have thermodynamically stable Na-rich phases. As shown in Figure 1.5, a number of elements, such as Si, Ge, P, Pb, etc., are known to alloy with sodium based on the Na-M binary phase diagram. The average potential of alloying reactions for these alloy anodes is relatively moderate, almost below 0.8 V vs. Na/Na^+. Moreover, nearly all the alloys except for Ga have a volumetric capacity above 900 $mAh \cdot cm^{-3}$, approximately double as high as hard carbon. Their utilization therefore could increase the volumetric capacity of SIB anodes, and further increase the competitiveness of SIB. In this section, we will primarily introduce several representative alloy materials which have the potential to be used in practical applications, with a focus on their unique characteristics, sodiation mechanism, and challenges.

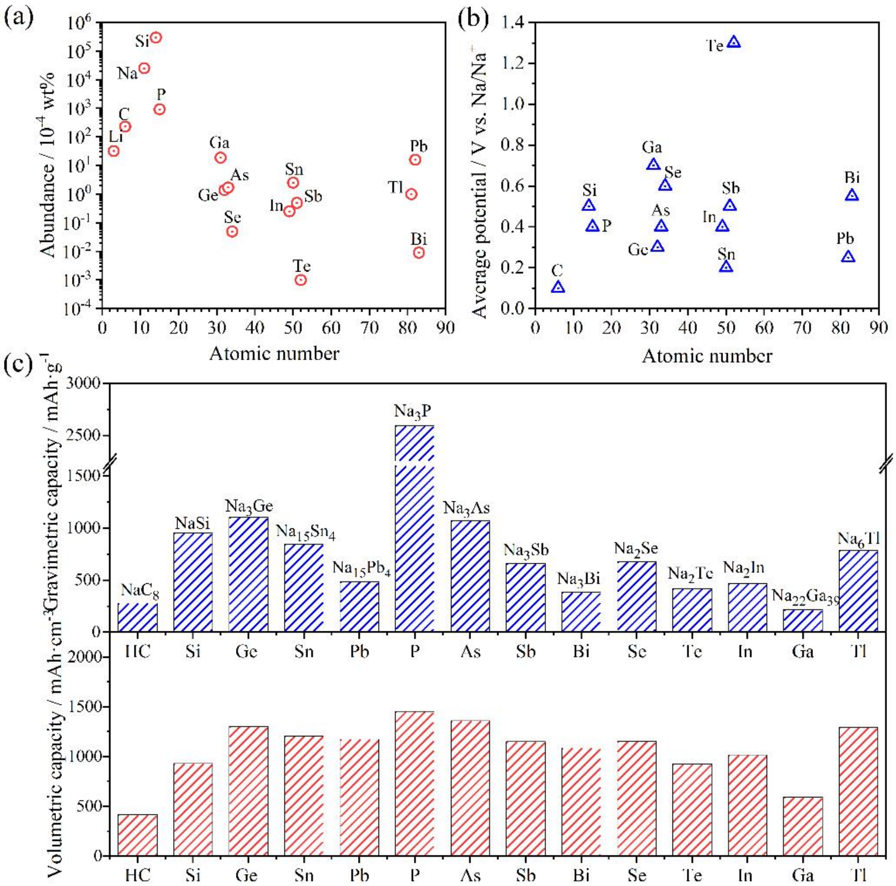

Figure 1.5 (a) The Earth's crust abundance [62] and (b) Average sodium-inserting potential of alloy elements [61, 63-67]. (c) The theoretical gravimetric and volumetric capacity of potential SIBs alloy anodes. It is noted that the volumetric capacity is calculated with regard to the Na-M alloy volume rather than the M active material according to reference [68].

1.2.3.1 Phosphorus

Phosphorus (P), the group VA element of the periodic table, has attracted enormous attention in SIB over the past decade owing to its abundance (Figure 1.5a, 11th abundant element in the Earth's crust), high theoretical capacity, and low cost [69]. There are three different allotropes for phosphorus, i.e., white, red, and black P. Among them, white P is commonly neglected as a SIB anode due to its instability in the ambient environment and toxicity. Red P is more stable than white P and shows great application potential in electrochemical applications because of its low cost and easy preparation. Black P, the most stable allotrope, possesses good electrical conductivity (~10^2 S·cm^{-1}), and is also an attractive anode candidate for high-energy SIBs, although the synthesis process for black P is complicated [39]. Despite the difference, the sodium storage of both black and red P is achieved by the alloying reactions between Na and P, following the below equation. Noteworthy, the intermediate Na-P phase is still unclear to date.

$$Na + xP \rightarrow Na_xP\ (0 < x < 3)$$
$$Na + Na_xP \rightarrow Na_3P$$

Advantages: P (both black and red P) possesses an extremely high theoretical gravimetric or volumetric capacity (2596 mAh·g^{-1} or ~1455 mAh·cm^{-3}, Figure 1.5 c) given the Na/P ratio of 3 for the final sodiated phase Na_3P. This capacity superiority ensures that a smaller amount of P is required to reach the same capacity requirement in contrast to a low-capacity anode candidate, which lowers the SIB cost to some extent [7]. On top of this, phosphorus has an appropriate average sodium-inserting potential (~0.4 V vs. Na/Na$^+$, Figure 1.5b) [70], and is abundant in Crust (Figure 1.5a) and non-toxic. These characteristics make P an attractive electrode candidate for high-energy SIB.

Challenges: Although the chemistry of 3Na in 1P ensures the large capacity of P electrodes, it also gives rise to a significant volume expansion (>300%) [71], which causes the electrode structural collapse and induces the loss of electrical contact, thereby resulting in poor cycling stability. Meanwhile, the low electrical conductivity (especially for red P, ~10^{-14} S·cm^{-1}) significantly hinders the charge transfer, thus greatly limiting the rate capability of the P electrode. In addition, unstable SEI is another challenge that could be considered before its commercialization. The large volume change during cycling will cause the SEI layer to crack, and more SEI will be formed on the exposed electrode surface, which leads to increased cell impedance and finally low coulombic efficiency [69].

1.2.3.2 Antimony

Antimony (Sb), which possesses a layer structure with the ideal interlayer space for sodium insertion [72], has been emerged as a rising star for SIB and widely studied. Like P, Sb also alloys with Na to form Na-Sb alloys at certain potentials (~0.5 V vs. Na/Na$^+$, Figure 1.5b), converting electrical to chemical energy, and vice versa. In general, the (de-)alloying reaction proceeds through multiple steps rather than one step [73], which can be expressed by:

$$Sb + xNa^+ + xe^- \leftrightarrow Na_xSb$$
$$Na_xSb + (1-x)Na^+ + (1-x)e^- \leftrightarrow NaSb$$
$$NaSb + 2Na^+ + 2e^- \leftrightarrow Na_3Sb$$

Noteworthy, since the intermediate Na-Sb phases formed are mostly amorphous, the stoichiometry of these phases cannot be determined accurately and thereby remains debated [74]. Generally, the final sodiated phase Na_3Sb competes between the hexagonal and cubic structure [75].

Advantages: Thanks to the high Na/Sb ratio of 3 for Na_3P, Sb exhibits a high theoretical specific capacity of 660 mAh·g^{-1} upon the full sodiation, corresponding to a high volumetric capacity of ~1150 mAh·cm^{-3} (Figure 1.5c). Also, Sb has a moderate sodium-inserting potential, which makes it suitable for SIB anode. Furthermore, different from P, Sb has an excellent electrical conductivity of ~2.56×10^6 S·cm^{-1}·, which facilitates the charge transfer. Therefore, the electrochemical reactions for Sb electrode are more favorable kinetically than P [76]. Additionally, the relatively abundant raw material reserve (Figure 1.5a) and non-toxicity make Sb more attractive as a practical SIB anode candidate.

Challenges: Despite the above appealing properties, Sb also faces two major challenges which make it far from a practical application. The first one is the large volume change (~390%) induced by the alloying/dealloying reactions [77], which will cause the electrode to collapse, leading to fast capacity degradation. Another challenge for commercialization is slow reaction kinetics during the (de-)sodiation process [78], which could result in the capacity fade, and poor cycling stability.

1.2.3.3 Bismuth

Bismuth (Bi), just like Sb, has a layer structure but with a larger interlayer space (~0.395 nm), which facilitates the sodium insertion, and thereby is also considered as a potential SIB anode candidate [39]. The electrochemical sodiation of Bi proceeds through a two-step alloying reaction, successively forming NaBi and Na_3Bi intermetallic phases at certain potentials [79, 80]:

$$Na + Bi \leftrightarrow NaBi$$

$$2Na + NaBi \leftrightarrow Na_3Bi$$

The phase transformation agrees well with the Na-Bi equilibrium phase diagram. But it is also worth mentioning that the crystal structure of the Na_3Bi phase competes between hexagonal and cubic ones, depending on the Bi particle size.

Advantages: Despite the moderate gravimetric capacity of 385 $mAh\cdot g^{-1}$ (Na_3Bi) [81], the alloying reactions yield an interesting volumetric capacity of ~1088 $mAh\cdot cm^{-3}$ (Figure 1.5c). Moreover, the fast sodium diffusion in Na-Bi alloys may endow Bi with good rate capability, i.e., Bi shows the fast-charging potential [82]. Additionally, the high electrical and ionic conductivity, together with non-toxicity also make Bi an appealing anode candidate for SIBs.

Challenges: However, the (de-)alloying reactions between Na and Bi (1.5) induce a significant volume change (~250%), which causes the loss of electrical contact between the electrode and current collector, further deteriorated cycle life [83].

1.2.3.4 Other alloys

Besides P, Sb, and Bi, other alloy elements (particularly group IV and IIIA) also attracted much attention since they can form alloys with Na electrochemically. For instance, Indium can alloy with sodium to form Na_2In, giving a 467 $mAh\cdot g^{-1}$ (1016 $mAh\cdot cm^{-3}$). Ge and Si can deliver a theoretical capacity of 1107 $mAh\cdot g^{-1}$ (1304 $mAh\cdot cm^{-3}$) and 954 $mAh\cdot g^{-1}$ (~930 $mAh\cdot cm^{-3}$), respectively, upon the formation of Na_3Ge and NaSi (Figure 1.5c). More information regarding the sodium-storage characteristics and mechanisms of these alloys can be found in the reference [84]. On top of the pure alloys, various intermetallic alloys, such as SbNi, SnSb, CuSn, Sn_3P_4, or $Sn_{10}Bi_{10}Sb_{80}$ [85] also exhibit attractive features as SIB anode materials, through modifying the Na-storage behavior of pure alloy, e.g., the improved cycling stability by effectively mitigating the pulverization and/or increasing the electrical conductivity [39, 86].

Overall, despite the efforts made over the past decades, a stable SIB anode has not been established to date, especially when application standards are considered. Therefore, further development of new electrode candidates with reasonable capacity, satisfactory cycle life, and high safety of inexpensive anode is favored in the SIB field.

1.3 Utilization of Group IVA Alloy Elements

1.3.1 Motivations

Group IVA alloy elements (abbreviated as M_{IVA} elements), i.e., Si, Ge, Sn, and Pb, exhibit interesting Na storage capabilities due to the success of their Li analogy. Theoretically, they are capable of alloying with sodium at relatively low potentials (almost 0.2-0.5 V vs. Na/Na^+, Figure 1.5b), yielding high gravimetric (or volumetric) capacities. For instance, Si, Ge, Sn, and Pb will deliver a gravimetric (or volumetric) capacities of 954 $mAh \cdot g^{-1}$ (~930 $mAh \cdot cm^{-3}$), 1107 $mAh \cdot g^{-1}$ (~1300 $mAh \cdot cm^{-3}$), 847 $mAh \cdot g^{-1}$ (~1210 $mAh \cdot cm^{-3}$) and 485 $mAh \cdot g^{-1}$ (~1174 $mAh \cdot cm^{-3}$), upon the formation of NaSi, Na_3Ge, $Na_{15}Sn_4$, and $Na_{15}Pb_4$, respectively (Figure 1.5c). These theoretical capacities are approximately 2.5-3 times higher than that of hard carbon for the volumetric one and 1.5-3 times for the gravimetric one. On the other hand, the Na-alloying potential of M_{IVA} elements is normally 0.2-0.5 V vs. Na/Na^+, higher than the Na deposition potential, which makes them less safety risk due to the Na dendrite formation during charging. Furthermore, the utilization of M_{IVA} elements as SIB anodes also possesses other metrics, including the abundant reverse in Earth's crust (Figure 1.5a), low cost (except for Ge), as well as good electrical conductivity (except for Si). Noteworthy, Sn and Pb can be utilized as electrodes in foil architecture, which not only lowers the material cost and increases the energy density due to the omittance of the Cu current collector and other inactive additives but also simplifies the manufacturing process. All of these advantages offer them great opportunities to be high-capacity anode materials for high-energy-density SIBs.

1.3.2 Fundamentals of Group IVA Alloy Elements

1.3.2.1 Structure and Basic Physio-chemical Properties of Si, Ge, Sn, and Pb

The crystal structures of group IVA alloy (M_{IVA}) elements are schematically illustrated in Figure 1.6. Both Si and Ge have the face-centered diamond cubic structure, where each Si or Ge atom is bonded to the neighboring four atoms to form the tetrahedra $SiSi_4$ or $GeGe_4$, but the lattice constant of Ge is slightly larger. Differently, (β-)Sn has a tetragonal structure with each Sn atom bonded to twelve covalent atoms. Pb is structured in a face-centered cubic space group but with a different space group than Si and Ge. Analogous to Sn, each Pb atom is bonded to twelve neighboring atoms to form the $PbPb_{12}$ cuboctahedra. Meanwhile, as the atomic number increases, the bond length of M-M increases from 0.236 nm (Si-Si) to 0.353 nm (Pb-Pb), indicating the softening elastic property. This may explain the low melting point for Sn and Pb, and that Si and Ge are brittle while Sn and Pb are ductile (Table 1.3). Regarding the electrical property, the conductivity of Si is very poor, while Ge is a semiconductor, with better electrical conductivity than Si. In contrast, Sn and Pb are highly conductive metals (Table 1.3). While few solid data with respect to the diffusion coefficient of Na in M_{IVA} elements are reported, it is expected that the larger lattice parameters of Sn and Pb provide more space to accommodate Na, enabling more favorable sodiation kinetics.

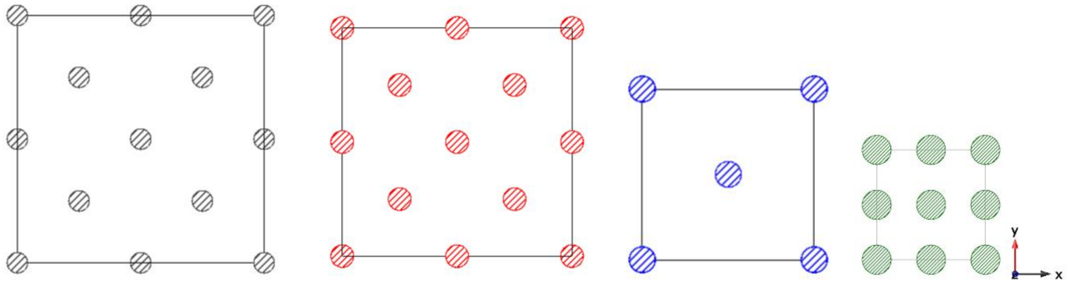

Figure 1.6 Structural schematic of Si (gray), Ge (red), Sn (blue), and Pb (green).

Table 1.3 Comparison of the physio-chemical properties of Si, Ge, Sn, and Pb anodes.

Materials	Crystal structure	Space group	Lattice parameters			Volume / nm^3	M-M bond length /nm	Electrical conductivity at 293 K / $S\cdot cm^{-1}$	Mechanical property
			a/nm	b/nm	c/nm				
Si	Cubic	$Fd\bar{3}m$	0.544	0.544	0.544	0.161	0.236	4.35×10^{-4}	Brittle
Ge	Cubic	$Fd\bar{3}m$	0.567	0.567	0.567	0.183	0.246	2.17	Brittle
Sn	Tetragonal	I4/mmm	0.350	0.350	0.468	0.057	0.341 / 0.35	$\sim9.17\times10^{6}$	Ductile
Pb	Cubic	Fm3m	0.499	0.499	0.499	0.124	0.353	$\sim4.55\times10^{6}$	Ductile

It is noted that structural information is obtained from Material Explorer.

1.3.2.2 The Electrochemistry of Na-M_{IVA}

(1) The Na-M Phase Diagram and Electrochemical Sodiation

The solid-state Na-M_{IVA} phase diagram (Figure 1.7-10) provides the theoretical basis for the electrochemical sodiation of M_{IVA} alloy. As shown in Figure 1.7, there exists two equilibrium Na-Si phases, i.e., Na_4Si_{23}, and NaSi for the Na-Si systems. The theoretical calculation predicted the most stable Na-Si phase thermodynamically is $Na_{0.76}Si$ [87] or $Na_{0.75}Si$ [88]. However, no successful sodiation of Si has proven this claim to date.

For the Na-Ge system (Figure 1.8), three different equilibrium Na-Ge phases, i.e., $NaGe_4$, NaGe, and Na_3Ge are present. However, it is a bit challenging to determine the sodiated mechanism and phases since merely amorphous Ge is capable of storing Na electrochemically and these sodiation Ge phases are also amorphous. $Na_{1.6}Ge$ is theoretically predicted to be the most stable Na-Ge phase at room temperature [88]. However, there remains debate about the final sodiation products from the experimental results: Paul et al. reported that the sodiation of Ge ended at $Na_{1.38}Ge$ phase based on the capacity quantification [89], while Xiaoyu Liu et al reported that the final sodiated Ge phase is estimated to be $Na_{1.6}Ge$ according to the monitored volume change [90].

From the Na-Sn phase diagram (Figure 1.9), many Na-Sn intermetallic phases including $NaSn_6$, $NaSn_4$, $NaSn_3$, $NaSn_2$, NaSn, Na_9Sn_4, Na_5Sn_2, Na_3Sn, and $Na_{15}Sn_4$ are stable at ambient temperature and no single-phase region is present [91]. However not all these phases are formed during the electrochemical sodiation, i.e., some phases are generally bypassed. Chevrier et al suggested $NaSn_5$, NaSn, Na_9Sn_4 and $Na_{15}Sn_4$ as the sodiation phases by DFT calculation [92]. Experimental results confirmed that the sodiation of Sn proceeds with a series of phase transformations which are consistent with the Na-Sn phase diagram [93-96], but there remains controversy about the intermediate sodiated phase.

The Na-Pb phase diagram (Figure 1.10) indicates five Na-Pb intermetallic phases, i.e., β phase, NaPb, Na_9Pb_4, Na_5Pb_2, and $Na_{15}Pb_4$ in an ambient environment. There also exist two single-phase regions: The β phase shows a relatively broad solid solution region with the Na content ranging from 28 to 33 at%, while $Na_{15}Pb_4$ shows a very narrow solid solution region. Electrochemically, the sodiation of Pb was confirmed by in-situ x-ray diffraction techniques to follow the process: Pb-$NaPb_3$-Na_9Pb_4-$Na_{15}Pb_4$ [79, 97], but there remains debate about the formation of Na_5Pb_2, which basically agrees with the phase diagram.

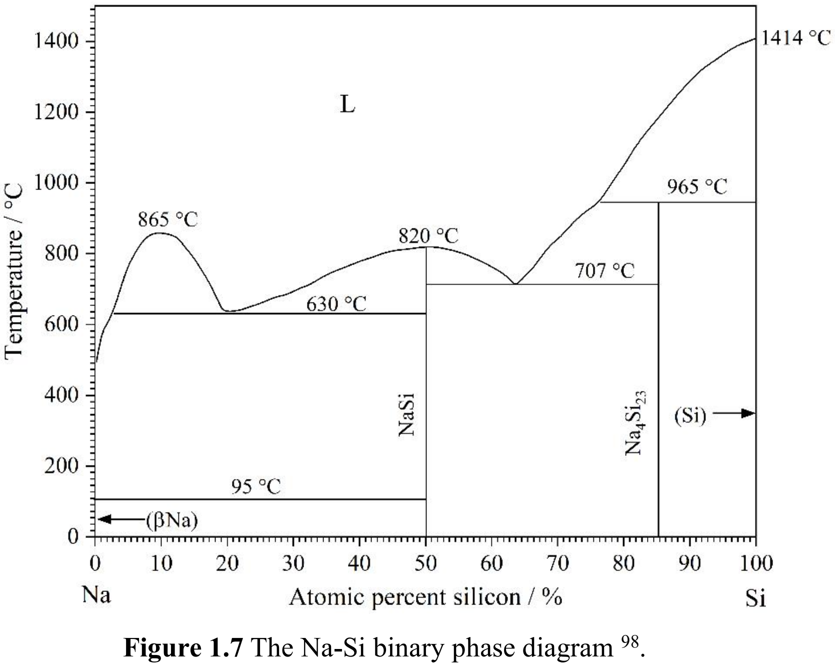

Figure 1.7 The Na-Si binary phase diagram [98].

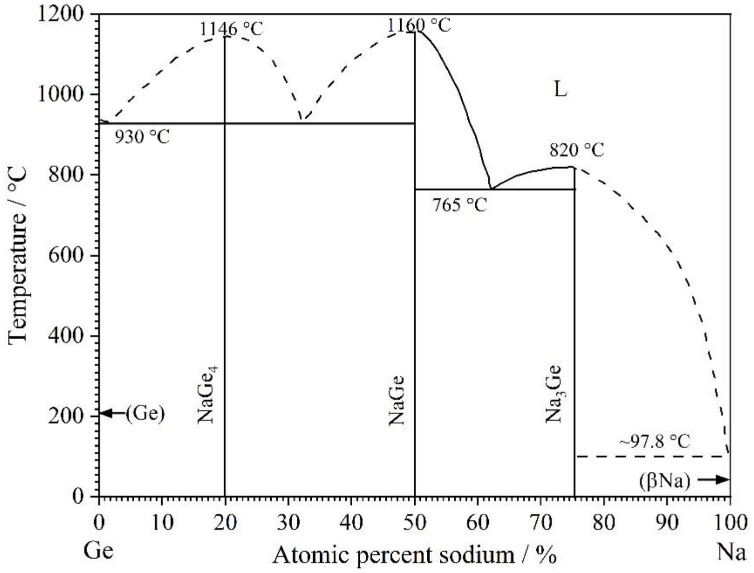

Figure 1.8 The Na-Ge binary phase diagram [99].

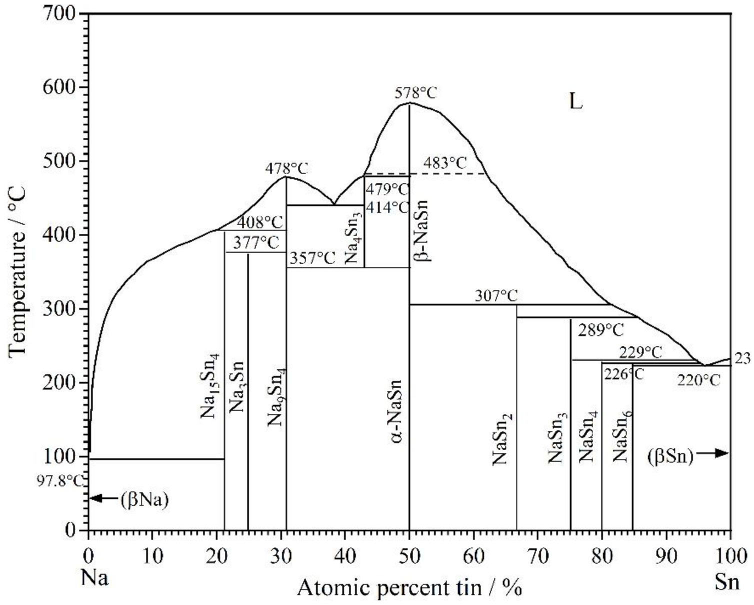

Figure 1.9 The Na-Sn binary phase diagram [91].

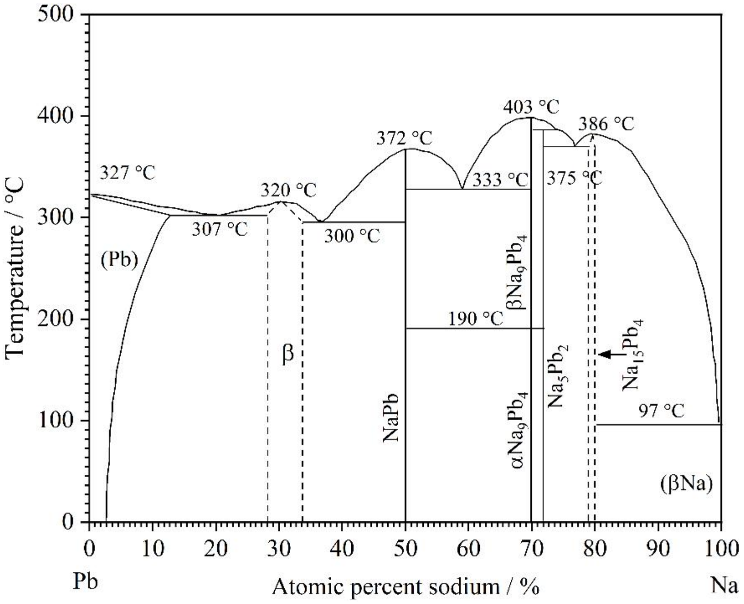

Figure 1.10 The Na-Pb binary phase diagram [79].

(2) The Crystal Structure of Na-M_{IVA} Intermetallic Phases

Table 1.4 gives the structural information of Na-Si, Na-Ge, Na-Sn, and Na-Pb intermetallic phases, with the schematic illustration of these phases' structure shown in Table 1.5-1.8. Overall, the lower-order Na_xM alloys (x<1) seem to remain the structure of pure M_{IVA}, and the Na-richest equilibrium Na-M phase likely crystallizes in a cubic structure (Table 1.4). Specifically, in the case of Na-Si system, the Na_4Si_{23} phase maintains the cubic structure, but its lattice constant is expanded to 1.019 nm compared with pure Si. As the Na/Si atomic ratio rises to 1, the crystal structure of Na-Si is transformed to be monoclinic, with the lattice parameters of a=1.211 nm, b=0.655 nm, and c=1.101 nm. For the Na-Ge phases, few structural details with regard to the equilibrium $NaGe_4$ phase, indicated by the phase diagram, have been reported. Like NaSi, NaGe also has a monoclinic structure but crystallizes in a different space group. The richest Na-Ge phases, Na_3Ge, crystallize in cubic structure and the lattice parameters are extended to 0.743 nm.

Among the lower Na-Sn phases, the equilibrium Na_xSn phase (i.e., $NaSn_5$, $NaSn_3$, and NaSn) structures in the tetragonal space groups, whereas the $NaSn_2$ phase has a monoclinic structure. For the high-order Na-Sn phases, while the structure of Na_9Sn_4 and Na_5Sn_2 becomes orthorhombic and trigonal, the structure of $Na_{15}Sn_4$ (the Na-richest intermetallic phase) turns into a cubic one. The Na-Pb system shows an analogous trend in the change of crystal structure with the increasing Na/Pb ratio. Namely, the $NaPb_3$ keeps the original structure of pure Pb, and other phases i.e., NaPb, Na_9Pb_4, and $Na_{15}Pb_4$ show similar cubic, tetragonal, orthorhombic, and cubic structure as that of Na-Sn phases with the same stoichiometry.

Table 1.4 Structure information of Na-M_{IVA} (M_{IVA}=Si, Ge, Sn, and Pb) phases

Materials		x in Na_xM	Crystal structure	Space group	Lattice parameters			Volume / nm^3
					a/nm	b/nm	c/nm	
Na-Si	Na_4Si_{23}	0.17	Cubic	$Pm\bar{3}n$	1.019	1.019	1.019	1.056
	NaSi	1	monoclinic	C2/c	1.211	0.655	1.101	0.763
Na-Ge	NaGe	1	monoclinic	$P2_1/c$	1.134	0.668	1.168	0.818
	Na_3Ge	3	Cubic	$Fm\bar{3}m$	0.743	0.743	0.743	0.409
Na-Sn	$NaSn_5$	0.2	Tetragonal	$P\bar{4}2_1m$	0.635	0.635	0.891	0.36
	$NaSn_3$	0.33	Tetragonal	I4/mmm	0.466	0.466	0.967	0.21
	$NaSn_2$	0.5	Monoclinic	C2/m	1.355	0.693	1.545	1.416
	NaSn	1	Tetragonal	$I4_1/acd$	1.034	1.034	1.741	1.892
	Na_9Sn_4	2.25	Orthorhombic	Cmcm	0.537	0.934	2.879	1.444
	Na_5Sn_2	2.5	Trigonal	$R\bar{3}m$	0.540	0.540	2.224	0.562
	$Na_{15}Sn_4$	3.75	Cubic	$I\bar{4}3d$	1.303	1.303	1.303	2.210
Na-Pb	$NaPb_3$	0.33	Cubic	$Pm\bar{3}m$	0.490	0.490	0.490	0.117
	NaPb	1	Tetragonal	$I4_1/acd$	1.057	1.057	1.783	1.993
	Na_9Pb_4	2.25	Orthorhombic	Cmcm	0.547	0.945	3.035	0.606 [100]
	$Na_{15}Pb_4$	3.75	Cubic	$I\bar{4}3d$	1.315	1.315	1.315	2.274

The information for the structure and lattice parameters is obtained from the Materials Project.

Table 1.5 The unit cell structure of Na-Si alloys

Alloys	**Na_4Si_{23}**	**NaSi**
Unit cells	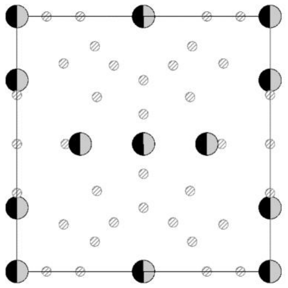	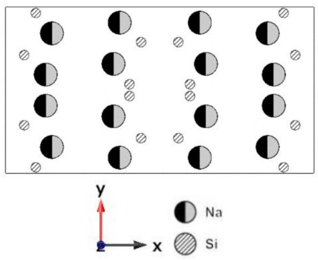

Table 1.6 The unit cell structure of Na-Ge alloys

Alloys	**NaGe**	**Na_3Ge**
Unit cells	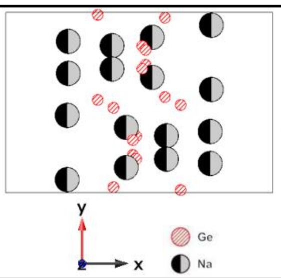	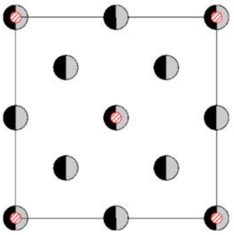

Table 1.7 The unit cell structure of Na- Sn alloys

Alloys	**$NaSn_5$**	**$NaSn_3$**	**$NaSn_2$**	
Unit cells	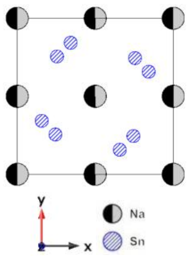	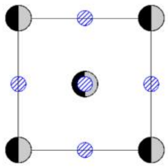	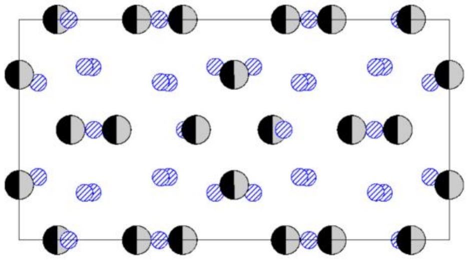	
Alloys	**NaSn**	**Na_9Sn_4**	**Na_5Sn_2**	**$Na_{15}Sn_4$**
Unit cells	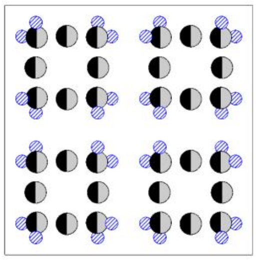	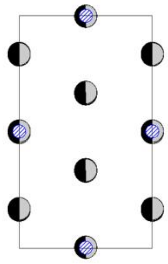	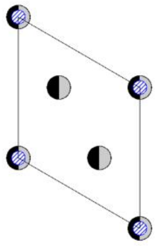	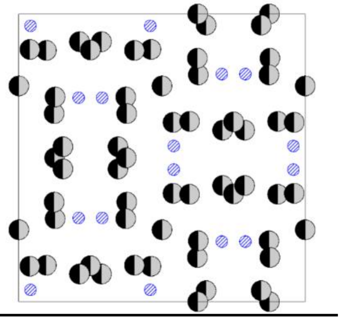

Table 1.8 The unit cell structure of Na-Pb alloys

Alloys	**$NaPb_3$**	**NaPb**	**Na_9Pb_4**	**$Na_{15}Pb_4$**
Unit cells	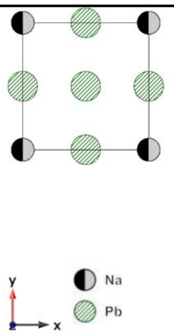	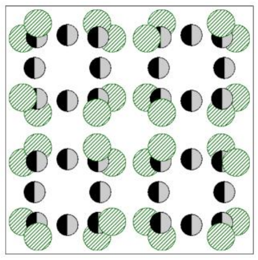	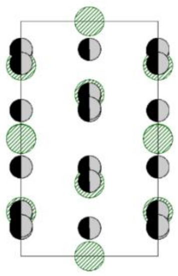	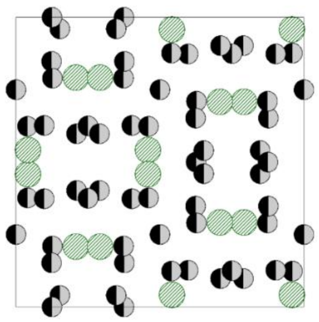

(3) Theoretically Predicted Sodiation Plateaus

Figure 1.11 shows the sodiation voltage curves for Si, Ge, Sn, and Pb, obtained from the density function theory (DFT) calculation according to the known crystal structure of Na-M_{IVA} intermetallic alloys. For the Na-Si system, the formation of NaSi is predicted to occur at a very low potential, around 0.05 V vs. Na/Na^+, while the calculated sodiation potential is in a wide range of 0.02-0.5 V for Na-Ge systems, 0.1-0.65 V for Na-Sn systems, and 0.1-0.45 V for Na-Pb systems.

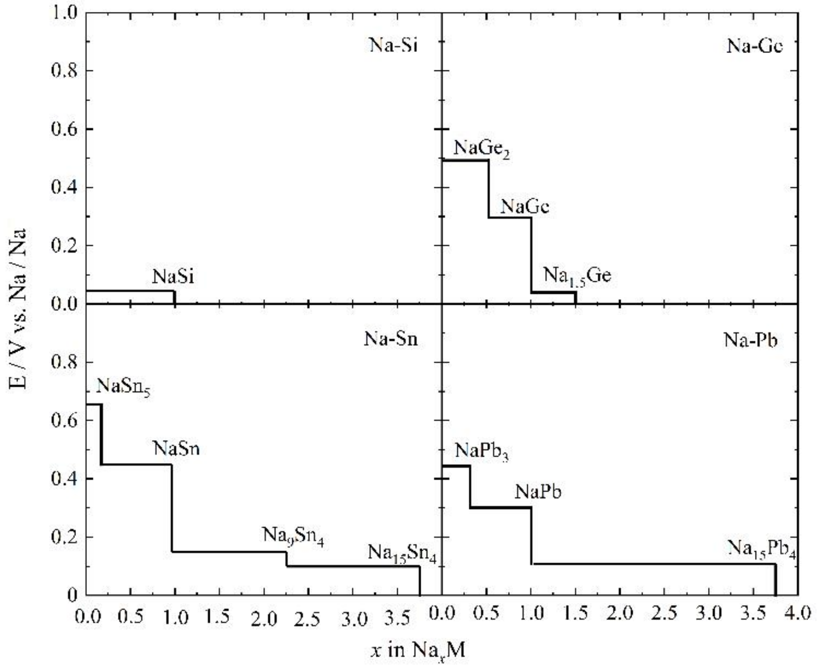

Figure 1.11 The DFT predicted voltage curve of Na-M_{IVA} alloys based on their crystal structures, (a) Na-Si, (b) Na-Ge, (c) Na-Sn, and (d) Na-Pb. Data are obtained from the reference [88, 92, 101].

(4) Theoretical Predicted Capacity and Volume Expansion

The theoretical capacities of different Na_xM intermetallic phases as a function of x are shown in Figure 1.12a. The values are estimated by using the equation $Q = xF/3.6m$, where x is the atomic ratio, F is Faraday's constant, and m is the atomic mass of M_{IVA}. Notably, the higher the atomic ratio, the higher sodiation capacities obtained by Na-M_{IVA} alloys. Meanwhile, the larger the mass weight of M_{IVA} is, the lower the capacity of Na_xM phases at the same ratio x is. For instance, the capacities of NaPb, Na_9Pb_4, and $Na_{15}Pb_4$ phases are all much lower than that of Na-Sn phases with the same stoichiometry.

Since the Na-M intermetallic phase has different crystal structures with different lattice parameters (Table 1.4), the Na insertion/extraction will induce the volume change. Figure 1.12b shows the calculated volume change as a function of Na content. It is noted that the V/V_0 here is normalized to the per M_{IVA} based on the Na-M_{IVA} structural information. In general, the volume change of Na_xM phases shows a linear increase with the rising atomic ratio. For instance, the transformation of Ge to NaGe is estimated to result in a ~116% volume expansion theoretically while a significantly larger volume change of approximately 350% could occur upon the formation of Na_3Ge. The sodiation to the Na-richest $Na_{15}Sn_4$ phase will cause a ~370% volume change and the formation of $Na_{15}Pb_4$ will give a ~360% volume change.

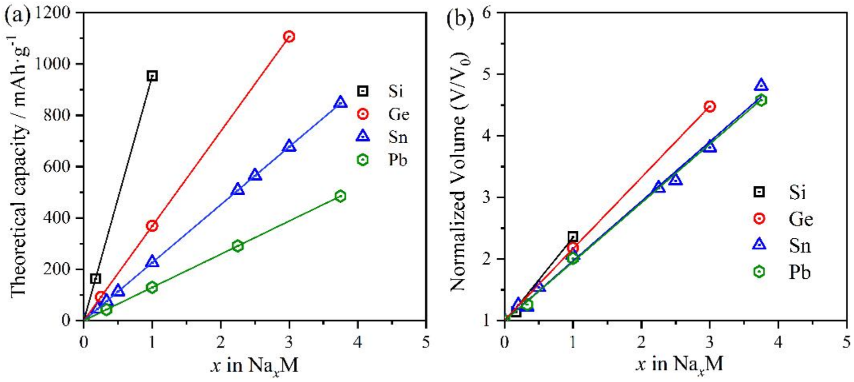

Figure 1.12 (a) The calculated theoretical capacity of Na_xM, and (b) Variation in the volume of Na_xM as a function of Na content (x).

(5) The DFT Simulated Physio-chemical Property of Na_xM Alloys

Electrical properties. While pure Sn shows good electrical conductivity (Table 1.3), it was reported that the sodiation results in dramatic increase in electrical resistivity of Sn electrode, i.e., Na-Sn alloys could be highly resistive [102]. For Na-Pb alloys, no experimental results regarding their electrical properties have been reported, although an early study showed increased electrical resistivity with increasing Na content at high temperatures [103]. Also, the electrical properties of Na-Si and Na-Ge alloys have rarely been reported.

Diffusion behaviors. Some theoretical calculations predict the diffusivities of Na in Si (or NaSi), Ge (or NaGe), and Sn (or NaSn) are in the order of 10^{-9}~10^{-10} $cm^2·s^{-1}$, while the sodium diffusivity values in Pb or NaPb or $Na_{15}Pb_4$ are in the order of 10^{-15} $cm^2·s^{-1}$ (Table 1.9). However, only limited experimental results regarding the Na diffusivity in these alloys have been reported. Abel et al estimated the Na diffusivity in Ge to be ~10^{-14} $cm^2·s^{-1}$ and in sodiated Ge to be ~10^{-13} $cm^2·s^{-1}$ (Table 1.9) by electrochemical impedance spectroscopy (EIS), much lower than the theoretically reported value. In Na-Sn system, the Na diffusivity in Na_xSn was reported to range between 10^{-9}-10^{-17} $cm^2·s^{-1}$ [104]. The Na diffusivity in Pb and $Na_{15}Pb_4$ is reported to be in an order of 10^{-16} and 10^{-17} $cm^2·s^{-1}$, respectively. In addition, it is worth mentioning that while conventional electrochemical methods such as galvanostatic intermittent titration technique (GITT), potentiostatic intermittent titration technique (PITT) and EIS are commonly employed to interpret the Na diffusion kinetics in alloy anodes, the reliable sodium diffusivity in Na-M_{IVA} is difficult to be extracted from these electrochemical measurements in two-phase transformation regions since the concentration gradient is not the only governing factors.

Mechanical properties. Although no experimental results regarding the mechanical property of Na-M_{IVA} alloys have been reported up to now, the DFT calculation predicted that the sodiation of M_{IVA} (Si, Ge, Sn, and Pb) alloys will lead to a significant decrease in their elastic moduli [105] (Table 1.9), due to the weaker interatomic interactions. This implies an increased capability of elastic deformation for Na-M_{IVA} alloys compared to pure M_{IVA} alloys. Besides, the mechanical ductility (or brittleness) is also calculated theoretically, as shown in Table 1.9. Both pure Si (or Ge) and its sodiated phase NaSi (or NaGe) are brittle, as supported by the low B/G ratio (Table 1.9). In contrast, pure Sn and Pb, with a high B/G ratio, are highly ductile. Differently, a small variation is observed in the B/G ratio with the sodiation of Sn. Thereby it is hard to predict which Na-Sn phases are brittle or ductile. However, as the sodiation of Pb proceeds, the sodiated Na_xPb alloys (particularly $x \geqslant 1$) seem to become more brittle, as evidenced by the significantly decreased B/G ratios.

Table 1.9 The chem-mechanical properties of M_{IVA} and Na-M_{IVA} (M_{IVA}=Si, Ge, Sn, Pb) alloys

Elements		Bulk modulus (B) /GPa	Elastic modulus (E) /GPa	Shear modulus (G) /GPa	B/G	Predicted Na diffusivity / $cm^2 \cdot s^{-1}$
Na-Si	Si	99.20[a]	164.80	67.30	1.47	~10^{-9}[101]
	NaSi	22.99	36.59	14.82	1.55	8.13×10^{-9}[88]
Na-Ge	Ge	76.80[a]	135.00	55.90	1.37	~9×10^{-1}[89]; ~10^{-13}[106]
	NaGe	16.15	39.17	18.25	0.88	2.87×10^{-8}[101]
Na-Sn	Sn	45.00[a]	51.01	17.93	2.51	~5×10^{-10}[107]
	$NaSn_5$	29.20	42.10	16.71	1.74	N/A
	NaSn	17.27	25.63	10.23	1.85	2.1×10^{-9}[108]
	Na_9Sn_4	18.91	24.11	9.38	2.01	N/A
	$Na_{15}Sn_4$	13.83	15.01	5.69	2.42	N/A
Na-Pb	Pb	38.50[a]	33.70	12.20	3.16	~10^{-16}[109]
	$NaPb_3$	32.94	23.23	8.43	3.90	N/A
	NaPb	15.04	24.54	9.99	1.50	~5×10^{-15}[82]
	Na_9Pb_4	N/A	N/A	N/A	N/A	N/A
	$Na_{15}Pb_4$	13.14	17.14	6.68	1.96	~1×10^{-17}[82]

Note that the mechanical parameters of Na_xM (M=Si, Ge, Sn, Pb) are obtained by DFT calculation [105].

1.4 Objectives

The primary goal of this thesis is to provide insights into the underlying sodiation mechanism and kinetics of Si-/Ge-/Sn-/Pb-based alloy anodes, aiming at enabling the utilization of alloy anodes for sodium-based batteries. While group IVA alloys are expected to increase the volumetric energy density of SIB anodes, they are poorly understood. Hereby, systematic investigations are conducted on the (de-)sodiation behavior of these alloys in this thesis to reach the goal, with the detailed aims summarized as below:

a. To enable the electrochemical sodiation of Si electrodes, by increasing temperature, introducing other active/inactive elements, and creating a porous structure.

b. To elucidate the kinetics and mechanisms of electrochemical sodiation of Ge thin film electrodes, by conducting robust potentiostatic analyses.

c. To provide an insight into the limiting factors for poor electrochemical performance of Sn foil electrodes through a systematical kinetic study using in-situ electrochemical impedance techniques.

d. To understand the origin of capacity degradation of Pb foil electrodes by the exploration of phase transformation reversibility, coupled with the structural analyses, and provide guidance for the future development and utilization of Pb foil electrodes.

Accordingly, this thesis primarily focuses on the following: **Chapter 1** provides a general overview of the development and challenges of SIB and presents the research motivation and content. **Chapter 2** outlines the experimental procedures for electrode preparation and (coin-/symmetric-/3-electrode) cell assembly, and introduces the experimental methods and electrochemical techniques used, as well as the theoretical basis for analysis of these techniques. **Chapter 3** examined the electrochemical sodiation of Si-based anodes, at elevated temperatures or after structural engineering. **Chapter 4** offers a thorough investigation of nature and kinetics of two distinct phase transformations that occur in the initial sodiation of Ge thin film electrodes. **Chapter 5** introduces the in-situ impedance technique for the kinetics study of Sn foil anodes in the (de-)sodiation. **Chapter 6** explored the electrochemical reactions and morphology change of Pb foil electrodes during the (de-)sodiation, as well as the reversibility of each phase transformation. **Chapter 7** summarizes the findings obtained in this thesis and proposes possible directions for further investigation into group IVA elements in the future.

Chapter 2: Research Methodology

2.1 Electrode Preparations

Three kinds of electrode, namely metallic foil, thin film, and slurry-cast composite ones are used here for our study. For the foil electrode, Pb (30 μm-thick) and Sn (30 μm-thick) foils are all purchased and directly used as the precursor for the working electrode. Differently, the Ge (or Si) thin film electrodes were prepared by sputtering Ge (or Si) on the substrate of Cu foil at room temperature. The sputtering target is a high-purity Ge (3 inches, 99.9999%, SENTE MATERIAl) or Si target (3 inches, 99.999%, Kurt J. Lesker). For all the depositions, the base pressure was kept at 8×10^{-7} Torr, the working power was maintained at 160 W (radio frequency (RF) mode), and the working pressure during the deposition was kept at 6.6 mTorr. The thickness of as-sputtered Ge thin film is calculated by the weight difference to be ~850 nm, corresponding to the theoretical capacity of about 0.041 $mAh \cdot cm^{-2}$ for $NaGe_4$, 0.16 $mAh \cdot cm^{-2}$ for NaGe, and 0.49 $mAh \cdot cm^{-2}$ for Na_3Ge, respectively.

The slurry-based $Na_3V_2(PO_4)_3$ (NVP) electrode was prepared as follows. First, a certain amount of polyvinylidene difluoride (PVDF) powder was dissolved in N-Methyl-2-pyrrolidone (NMP) solvent to make a 5 wt% PVDF solution. Later, the NVP powder, carbon black powders, and PVDF in a mass ratio of 85%, 5%, and 10% were weighed and mixed in a plastic jar at 1500 rpm for 25 min. The obtained slurry was then coated on the Al current collector and dried in a vacuum oven at 90 °C for 24 h. The dried NVP sheet was pouched into discs with a diameter of 12 mm for the later assembly. The mass loading for the NVP electrode is about 1 $mg \cdot cm^{-2}$.

2.2 Cell Assembly

Coin-cells. All the cells are assembled in a 2025-type or 2032-type coin-cell configuration in an Ar-filled glovebox (<0.5 ppm H_2O and O_2). As for the half-cells, the Sn and Pb foil, or as-sputtered Ge (or Si) thin film was punched into disks with a diameter of 12 mm for the working electrode, while the pure Na metal foils were used for the counter electrode for Na-ion half cells. Glass fiber and 1 M $NaClO_4$ in EC: PC = 1:1 vol% are used as the separator and electrolyte for the cells, respectively. Besides, a stainless steel (SS) wave spring and an SS spacer (1 mm thick) were used to keep the stack tight.

The assembly of the NVP//Pb full cells follows the same procedures as that of half-cells, but the NVP cathode is used to pair against the Pb foil anode. To effectively avoid any catalytic reaction of Pb with the electrolyte, a piece of Na metal is pressed onto the Pb foil electrode for approximately 40 min before cell assembly, such that a new interface between the electrode and electrolyte is formed. The open-circuit voltage of the full cell with the NVP cathode and presodiated Pb foil anode is measured to be ~2.5 V at first and drops to ~2.4 V after the 10 h rest.

For the Na//Na and Na_xSn//Na_xSn symmetric cells, the cell design is the same as above, while two identical working and counter electrodes (i.e., the same composition and size) are used here. Specifically, in case of Na//Na cells, two Na metal foils are separated by glass fiber. To make the Na_xSn//Na_xSn symmetric cells, two Swagelok cells with Sn and Na foil electrodes are disassembled after each cell achieves the desired capacity or reaches to the desired potential. Subsequently, the obtained Na_xSn electrode was re-assembled in a coin-cell configuration. Notably, all assembled coin cells were rested for 12 hours before the measurements to ensure that the electrode was fully wet.

Three-electrode Swagelok Cells. The schematic illustration of the three-electrode Swagelok cells design is shown in Figure 2.1. Each Swagelok cell is composed of a Sn foil (working electrode), two Na-metal chips (one for the counter electrode and one for the reference electrode), as well as a glass-fiber separator, an SS spring, and a spacer. The Sn working and Na counter electrodes have a diameter of 10 mm while the Na reference electrode and separator are 6 mm and 14 mm in diameter, respectively. It is noted that a thick Cu foil (thickness: 1mm, diameter 12 mm) is used as the spacer. All the cell components (i.e., spacers, electrodes, and separators) were centered and packed together after screwing tightly the configuration. A conventional electrolyte of $NaClO_4$ in EC: PC=1:1 vol% is used and the volume is around 200 µl.

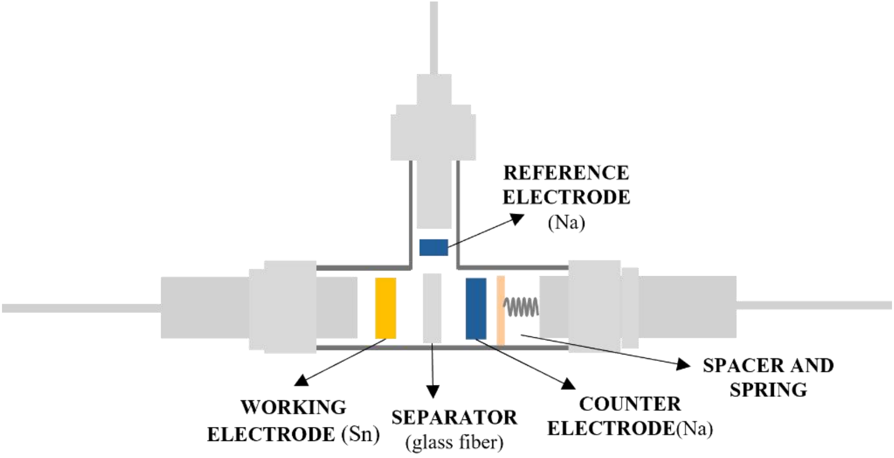

Figure 2.1 Schematic illustration of three-electrode Swagelok cell set-up.

2.3 Robust Electrochemical Techniques

2.3.1 Potentiostatic Chronoamperometry

The potentiostatic chronoamperometry (CA) is a robust technique to understand the nature and kinetics of the electrochemical reactions in electrode materials, in which a cathodic or anodic potential step (Figure 2.2a) is applied across the two-phase equilibrium potential and the current responses as a function of time at the fixed driving force is monitored simultaneously. Figure 2.2b shows an example of the typical current-time curve during the potentiostatic process, featured by a ‘current hump’ when the electrochemical reaction is dominated by the nucleation and growth process [110]. At the beginning of chronoamperometry, the current drops abruptly, which reflects the electrical double-layer behavior in the electrode/electrolyte interface. Subsequently, the current response begins to increase at point (a), which represents the threshold of nucleation of a new phase. As time goes on, the current undergoes a continuous increase due to the increased number of phase boundaries till the maximum value at point (b). Afterward, the current response decreases monotonously with time, indicating the merging of smaller nuclei of the new phase into a larger one. The process will be finalized at point (d) where the current response decreases to nearly zero.

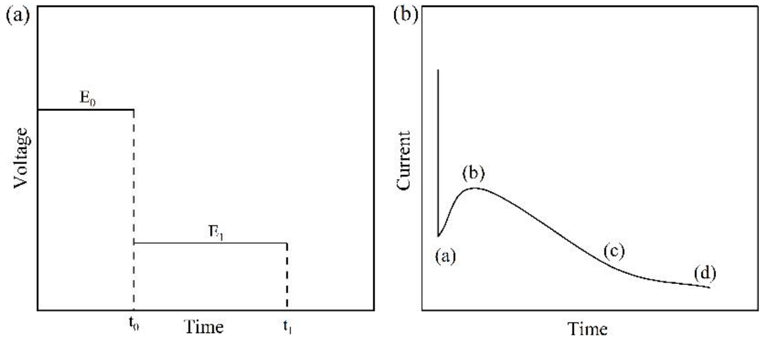

Figure 2.2 Schematic illustration of (a) potentiostatic operation, (b) the typical current response for the electrochemical reaction governed by nucleation and growth as a function of time during the potentiostatic process.

A detailed analysis of the chronoamperogram can be conducted on the basis of the Kolmogorov-Johnson-Mehl-Avrami (KJMA) theory. Conventionally, the KJMA model is established for describing the kinetics (e.g., the reaction rate) of solid-state isothermal phase transformation in metals(e.g., crystallization). But currently, it is also extended to interpret the kinetic of phase transformations in electrochemical reactions in the lithium or sodium systems (e.g. Li-Si [111], Li-Ge [112], and Li-$LiFePO_4$ [110]). The KJMA equation describes the change in the fraction of the new phase with time during the potentiostatic process, as follows [110, 113]:

$$f = 1 - \exp(-kt^n) \qquad (1)$$

Here, f is the volume fraction of one phase that has been transformed to another phase (e.g., the extent of transformation of $NaGe_4$), which can be approximately calculated by the ratio of the charge to total charge contributed by the whole reactions). k is the rate constant of the phase reaction, which is determined by the nucleation and growth rate, the rate-limiting step and the geometry of new phase [114]. n denotes the Avrami constant, and t is the time during the potentiostatic tests. To readily obtain the rate constant k, Avrami constant n, the KJMA equation is rewritten as follows:

$$\ln(\ln 1/(1-f)) = \ln k + n \ln t \qquad (2)$$

Therefore, the Avrami constant n and the rate constant k can be determined from the plots of $\ln\ln 1/(1-f)$ against ln t, where the slope corresponds to the Avrami constant n and the intercept corresponds to ln$k$. For the Avrami constant n that is directly related to nucleation and growth, it is decided by three important factors:

$$n = a + bc \qquad (3)$$

where *a* is the nucleation index, *b* reflects the dimension of growth and *c* indicates the rate-limiting step of the phase transformation. The nucleation index *a* indicates the nucleation rate as a function of time. For instance, if *a* is zero, it means that the nucleation rate during the phase transformation is zero. If *a* is more than zero but less than 1, the phase transformation proceeds with a decreasing nucleation rate as the time flows. $a = 1$ means a constant nucleation rate while $a > 1$ implies an increasing nucleation rate. The index *b* implies the dimension of growth: b=1, 2, and 3 represent the one-dimensional(1*D*), two-dimensional (2*D*), and three-dimensional (3*D*) growth, respectively. The growth index *c* indicates whether the growth process is limited by diffusion (c=0.5) or phase boundary movements (c=1). Figure 2.3a shows the typical chronoamperometry curves described by the KJMA model with the Avrami constant n=1, 1.3, 1.6, and 2 [110]. For the case of $n<1$, the chroamperogram is featured by a monotonic current decrease, which suggests that the phase transformation probably behaves as a non-equilibrium solid solution [110]. An example is the amorphous Si to amorphous Li_xSi transformation: the chroamperometry curves show the characteristic of current monotonically decreasing as time, and the sodiationof Si to Li_xSi is found to probably proceeds through a moving sharp interface (Figure 2.3b) [111]. For the case of n>1, the chroamperogram is characterized by an initial current density increase followed by a gradual decrease, namely, a 'current hump' feature. This implies that nucleation and growth play a significant role in the electrochemical reaction kinetic [110]. Figure 2.3c and d show the two examples of phase transformation models in a system with n>1 (e.g., the first-order transformation between two amorphous Li-Si phases with different Li contents [111]).

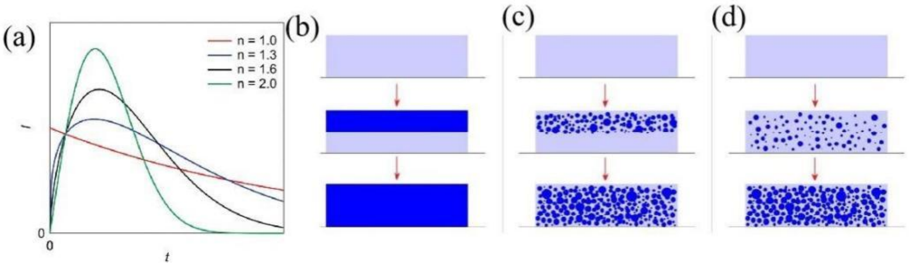

Figure 2.3 (a) The CA curves described by the KJMA model with different Avrami constants *n* [110]. The phase transformation models illustrating the cross-section of the Si electrode [111], (b) the phase propagation with a sharp interface, (c) phase transition involving nucleation and growth that initially occurs near the top surface of the film and then a nucleation front propagates through the film, and (d) nucleation and growth that occurs uniformly through the film.

2.3.2 Electrochemical Impedance Spectroscopy

Electrochemical impedance spectroscopy (EIS) is a simple and powerful technique to investigate the mass transport or charge transfer kinetic in an electrochemical system since it allows us to separate different physical and electrochemical processes (e.g., ionic diffusion) based on their time response across the applied frequency range. The essential of the impedance measurement is to apply a small amplitude potential or current stimulus (normally sinusoid) to the cells and simultaneously measure the response (current or potential) across a wide frequency range [115]. Then the impedimetric data at different frequencies can be obtained based on the Ohm-like relationship between the applied voltage (or current) and their response after a Fourier transformation of these current and voltage data: $Z(i\omega)=V(i\omega)/I(i\omega)=V_mI_m\exp(i\theta)$ [116]. Noteworthy, the EIS measurement is normally conducted under the steady conditions of the cell system. Further, the applied excitation should be small enough to ensure the linear system so that reliable impedance can be obtained. To visualize the impedance for better analysis of the electrochemical behavior, the Bode plot, where the total impedance and phase are plotted as a function of frequency (i.e., |Z|=*f*(ω) and -phase=*f*(ω)), or Nyquist plot which describes the real part of the impedance versus the imaginary part at each frequency (i.e. $-Z''=f(Z')$) is generally used as the representation of the impedance spectra [117]. The former provides a clear matching of impedance with the applied frequency, while the use of the Nyquist plot allows for the preliminary prediction of the elements in the electrical circuit involved in the system according to the plot shape [116], despite the lack of direct frequency information.

Analysis of impedance data by electrical-circuit model fitting. To understand the specific electrochemical processes involved in the system deeply, the equivalent circuit model, in which every element represents one physical characteristic of the system, is employed to simulate the impedance data and translate these abstract data into concrete physics or electrochemical processes. Figure 2.4 shows the typical Nyquist plot of simple systems with different electrical circuit models. In theory, the Nyquist plot will be characterized by a point in the real axis when only a pure resistor (R) is included due to its independence of frequency (Figure 2.4a). In contrast, for a model only containing an ideal capacitor (C), the Nyquist plot behaves like a vertical line in the imaginary axis (Figure 2.4b). In a circuit composed of a resistor and capacitor that are connected in series, the Nyquist plot is the combination of plots of the former two cases (Figure 2.4c). Differently, when the circuit contains a resistor and capacitor connected in parallel (Figure 2.4d), the Nyquist plot is featured by a semicircle. It is worth mentioning that in the non-ideal system, as the electrode surface is normally not perfectly flat, which gives rise to non-ideal capacitive behavior, thereby causing a 'depressed semicircle' in the Nyquist plot of the system with an R-C electrical circuit model.

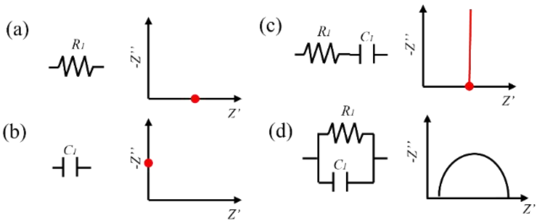

Figure 2.4 Examples of typical Nyquist and Bode plots of some electrical circuits [115].

In a real electrochemical system, the case is more complex. For an electrochemical cell that involves oxidation/reduction (Faradic) reaction, the total monitored current during the impedance measurement is the sum of two parts of current contributed by the double-layer charging/discharging (i_c) process and the Faradaic behavior (i_F). Generally, the Faradaic process includes the mass transfer, and the diffusion of ions from the electrolyte to the electrode surface passivation layer and inside the electrode, which is usually represented by an equivalent circuit called the Randles circuit as shown in Figure 2.5a. Mathematically, the impedance of the Faradaic process can be expressed as: $Z_F = R_{ct} + Z_W$, where R_{ct} denotes the charge transfer resistance related to the transfer kinetic, and Z_w is the Warburg impedance associated with ions transport. In the high-frequency region, the C_{dl} and R_{ct} are significant, and the Z_w is negligible, thus the equivalent circuit of the system can be simplified in Figure 2.5b. Under this circumstance, the relationship between Z' and Z'' is approximately expressed as: $(Z' - R_{ohm} - R_{ct}/2)^2 + (Z'')^2 = (R_{ct}/2)^2$ [115], which explains the semicircle shape of the Nyquist plot at a high-frequency region (Figure 2.5d). On the contrary, at low frequencies, the impedance of double-layer charging (C_{dl} in Figure 2.5c) is extremely high so that the current flows through the elements R_{ohm}, $R_{ct,}$ and Z_w. In this case, the relation between the real and imaginary part of the impedance can be described as below when the frequency is close to zero: $-Z'' = Z' - R_{ohm} - R_{ct} + 2\sigma^2 C_{dl}$. Thus, the Nyquist plot at low frequency behaves as a straight line with a slope of 45 degrees (Figure 2.5e) [115]. Therefore, for an electrochemical system (i.e., Li-ion batteries) the Nyquist plot over a wide frequency range normally consists of semicircles (charge transfer is dominant in the electrochemical process) and straight line (mass transports kinetic is rate-limiting), as shown in Figure 2.5f.

However, the ideal semicircle and 45-degree straight line can be observed experimentally only in the electrode with an extremely flat surface (e.g., liquid Hg) [115]. In real electrochemical systems, many components are involved, and the electrochemical processes are relatively complicated, the impedance contributed by these processes might be overlapped at frequencies. In this regard, one may struggle to determine the equivalent circuit for interpreting the physical or electrochemical characteristics of the system. Some studies mentioned that in Li-ion batteries it is a bit difficult to distinguish the resistance of solid-state interphase and charge transfer in the mid-to-high frequency region [118] unless the batteries are in the blocking zone (e.g., fully charge/discharge state), where the charge transfer is largely blocked so that the low-frequency impedance could be viewed as the contribution of the charge transfer process. Despite the limitation, we cannot deny that the simulation of electrical circuits is useful for the interpretation of impedance spectra at present.

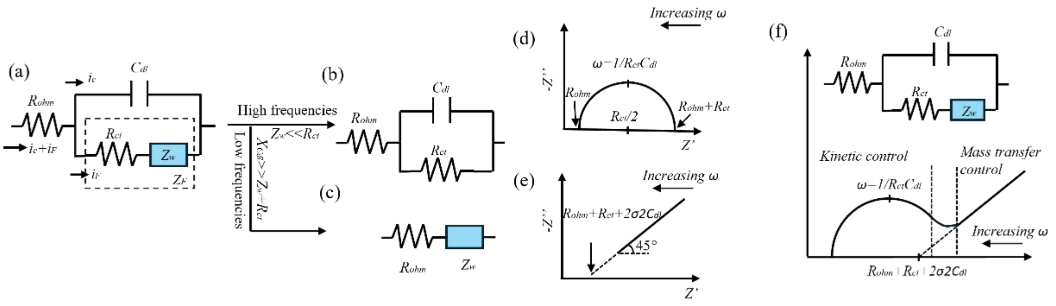

Figure 2.5 (a) The typical Randle circuit. (b)(c) The equivalent electrical circuit at low-/high-frequencies and (d)(e) corresponding Nyquist plots. (f) The common Nyquist plot for the system with a Randle circuit.

Since the electrochemical behavior in the low-frequency region is usually governed by ion transport, one can extract the ion diffusion coefficient from the Warburg impedance analysis. At low frequencies, the real (Z') and imaginary (Z'') part of the impedance can be approximately described as [119]:

$$Z' = \sigma\omega^{-0.5} + R_{ohm} + R_{ct}$$

$$-Z'' = \sigma\omega^{-0.5} + 2\sigma^2 C_{dl}$$

Where σ denotes the coefficient of Warburg impedance, ω is frequency, and R_{ohm}, $R_{ct,}$ and C_{dl} represent the ohmic resistance, charge transfer resistance, and capacitance originating from double-layer charging, respectively. Both Z' and Z'' are proportional to the inverse of the square root of the frequency in the low-frequency region and the slope of Z' (or Z'') versus $\omega^{-0.5}$ plots gives the coefficient of Warburg impedance (σ). Assuming that the electrochemical system follows a one-dimension diffusion model, the chemical diffusion coefficient of ions (D) can be derived from the coefficient of Warburg impedance σ by solving the partial differential equations of Fick's second law consider semi-infinite diffusion [119]:

$$D = \left(\frac{RT}{\sqrt{2}F^2\sigma C}\right)^2$$

Here R, T, F represent gas constant, temperature, and Faraday constant. σ is the Warburg coefficient, and C denotes the concentration in the electrolyte.

2.3.3 Distribution of Relaxation Time (DRT) Technique

While the use of the electrical circuit simulation is efficient and useful to interpret the electrochemical kinetic, it requires solid knowledge regarding the impedance technique and the electrochemical system to choose a suitable electric circuit for accurate interpretation, especially for the complex impedance spectra. DRT is a recently developed technique that uses mathematical methods to transform the frequency-dependent impedance spectra into a relaxation time-based DRT spectrum [120], aiming to more accurately distinguish different electrochemical processes. The relation between the impedance and the relaxation time is written as [120]:

$$Z(\omega) = R_0 + \int_0^\infty \frac{\gamma(\tau)}{1 + j\omega\tau} d\tau$$

Noteworthy, this equation is valid only when the impedance measurements meet the requirement of linearity, causality [121]. The DRT calculation is not simple since an inverse problem is required to be solved, which is very sensitive to the error of the experimental data [122]. Namely, accurate DRT analysis demands high-quality data of the impedance spectra. Many approaches have been developed to overcome this challenge, such as the Fourier transformation [123], ridged regression [122], Bayesia approach [124], etc. Figure 2.6 shows an example of the DRT analysis for the impedance data (Nyquist plot) based on the R-C model using the DRT tools freeware, where three peaks at different relaxation-time indicate three related electrochemical processes in the system [120]. In recent years some research has been focused on DRT techniques, but it is still in the early stage and more attention is needed to be paid to developing more reliable and accessible DRT techniques for deconvolving EIS spectra.

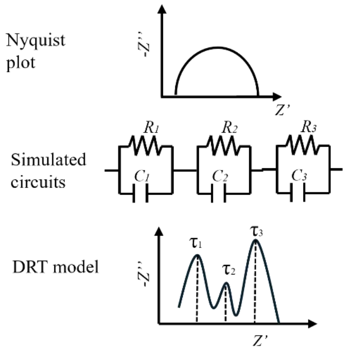

Figure 2.6 An illustration of the DRT calculation [120].

2.4 Electrochemical Measurements

All the electrochemical measurements, e.g., CA, galvanostatic charge-discharge (GCD), cyclic voltammetry (CV), and EIS, are conducted using a VMP 300 potentiostat (Biologic Technologies, France) and LAND battery testing system.

2.4.1 Cyclic Voltammetry

The cyclic voltammetry measurements were performed on the Si//Na (or Li) cells by the Biologic system at different temperatures. The scanning rate is 0.01 $mV\cdot s^{-1}$.

2.4.2 Galvanostatic Cycling

The cycling of Ge//Na half-cells was done at two C-rates (i.e., 1/100 C and 1/20 C) and the potential window during the measurement was limited to 0.001–1.5 V (vs Na/Na^+). The differential capacity (dQ/dV) curves were derived from these GCD results.

For the Pb//Na half-cells, an initial large current of 0.5 mA was applied till 0.8 V(vs. Na/Na^+) to get rid of the catalytic reaction that occurs at a relatively high voltage on the surface of the Pb electrode [79]. After that, the cells were discharged and charged at the constant current of 0.1 mA (~C/177, based on the theoretical capacity of $Na_{15}Pb_4$) at five different cut-off voltages: 0.001-0.8 V, 0.4-0.8 V, 0.15-0.45 V, 0.09-0.3 V, 0.001-0.2 V (vs. Na/Na^+). The NVP//Pb full cells were cycled in the voltage window including the (de-)sodiation plateau voltage of Pb//Na and NVP//Na half cells.

2.4.3 Chronoamperometry Measurements

The potentiostatic CA measurements in this thesis were conducted on Ge vs. Na half-cells to shed light on the nature of phase transitions that occur in the initial sodiation of Ge. Specifically, regarding the CA measurement of the first phase transition (plateau 1 in Figure 2.7a or peak 1 in Figure 2.7b), the cells were initially held at a voltage of 600 mV (E_0 in Figure 2.7b) for 4 h to largely isolate irreversible surface reactions. Subsequently, the cell voltage was adjusted to the E_1 region (e.g., in the range of 180–280 mV at room temperature (shaded region in Figure 2.7b)) and the current responses were recorded till the current value dropped to nearly zero during this process. Similarly, the CA measurements of the second phase transition in Ge electrodes (plateau 2 in Figure 2.7a or peak 2 in Figure 2.7c) were also done by applying a cathodic potential step (E_0'-E_2 in Figure 2.7c) across the two-phase equilibrium potential (the shaded region in Figure 2.7c). The first potential hold at E_0' = 250 mV is aimed to equilibrate $NaGe_4$ and the applied potential E_2 was fixed in the range of 10-110 mV during the whole CA measurement. The obtained current-time results were all quantitatively analyzed by KJMA models, which are introduced in detail in section 2.3.1.

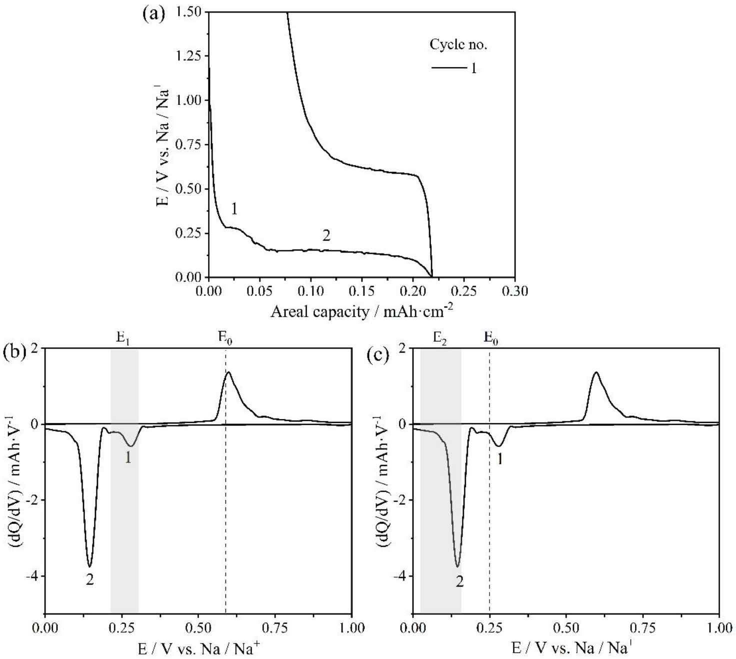

Figure 2.7 (a) The initial GCD profile of Ge thin film vs Na half-cells operating at 1/100 C at room temperature. (b) (c) The corresponding dQ/dV curves derived from Figure 2.7a. The potential chosen for CA measurements of the first phase transition are denoted as E_0 (the dashed line) and E_1 (the shadow zone) in Figure 2.7b, while the potentials for CA measurements of the second phase transition are denoted as E_0' and E_2 in Figure 2.7c.

2.4.4 Electrochemical Impedance Spectroscopy Measurements

Conventional electrochemical impedance spectroscopy (EIS) measurements of Na//Na and Na_xSn//Na_xSn symmetric cells were done at the open-circuit voltage in the frequency range of 100 kHz-5 mHz. A small perturbation amplitude of 5 mV is applied for all the cases to ensure a more accurate impedance measurement in the linear potential-current region [115]. Differently, in-situ EIS measurements of Sn electrodes at different depths of discharge (DoD) or state of charge (SoC) were conducted in a Swagelok three-electrode cell configuration at the end of each relaxation (at least 2 h to ensure the cell reached the steady state) after the galvanostatic sodiation/desodiation to desired DoD or SoC at C/100 (an example as shown in Figure 2.8). The frequency range and perturbation amplitude for the in-situ EIS measurements are 100 kHz-10 mHz and 5 mV, respectively.

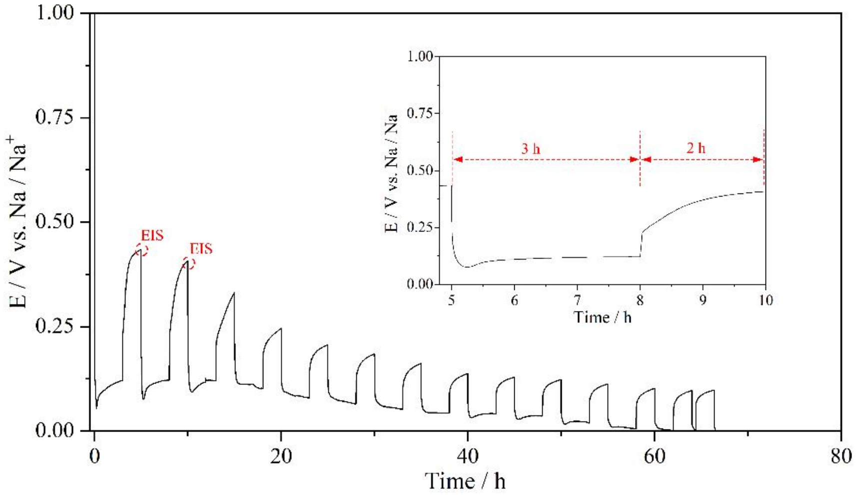

Figure 2.8 An example of the test protocol for the in-situ EIS measurements of the Sn electrode that experiences 3 h discharge followed by 2 h relaxation.

2.5 Material Characterizations

2.5.1 X-ray Diffraction (XRD)

Ex-situ XRD technique is employed to characterize the phase evolution of the Sn, Pb, Ge, or Si electrode during the (de-)sodiation process. To minimize the impact of slow sodiation kinetics on the phase composition, when the desired potential or capacity is reached, all the half-cells were held at least 2 h prior to their disassembly in an argon-filled glovebox. After the disassembly, the (de-)sodiated Sn, Ge, or Si electrode samples were then washed with pure Dimethyl carbonate (DMC) solvent and sealed in Kapton tape in the glovebox to avoid the oxidation of the electrode. Differently, a well-designed airtight holder is used to seal the (de-)sodiated Pb samples after the washing procedure. All the XRD tests were conducted at a scan speed of 5°/min in the 2θ angle range of 20°−80° at room temperature using Rigaku SmartLab 9 kW or DaVinci 1 X-ray diffractometer.

2.5.2 Scanning Electron Microscopy (SEM)

The ex-situ SEM technique was used to observe the surface morphological change of the Pb and Sn foil electrode during cycling. The electrode sample for SEM tests was obtained by disassembling the Sn//Na or Pb//Na cells sodiated to different extents and sealing them using the vacuum bag before taking them into the SEM vacuum chamber. The SEM images of the (de-)sodiated Sn and Pb were taken by using scanning electron microscopy (Tescan VEGA3) and field-emission scanning electron microscopy (Zeiss-Supra 55VP-FEG-SEM), respectively, operating at an accelerated voltage of 20 keV and working distance of roughly 10 mm.

Chapter 3: Sodium Storage Behavior of Si

3.1 Introduction

Due to the emerging success in LIBs and the high theoretical Na-storing capacity, Si is preferentially examined as the SIB anode candidate among the group IVA. While the Na-Si phases (e.g., Na_4Si_{23} and NaSi) have been reported by metallurgists (Figure 1.7) [98, 125], very little Na can alloy with crystalline Si electrochemically at room temperature perhaps due to its larger atomic size and thus constrained Na diffusion [79, 126]. Encouragingly, some theoretical calculations predict that the Na insertion into amorphous Si is more favorable thermodynamically than into crystalline Si since the larger interstitial sites of amorphous Si can readily accommodate Na atoms, resulting in a lower activation energy of -0.15 eV for nucleating the $Na_{0.76}Si$ phase [87, 127, 128]. However, experimental results have not been in agreement with the calculations, showing that even amorphous Si can hardly be sodiated [79]. This inconsistency between the theoretical and the experimental results is generally believed to be due to the sluggish diffusion of Na in Si and the low electrical conductivity of Si [87, 128]. Some endeavors have been made to overcome the kinetic limitation of Si by reducing the particle size to nanoscale, but no solid evidence confirms the Na incorporation into Si to date. In this work, we are also devoted to enabling Na insertion into Si by improving its kinetics or overcoming the kinetic barrier through different alternative approaches, such as increasing temperature, constructing porous structure by dealloying strategy, and introducing other elements into Si. While these outcomes are not encouraging, some insights into the limiting factors of the sodiation of Si are elucidated.

3.2 Results

3.2.1 The Na Insertion into Si at Ambient Temperature

The typical voltage profiles of the Si thin film electrode at 0.05 C are shown in Figure 3.1a. No sodiation plateaus are observed. Moreover, only limited reversible capacity (Ca.~0.012 $mAh \cdot cm^{-2}$) is achieved during the cycling at room temperature, implying the unfavorable (de-)sodiation behavior of Si. This is consistent with the absence of characteristic diffraction peaks (Figure 3.1b) corresponding to Na-Si phases in the XRD diffractogram of the electrode after the full sodiation (to 0.001 V vs.Na/Na^+).

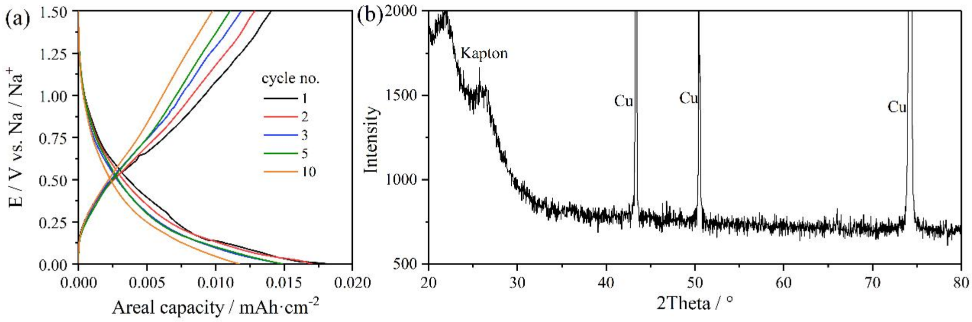

Figure 3.1 (a) GCD curves of Si anodes at 0.05 C. (b) The XRD pattern of Si anode after full sodiation.

3.2.2 The Na Insertion into Si at Elevated Temperature

As already mentioned, the slow diffusion of Na in Si might be largely responsible for the electrochemical inactivity. Therefore, higher temperatures for sodiation are expected to mitigate the kinetic issues and hopefully facilitate the sodiation of Si. Figure 3.2 compares the GCD profiles of the half cells with Si thin films as the working electrodes at various temperatures. It is found that Si is restrictedly reactive to Na, regardless of sodiation temperatures. Even at 65 °C (nearly the upper limit for the commercial rechargeable batteries), neither sodiation plateau nor evident capacity can be observed in these GCD profiles, indicating a negligible Na insertion into Si. This conclusion is further supported by the similar capacity levels observed in the dummy cell using just the bare Cu foils in the absence of Si thin films as the anode (Figs. 3.2 d-f) at the same chosen temperature. The higher capacity obtained at 50 °C and 65 °C is likely a result of the deteriorated electrolyte breakdown induced by higher temperatures.

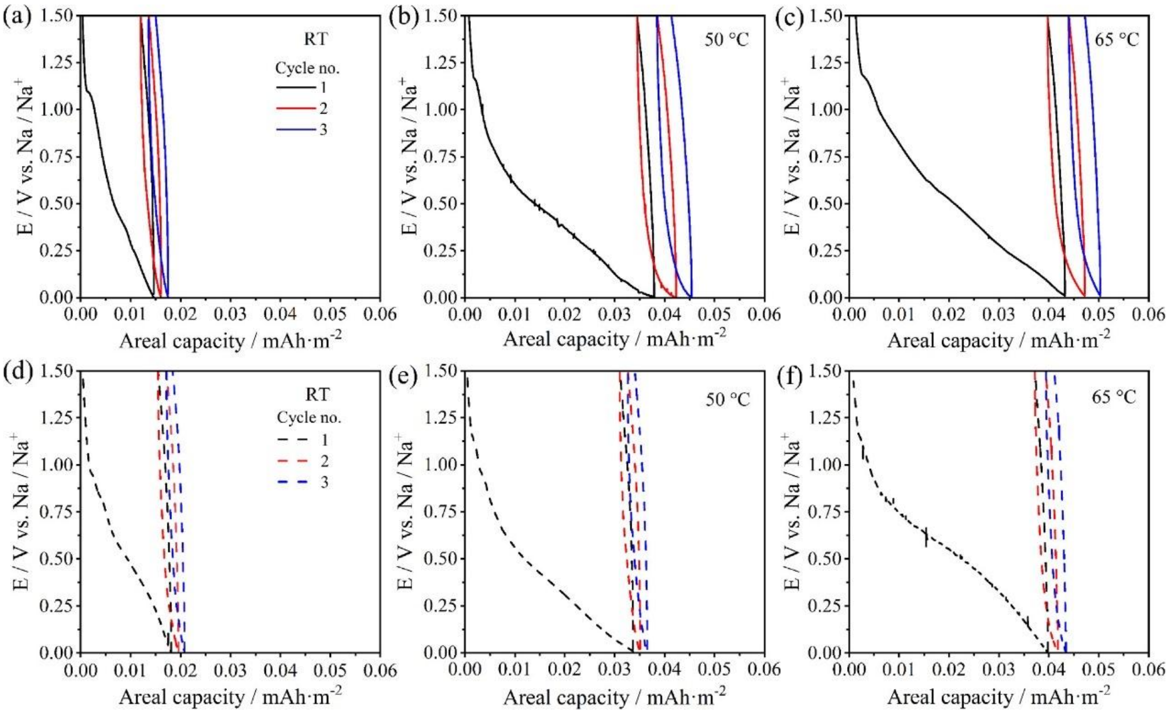

Figure 3.2 GCD profiles of the first three cycles obtained from the Si versus sodium half-cells (the solid lines) at different temperatures: (a) room temperature (RT), (b) 50 °C, and (c) 65 °C. The corresponding GCD profiles (the dashed lines) obtained from the dummy cells (bare Cu foil against Na metal) are provided in (d), (e), and (f), respectively.

3.2.3 The Na Insertion into Al-Si Alloy

Introducing Al into Si is also expected to facilitate Na insertion into Si. For one thing, the inclusion of Al will lead to an increase in the electrical conductivity of the Si electrode, thus promoting the charge transfer to some extent. For another thing, the first principal calculation predicts the great potential of NaAlSi as an SIB electrode, which has high structural stability, and will give a theoretical capacity of 476 mAh·g^{-1}

(equivalent to approximately 1200 mAh·g^{-1}, much higher than hard carbon) [129]. Experimentally, the ternary NaAlSi phase was also reported as a final product for the electrochemical corrosion of Al-Si alloy with molten Na [130, 131], although Al and Si are electrochemically inactive to Na at ambient temperature. In addition, in the analogous LIB chemistry, the ternary LiAlSi phase was proven to be the lithiated product of the Al-Si electrode at room temperature [132]. Therefore, it is anticipated that the NaAlSi phase might be formed in the electrochemical sodiation of Al-Si electrodes. In this regard, the incorporation of Al into Si could enable Na insertion into Si.

To validate our hypothesis, systematical experiments are conducted on the sputtered Al-Si thin film electrodes. Noteworthy, prior to the sodiation, the Al-Si electrode undergoes a pre-lithiation to form the LiAlSi ternary phase. The idea is to promote the formation of NaAlSi by Na exchanging with Li during the subsequent sodiation. Figure 3.3 shows the typical current vs. potential curves of the Na-ion half cells with Al-30 at% Si thin film electrode which is prelithiated to different potentials (0.01-0.3 V vs. Na/Na$^+$). One may see that all the voltage profiles show a similar shape, with no obvious reduction and oxidation peaks observed in the sodiation and desodiation process. Meanwhile, the values of sodiation and desodiation current in all cases are similar and very small, only about 2 μA. This implies that Na can be hardly inserted into Al-Si. The non-zero current in voltage profiles is assumed to be the result of the electrolyte decomposition.

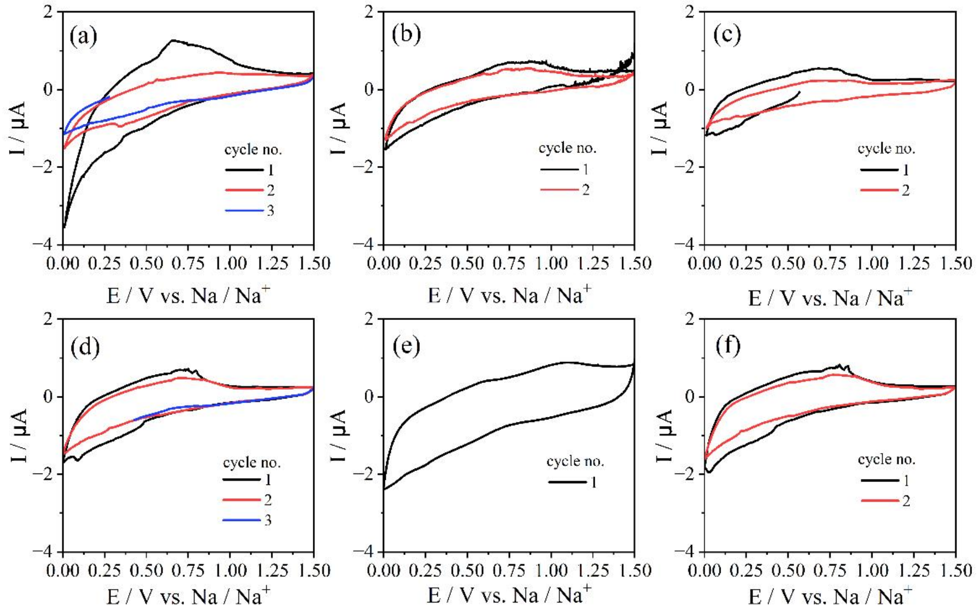

Figure 3.3 The room-temperature CV curves of Al-30at%Si thin film electrodes versus Na, after the pre-lithiation to different potentials, (a) 0.3 V, (b) 0.2 V, (c) 0.15 V, (d) 0.1 V, (e) 0.05 V, (f) 0.01 V. The scanning rate is 0.01 mV·s^{-1} and the voltage window is 0.001-1.5 V.

Other than the prelithiation depth, the composition of Al-Si is also adjusted to examine whether the sodium can be alloyed with Al-Si electrodes. Figure 3.4 compares the CV curves of Al-Si electrodes with different compositions at room temperature. Regardless of the Si content, all Al-Si electrodes display similar CV curves with small (de-)sodiation current, which indicates unfavorable (de-)sodiation behavior of Al-Si at room temperature. Even at a higher temperature (50 °C, Figure 3.5), no oxidation/reduction peaks occur during the cycling of the Al-30 at% and Al-45 at% electrodes. Meanwhile, a negligible increase in the (de-)sodiation current is obtained. This again suggests that Al-Si is hardly sodiated even at elevated temperatures. The true reasons why Si or Al-Si alloy is inactive are not clear.

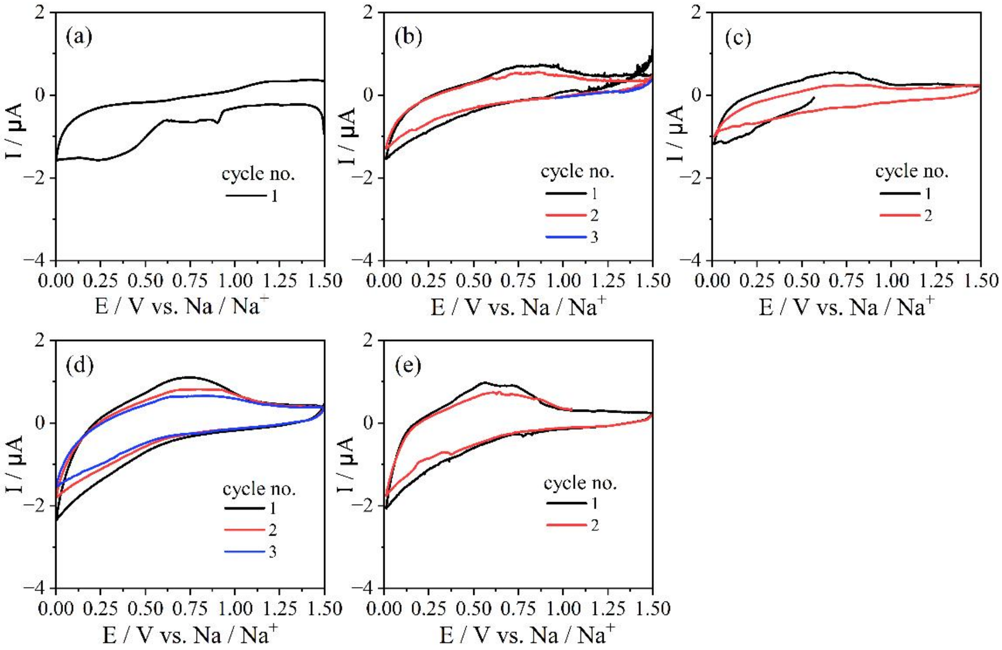

Figure 3.4 The comparison of CV curves of the Al-Si thin film electrodes with various compositions after the first prelithiation to 0.15 V at room temperature, (a) pure Al, (b) Al-10 at%Si, (c) Al-30 at%Si, (d) Al-45 at%Si, (e) pure Si.

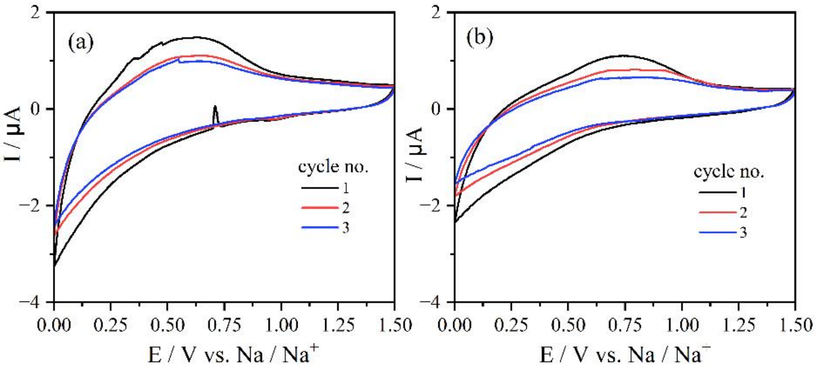

Figure 3.5 The first three CV curves of the half-cells with (a) Al-30 at%Si electrodes, and (b) Al-45 at%Si electrodes at 50 °C.

3.2.4 The Na Insertion into Chemically Etched Si

Additionally, it is well-recognized that the porous structure is beneficial to the lithiation or sodiation process since this configuration could provide more diffusion path and shorten the ion diffusion distance, thereby promoting sodium insertion. Herein we design porous Si electrodes by chemical etching (7wt% HCl) of Al-Si thin film to facilitate the alloying of Si with Na. An etching duration of 2 h is adopted to ensure the full reaction. From Figures 3.6a and c, the etched electrode shows little sodium-storage capability both at room and elevated temperature (65 °C), as is supported by the absence of reduction/oxidation peaks and a small current in both cases. Also, it should be pointed out that the chemical etching process is successful, because the etched electrode functions well versus lithium metal (Figure 3.6b and d). Meanwhile, their CV curves are analogous to that of pure Si electrodes vs. lithium in the literature, and the calculated specific capacity of the etched electrode versus Li is close to the theoretical one of pure Si electrode.

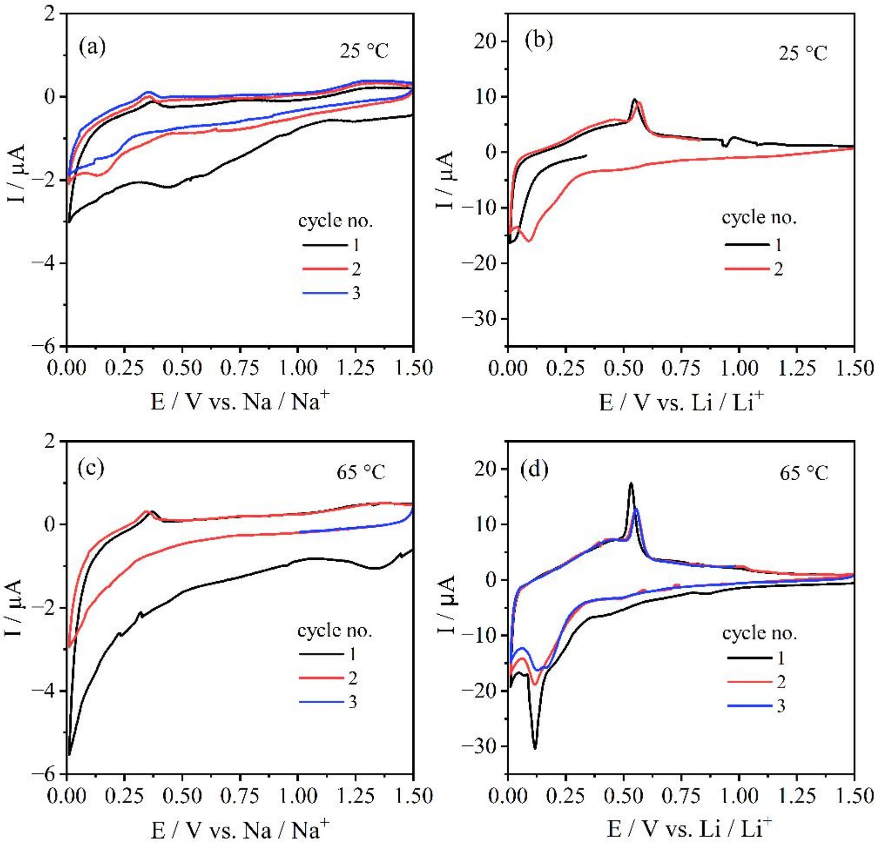

Figure 3.6 The CV curves of the chemical etched Al-30at%Si thin film electrode vs. Na or Li at 25 °C and 65 °C.

3.3 Discussion about the Sodiation of Si

While four Na-Si phases (i.e., $NaSi_{94}$, Na_4Si_{23}, $NaSi_2$, NaSi) have been reported by metallurgists [98], a complete Na-Si binary phase diagram has not been established to date [125]. Among these four phases, NaSi is suggested to be approachable via electrochemical sodiation based on the theoretical calculations, delivering a capacity of 954 $mAh\cdot g^{-1}$ [92]. However, this capacity value is not observed in our experiments regardless of whether the sodiation is carried out at room or moderate temperatures. In fact, this 954

$mAh \cdot g^{-1}$ has never been achieved experimentally in the previous reports. For instance, a study reports that Si shows very little electrochemical activity to sodium at room temperature [126]. Given the presence of multiple Na-Si phases, researchers commonly believe that the sluggish diffusion of sodium should be largely responsible for the unfavorable sodiation of Si [128]. Thereby, Obravoc et al. attempted to activate Si by increasing temperature but found that Si is still inactive to sodium electrochemically at temperatures up to 60 °C [79]. Consistently, our results also show that Si does not work in functioning as SIB anodes at elevated temperatures (e.g., 65 °C). Even at 80 °C, only very limited reversible capacity can be obtained during the electrochemical sodiation/desodiation processes of Si [133]. These negative outcomes indicate that the unfavorable sodiation of Si may be caused by a combination of many factors, in addition to the slow diffusion of Na in Si. For instance, the limited interstitial spacing and the weaker attractive interaction of Na-Si than Na-Na at a local Na-rich region [87] could be also responsible. Overall, the electrochemical sodiation of Si has not been successful to date, despite the presence of the Na-Si phases.

3.4 Conclusion

To summarize, Si is found to be hardly sodiated electrochemically even at 65 °C. The incorporation of Al into Si doesn't enable the insertion of Na into Si both at room and elevated temperatures. Besides, the Al-Si electrode after etching shows little Na storage capability even at 65 °C. The underlying reasons why Si cannot store sodium remain unclear. Further explorations of the alloying behaviors of Si or Si-based alloys with Na at higher temperatures or extremely low C-rates are required to understand the critical factors which limit the sodiation of Si in the future.

Chapter 4: Sodiation Kinetics of Ge

4.1 Introduction

From the above chapter, the sodiation of Si remains a "black box" at the end of the day, in which multiple Na-Si phases do exist, but none is observed electrochemically. Alternative ways of exploration are therefore required to understand why the electrochemical sodiation of Si is not generally observed. Ge, the neighboring element of Si in group IVA in the periodic table, shares the same crystal structure (i.e., face-centered cubic), bonding mechanisms with Na (i.e., monoclinic NaSi and NaGe Zintl phase), and valence electron configurations ($3s^2p^2$ for Si vs $4s^2p^2$ for Ge) as Si. Furthermore, the lithiation mechanism of Ge is analogous to that of Si. This analogy may be parallelly supported by swapping Na with Li. As a result, it is anticipated that the understanding of the electrochemical sodiation of Ge may help shed light on the limiting factors of the electrochemical sodiation of Si for analogous reasons.

Ge production is inherently tied to industrial Si refinement, implicating an intrinsic cost disadvantage compared to other raw materials [134]. Nevertheless, amorphous Ge is observed to exhibit some electrochemical activities in regard to Na experimentally, i.e., it can be electrochemically sodiated [89, 90], and this warrants further understanding regarding its energy storage capability pathways. Aside from pure amorphous Ge, most SIB-related explorations focus on improving electrochemical performance through some type of chemical, geometric, or processing modification approach. For instance, some researchers incorporate other elements (e.g., Te, P, Cu, and Co) into Ge and successfully improved the rate capability and cycling performance of Ge [135-138]. Chung et al. designed a novel 3D Ge/Si core-shell nanorods with TiN/Ti thin film and found the cycling stability is significantly improved by this 3D favorable structure [139]. Wei et al. constructed the highly dispersed Ge quantum dot which can maintain ~80% initial capacity after 5000 cycles even at a 3 C rate [140]. Furthermore, pre-alloying tricks are employed to make Ge more susceptible to sodiation. It is found that the Ge nanowires, which are amorphized by precycling with Li, have a lower energy barrier for nucleating Na_xGe phases [106]. The effectiveness of this pre-alloying trick is also proved by an in-situ transmission electron microscopy (TEM) study, in which the volume expansion of the sodiated Ge ($Na_{1.6}Ge$) is nearly 300%, and nanopores are observed after desodiation [90]. However, nanowires might not be fully representative due to their size effect, i.e., single crystalline or bamboo structure. At the end of the day, the sodiation mechanisms and kinetics of pure Ge as a chemical element can hardly be extracted from these studies, although very promising performances are achieved from these literature.

Herein, for the first time, we conduct systematic kinetic analyses on the two possible phase transitions that occur in the initial sodiation of Ge electrodes by using the potentiostatic technique, with the aim of providing insights into the sodiation mechanisms and diffusion kinetics of Na in (sodiated) Ge. A quantitative analysis using the Kolmogorov-Jonson-Mehl-Avrami (KJMA) model reveals that the irreversible Ge/$NaGe_4$ phase transition is controlled by the Na diffusion, proceeding through a sharp interface propagation, whereas for the reversible $NaGe_4$/$Na_{1+x}Ge$ phase transition, the movement of the reaction front (i.e., phase boundary) is the rate-limiting step, and it proceeds via a nucleation-growth model. Not only does the collected data fill out the research gap regarding the electrochemical kinetics of Na-Ge systems, but they may also shed light on important transport and reaction characteristics of any new anode material that may be found in a future SIB.

4.2 Results

4.2.1 Effect of Rate/Temperature on (De-)Sodiation of Ge

According to the Na-Ge phase diagram [99], there exists three intermetallic compounds, namely, $NaGe_4$, NaGe, and Na_3Ge, delivering theoretical capacities of 92 $mAh{\cdot}g^{-1}$, 369 $mAh{\cdot}g^{-1}$, and 1107 $mAh{\cdot}g^{-1}$. Figures 4.1a and 4.1b present the GCD profiles of Ge thin film electrodes which are cycled against Na metal at a commonly low-rate of 1/20 C and a further slow rate of 1/100 C at room temperature. One can see that there is one long and flat plateau centred at ~0.12 V (vs Na/Na^+) during the initial sodiation at 1/20 C (Figure 4.1a), which is assumed to be responsible for the Na insertion into Ge to form the NaGe phase [89, 90, 141], incorporating the findings from the dummy cell. For the subsequent cycles, the sodiation plateau slightly rises to ~0.15 V (vs Na/Na^+), indicating the enhanced reaction kinetics after the initial cycle but with less sodiation capacities. When the direction of the applied current is reverted (i.e., desodiation), the Na extraction is observed to happen at around 0.6 V (vs Na/Na^+) regardless of the cycle number. These plateaus correspond to the distinct peaks at the same potential in the dQ/dV curves in Figure 4.1c. Additionally, except for noticeable irreversible capacity loss in cycle 1, less irreversible capacity is found at 1/20 C in the following cycles, implying certain reversibility for the Na insertion/extraction into Ge.

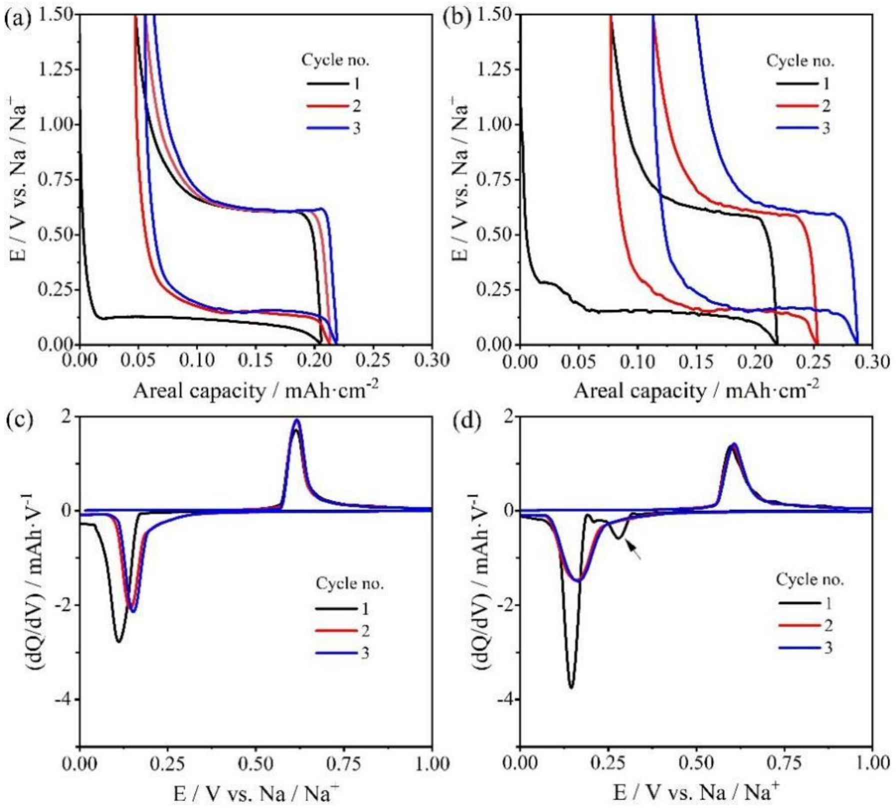

Figure 4.1 Room temperature GCD profiles of the Ge thin film electrodes obtained at (a) 1/20 C and (b) 1/100 C. The corresponding differential capacity (dQ/dV) curves for Ge electrodes obtained at (c) 1/20 C and (d) 1/100 C.

When the cycling rate slows down to 1/100 C (Figure 4.1b), in addition to the long plateau at ~0.12 V (vs. Na/Na$^+$), an extra but short plateau appears at ~0.3 V (vs. Na/Na$^+$) at the beginning of the first sodiation, which corresponds to the small reduction peak in first dQ/dV curves at 1/100 C (arrow in Figure 4.1d). Noteworthy, this short plateau disappears permanently in the following cycles, suggesting that a phase transition is perhaps taking place on this plateau and should be irreversible. Similar observation was also reported by Miao et al. in the initial lithiation of amorphous Si [142]. For the desodiation process, the same feature with only one plateau at ~0.6 V (vs. Na/Na$^+$) is observed in the GCD profiles at 1/100 C, corresponding to the oxidation peak in Figure 4.1d. As compared to 1/20 C, larger irreversible capacity loss is observed in each cycle at 1/100 C, which may be associated with the possible formation of the less reversible Na_3Ge phase at this extremely low C-rate.

The phase evolution of Ge during the initial sodiation/desodiation was examined by ex-situ XRD. No distinct diffraction peaks representing crystalline Ge or sodiated Ge are observed from all the X-ray diffractograms (Figure 4.2), indicating the low crystallinity or the amorphous nature of both pristine and sodiated Ge electrodes. Given the limitation of the XRD technique, here we attempt to determine what Na-Ge phases are probably formed during the initial sodiation by quantifying the sodiation capacity of the Ge electrode based on the electrochemical data. Despite the minor capacity of the dummy cell (only the initial cycle; Figure 4.3), we reasonably exclude this amount of capacity that is likely contributed by electrolyte breakdown to enhance the accuracy of the capacity quantification in Figure 4.4. According to the Na-Ge phase diagram [99], the first short plateau of the initial sodiation occurring at ~0.3 V is suggested to be: $Na + Ge \rightarrow NaGe_4$, which is further verified by the perfect match between the capacity obtained from the electrochemical data and the theoretical capacity calculated by the atomic ratio of the $NaGe_4$ phase. Furthermore, the second long plateau at ~0.12 V should correspond to the formation of the NaGe phase at the expense of $NaGe_4$ because the NaGe is reported to be thermodynamically stable [101]. Unexpectedly, the obtained capacity is found to be noticeably larger than the theoretical capacity of the NaGe phase, especially since the dummy cell capacity has already been excluded. Based on the electrochemical data, the final sodiated products of Ge at 1/100 C are calculated to be $Na_{1.38}Ge$, which is generally consistent with the previous report on the final sodiated phase of Ge, for example, $Na_{1.16}Ge$ [89], $Na_{1.56}Ge$ [87], and $Na_{1.6}Ge$ [90]. From the Na-Ge binary phase diagram, no equilibrium phase exists between NaGe and Na_3Ge. It is supposed that a part of NaGe may be further transformed into a higher-ordered Na_3Ge phase at local Na-rich regions.

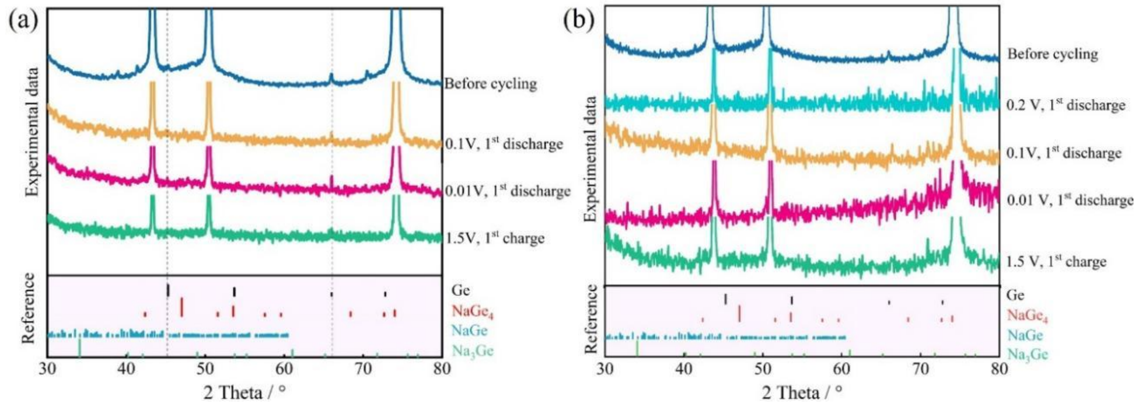

Figure 4.2 *Ex situ* XRD patterns of Ge thin electrodes after different discharge/charge depths at, (a) 1/20 C and (b) 1/100 C.

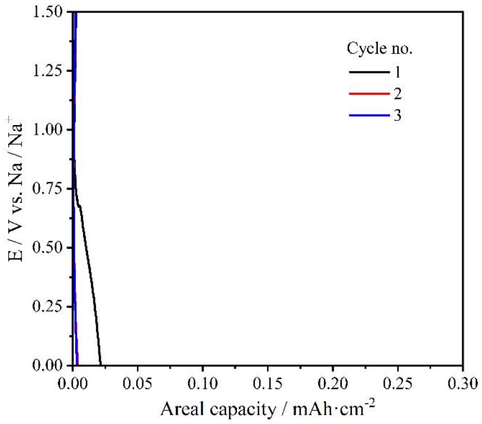

Figure 4.3 The voltage vs. capacity plots of the dummy cell measured at 1/100 C (~2 uA) at room temperature.

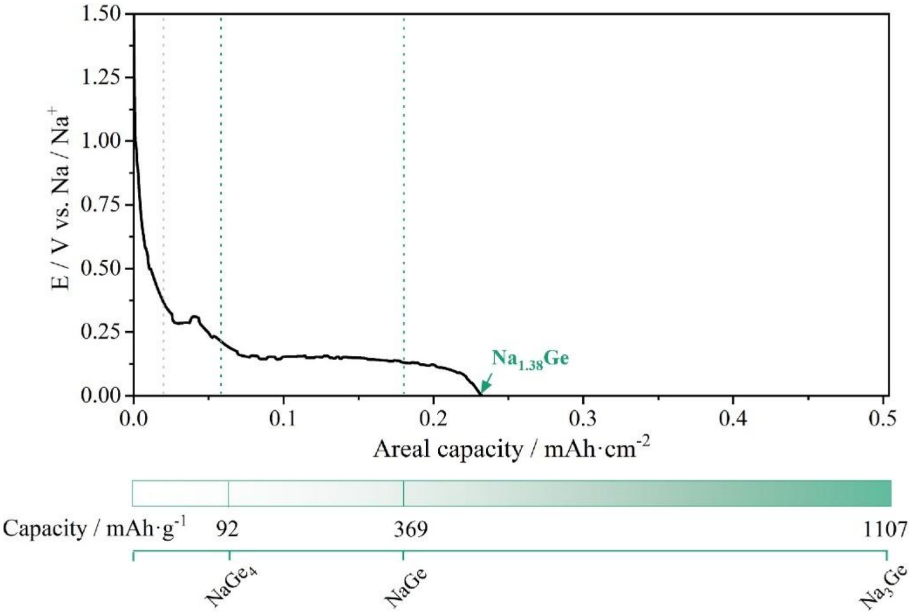

Figure 4.4 The capacity quantification of Ge thin film electrode during the first sodiation at 1/100 C (~2 µA) at room temperature, accounting for the lost, irreversible capacity of a dummy cell in Figure 4.3.

To further explore the end sodiation products of the Ge thin film electrode, the electrochemical tests are also done at elevated temperatures. Figures 4.5a-d show the first (de-)sodiation profiles and their corresponding dQ/dV curves of the Ge electrodes cycled at 1/100 C at room and elevated temperatures. In all cases, the GCD profiles seem to exhibit similar features: Two sodiation plateaus and one desodiation plateau, corresponding to the peaks in the dQ/dV curves, with the exception of the two desodiation plateaus observed at 60 °C. Taking a closer look, however, the sodiation plateaus tend to move upward as the temperature rises, of which the shift of the first one is more pronounced in the chosen temperature range. Also, the first sodiation plateau is found to become steeper at higher temperatures. These changes can be observed more easily when looking into the dQ/dV curves (annotated by the arrows), which is probably related to less energy barrier for nucleation due to the elevated activity of Ge at higher temperatures to Na [143]. Meanwhile, the GCD profiles become smoother at elevated temperatures, which is likely ascribed to the more favorable kinetics induced by higher temperatures (e.g., faster ion diffusion). Noteworthy, the anodic peak seems to split into two at around 0.6 V (vs. Na/Na$^+$) at a temperature beyond room temperature, as corroborated by two distinct anodic peaks at 60 °C. This observation is also reported in the desodiation of gallium electrodes, which is assumed to be associated with the kinetic limitation [67].

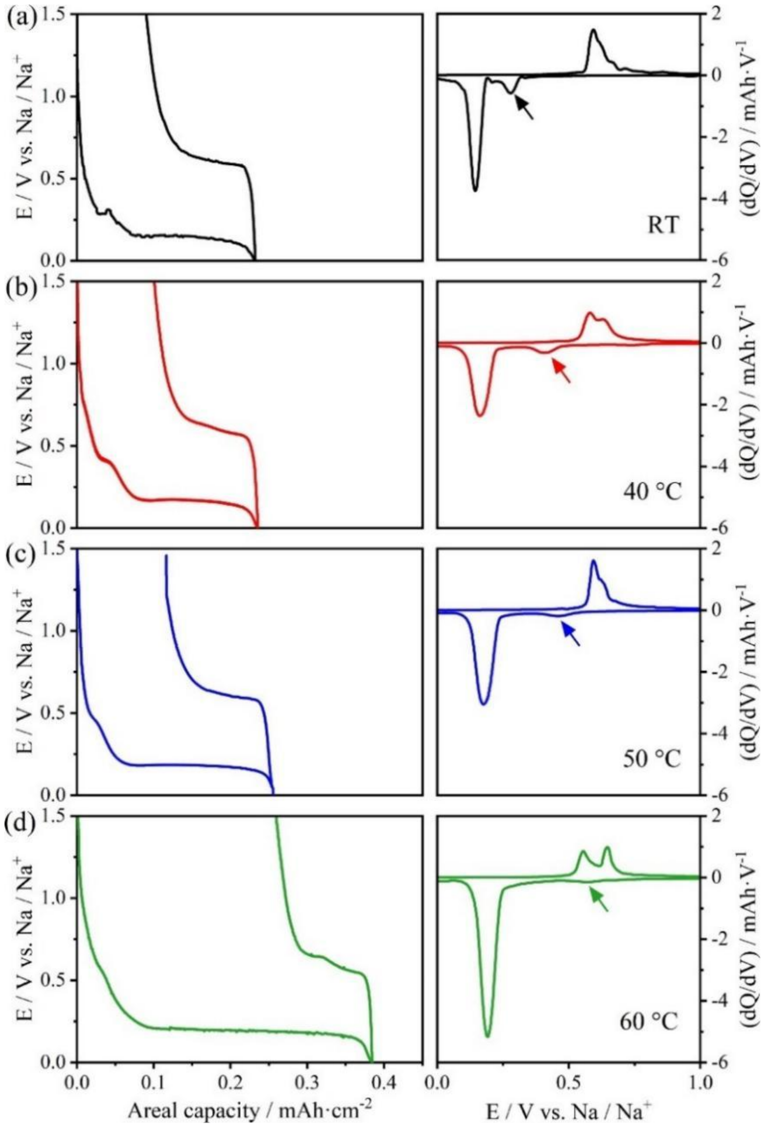

Figure 4.5 The potential vs areal capacity of Ge electrodes conducted at 1/100 C and its corresponding dQ/dV at various temperatures, (a) room temperature (RT), (b) 40 °C, (c) 50 °C, and (d) 60 °C.

4.2.2 Chronoamperometry of the Ge/$NaGe_4$ Transition

With convenience and adequate sensitivity in detecting the current response, chronoamperometry (CA) can be a suitable electrochemical technique to study the kinetics of electrochemical phase transition due to the constant driving force (i.e., a fixed overpotential). In the context here, we start with systematic tests on the first irreversible phase transition ($Na + Ge \rightarrow NaGe_4$), aimed at shedding light on the nature of initial nucleation and growth.

Figure 4.6 presents the current-time curves of Ge thin film electrodes under different applied potentials E_1 at various temperatures. It is found that regardless of the applied E_1 and temperature, all the current-time curves follow a typical trend: the currents drop abruptly once the overpotentials are applied, and then the decrease gradually slows down towards the end of sodiation. The two different stages for current variation in each curve are observed to be separated by a distinct kink (denoted by the arrow in

Figure 4.6a-d), which is likely a result of the phase propagation reaching the current collector [142]. Furthermore, at all chosen temperatures, the bigger the overpotential (E_0-E_1) is, the earlier the current kink appears and the bigger the current is. This trend may be explained by the faster phase transition rates under the higher overpotentials. Differently, as the temperature is elevated, the current magnitude obtained at the same E_1 seems to increase slightly, and the time reaching the kink seems to shorten. In addition, it should be noted that the kink disappears in the current-time curves in the second sodiation of the Ge that has undergone a GCD cycle (Figure 4.7), implying that the first phase transition is irreversible, which is in good agreement with the previously presented GCD analysis. Meanwhile, the current shows a monotonic decline as time goes by, indicating a single diffusion behavior. This simpler sodiation behavior in the second cycle (than the first cycle) was also observed in the lithiation of Si [142]. It is assumed that the formed Na-Ge phase (i.e., $NaGe_4$) in the first cycle can function as the new nucleation sites for the subsequent nucleation and growth processes so that the Na atoms can diffuse more readily into Ge without causing a significant structure change at the same applied E_1.

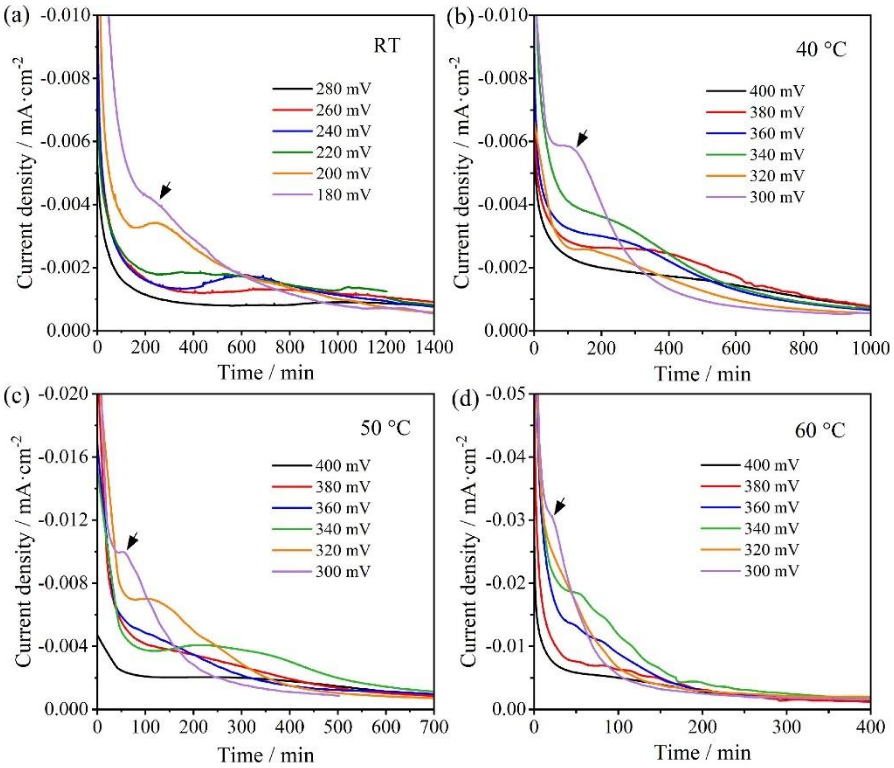

Figure 4.6 Current-time curves at different E_1 after the equilibrium at E_0 = 600 mV at various temperatures, (a) room temperature, (b) 40 °C, (c) 50 °C, and (d) 60 °C. Note that the kink is denoted by a short arrow.

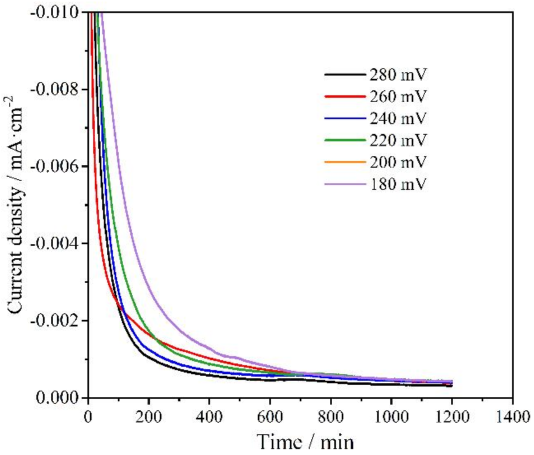

Figure 4.7 Current-time curves at different potential E_1 after equilibrium at E_0=600 mV in the second sodiation process. Note that all the cells undergo a sodiation/desodiation process at a constant current (1/20 C, i.e., 10 μA) prior to CA measurements.

4.2.3 Chronoamperometry of the $NaGe_4/Na_{1+x}Ge$ Transition

Kinetic analysis of the second phase transition (~0.12 V vs. Na/Na$^+$, $Na + NaGe_4 \rightarrow Na_{1+x}Ge$) is also done by using the CA technique. Figure 4.8 presents the current response as a function of time at different E_2 ranging from 110 mV to 10 mV (vs. Na/Na$^+$) at various temperatures. As can be seen, all current-time curves exhibit similar trends, of which, however, the shape is very different from the initial irreversible phase transformation presented before. Specifically, all the curves are characteristic of a single distinct peak, with the currents initially climbing to their maximum values, followed by gentler drops to nearly zero (i.e., end of sodiation). These features indicate that the nucleation and growth of new phases (generalized as $Na_{1+x}Ge$) likely govern the whole reversible phase transition [110]. Furthermore, as the applied potential E_2 moves from 110 mV to 10 mV (vs Na/Na$^+$), not only does the peak current increase evidently, but the duration to reach the peak current also shortens. This trend seems reasonable because a higher overpotential (i.e., a low potential vs. Na/Na$^+$ in this study) would certainly facilitate faster phase transformations. When the temperature rises from room temperature to 60 °C, one may see that the peak current seems to become bigger, and less time is required to reach the peak at higher temperatures, particularly at low E_2 (e.g., 10 mV, 30 mV, and 50 mV), indicating faster phase transformations.

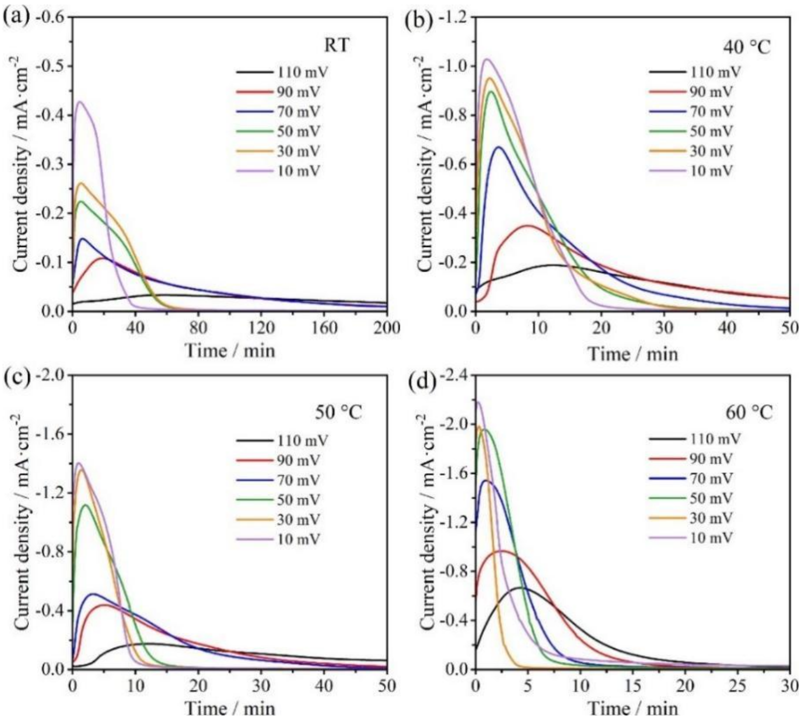

Figure 4.8 Current-time curves for the Ge electrode measured at different potentials E_2 (110-10 mV) after the 250 mV (E_0') holding at different temperatures, (a) room temperature, (b) 40 °C, (b) 50 °C, and (d) 60 °C.

4.3 Discussion

4.3.1 The Rate/Temperature-Dependent (De-)Sodiation of Ge

When revisiting the GCD profiles of the initial sodiation of Ge electrodes at 1/20 C and 1/100 C (Figure 4.1a-b), it may be noticed that the electrochemical behavior is clearly affected by the sodiation rate: Two distinct potential plateaus are observed at 1/100 C, of which the first one is absent at a higher rate of 1/20 C. On the basis of the phase diagram of Na-Ge [99], the electrochemical reactions involved in the sodiation of Ge are expected to be:

$$Na + Ge \rightarrow NaGe_4$$

$$Na + NaGe_4 \rightarrow Na_{1+x}Ge$$

At a relatively faster C-rate (i.e., 1/20 C in this work), due to a slower Na diffusion in the fresh Ge than in the sodiated $NaGe_4$, the propagation of the $NaGe_4$ phase (at the expense of Ge) front moves slower than that of the $Na_{1+x}Ge$ (at the expense of $NaGe_4$), resulting in simultaneous formation of both $NaGe_4$ and $Na_{1+x}Ge$. Electrochemically, this situation is revealed by single long plateaus during the initial sodiation process at 1/20 C (Figure 4.1a). In contrast, when the cycle rate slows down to an extremely low level (i.e., 1/100 C), there is enough time for the formation of $NaGe_4$ at a relatively higher potential (i.e., the first plateau at ~0.3 V vs Na/Na^+). In other words, the formation of the $NaGe_4$ and the $Na_{1+x}Ge$ occurs one after another, which thus gives two potential plateaus appearing in the initial sodiation of Ge electrodes at 1/100

C (Figure 4.1b). These processes will be schematically elaborated later in this work.

Moreover, it is found that the sodiation behavior of Ge is greatly influenced by temperature, as indicated by the smoother potential curves of the GCD profiles and lower overpotentials (i.e., higher plateau potentials) required for electrochemical reactions at elevated temperatures (Figure 4.5). At the temperature ≤ 50 °C, the GCD profiles exhibit similar features with similar capacities. By eliminating the capacity contribution from electrolyte breakdown, the obtained capacity of Ge corresponds to a Na insertion capacity of $Na_{1.38}Ge$ at room temperature, $Na_{1.41}Ge$ at 40 °C and $Na_{1.59}Ge$ at 50 °C, respectively. The Na/Ge atomic ratio is all higher than 1, but far away from 3. From the Na-Ge phase diagram, there is no other equilibrium phase between NaGe and Na_3Ge. Hence it is speculated that by the end of Ge sodiation at a temperature ≤ 50 °C, the NaGe phase predominates among the final sodiated products, perhaps with minor Na_3Ge existing. Intriguingly, when the temperature goes up to 60 °C, a dramatic capacity increase (~60%) is observed in the first sodiation of Ge (Figure 4.5d). The final sodiated products can be generalized as $Na_{2.3}Ge$ at 60 °C, which is a lot closer to the Na_3Ge stoichiometry. This electrochemical behavior at 60 °C suggests that a Na-rich phase (i.e., Na_3Ge) may be the primary product, agreeing with the two desodiation peaks (desodiation of both Na_3Ge and NaGe) observed in Figure 4.5d. Formation of higher-ordered phases is often observed for alloy anodes in Li-based systems at elevated temperatures, such as $Li_{22}Sn_5$ [144], and $Li_{2-x}Al$ [145]. However, due to the amorphous nature of both phases during sodiation, the formation of Na3Ge is not detected by XRD, hence, further investigations are required.

For desodiation at 60 °C, a significant capacity loss of ~70% is observed, significantly larger than those obtained at other temperatures below 60 °C (Figure 4.5d). This abrupt loss in reversible capacity is assumed to be partly affected by the material properties of Na_3Ge. On one hand, the irreversible capacity is likely associated with sodiation-induced volume change. Subhajit et al. reported that the amorphous Ge thin film undergoes ~240% volume change after the full sodiation, which corresponds to roughly $Na_{1.4}Ge$ [146]. Also, the amorphous Ge nanowires are observed to suffer from a ~300% volume expansion upon sodiation, in which the reaction terminates at $Na_{1.6}Ge$ [90]. Hence, it is anticipated that the formation of the Na_3Ge phase would induce a larger volume expansion (more Na is stored), thereby possibly more susceptible to mechanical failures [147]. It is known that huge compressive stresses can be generated in alloy anodes upon lithiation [148] and sodiation due to the volume expansion. Quantitatively, compressive stress of 0.56 GPa is observed when a Ge film is sodiated at room temperature, above which a higher compression is expected [146]. On the other hand, the electrical resistivities of Ge and its sodiated phases should also play a role. Although no direct evidence can be found on how Na inclusion affects the electrical conductivity of the sodiated Ge, the sodiated Sn (the element below Ge in the periodic table) is reported to be more electrically resistive as the Na content increases, not uncommon for intermetallic phases. The increase of this ohmic resistance can be drastic with values that are several orders of magnitude higher than pristine Sn

[149]. The poor electron transfer would slow down or even block the Na migration in the electrode during (de-)sodiation, thereby leading to large capacity losses (e.g., Na trapping). Back to Ge, it is also expected that the electrical resistivity of the sodiated Na_3Ge may be larger, which negatively affects the charge transfer and thus causes larger capacity loss. Additionally, an early study reported that the electrical resistivity of Ge in liquid Na is found to increase with temperature, but within a significantly higher range from 200 °C to 450 °C [150]. While no solid conclusion can be drawn on whether the electrical resistivity of our sodiated Ge is also higher at 60 °C than that at lower temperatures, it is not impossible that a slightly higher temperature may negatively affect the charge transfer of sodiated Ge to some extent, in our case, giving a poorer initial coulombic efficiency of the Ge electrode at 60 °C.

4.3.2 Nucleation and Growth Kinetics of $NaGe_4$

To quantify the nucleation and growth kinetics of the Ge/$NaGe_4$ phase transition, the current transients from the potentiostatic measurements are further analyzed using the KJMA model (details are provided in the supplementary data). Starting with room temperature, all the $\ln(\ln 1/(1-f))$ curves seem to show linear increases with the rising $\ln t$ with similar slopes (Figure 4.9a). The Avrami constants n at different voltage E_1, i.e., the slopes, are extracted and presented in Figure 4.9b. As shown, Avrami constants n obtained at room temperature are centered around 0.5, regardless of the applied potential. Based on $n = ab + c$, where a, b, and c represent the nucleation rate, the growth geometry, and the rate-limiting step, respectively, the obtained Avrami constants of nearly ~0.5 can be interpreted as: $a \approx 0$, $b = 1$, and $c = 0.5$. The $c = 0.5$ is one of the two well-characterized values, which is indicative of a diffusion-controlled process ($c = 1$ of the reaction-controlled process). This analysis implies that the Ge/$NaGe_4$ phase transformation at room temperature is characterized by a decreasing nucleation rate and a one-dimensional diffusion-controlled growth.

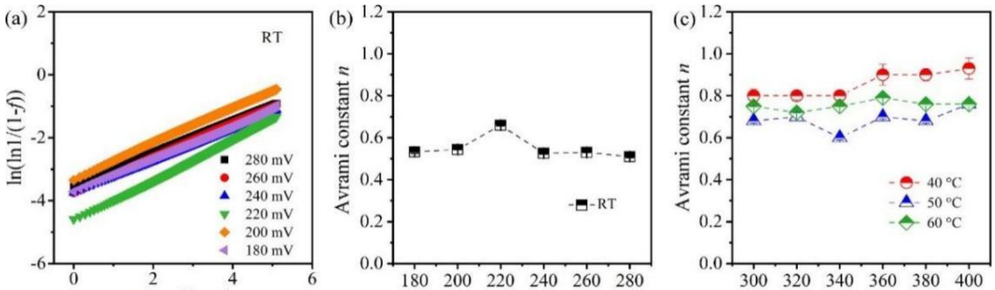

Figure 4.9 (a) Plots of the double logarithmic extent of new phase transformation (f) vs the logarithmic time for Ge electrodes after the potentiostatic holds at 280-180 mV at room temperature. (b) The Avrami constant n at different potential E_1 at room temperature. (c) The Avrami constant n as a function of the potentiostatic hold E_1 at elevated temperatures (i.e., 40 °C, 50 °C, 60 °C). The n values are determined from the slope of $\ln(\ln 1/(1-f))$ vs $\ln t$ (Figure 4.10c, 4.10f, 4.10i) for different potentiostatic tests at a fixed potential E_1 range of 300–400 mV based on the KJMA model.

Since the sodiation temperature does affect the formation of Na-Ge phases (as seen in Figure 4.5), we decided to repeat the same analyses at elevated temperatures, i.e., 40 °C, 50 °C, and 60 °C (Figure 4.10). One may see from Figure 4.9c that the Avrami constants at elevated temperatures all become slightly larger than those obtained at room temperature, laying somewhere between 0.6 and 1. The larger Avrami constants at higher temperatures likely resulted from higher nucleation rates as well as faster ion diffusion, while the growth geometry is unlikely affected. Nevertheless, the slow diffusion in Ge for the formation of the $NaGe_4$ phase is still the rate-limiting factor, even when the temperature is increased up to 60 °C.

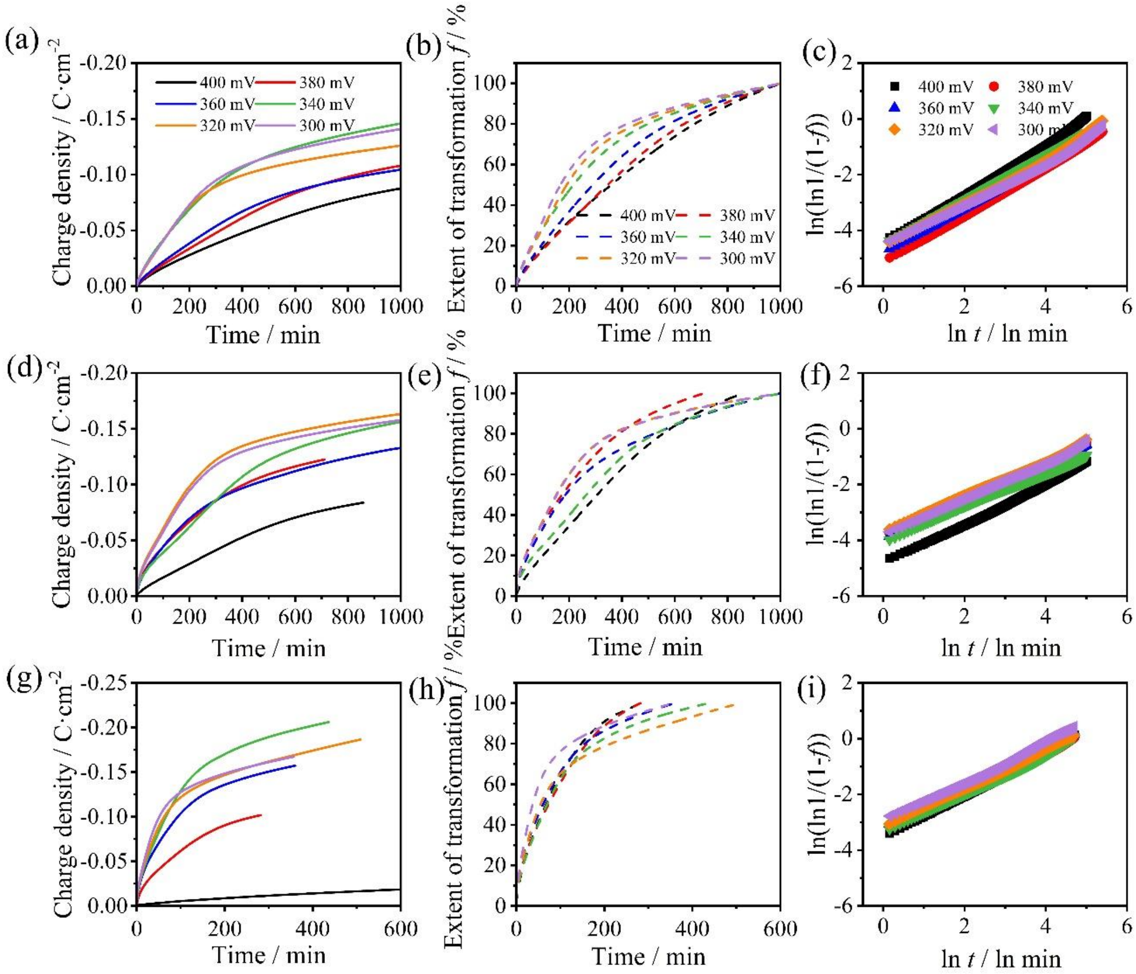

Figure 4.10 Plots of charge density versus time for Ge electrode obtained at different potential E_1 at (a) 40 °C, (d) 50 °C, and (g) 60 °C. The extent of the transformation to $NaGe_4$ phase (*f*) as a function of time at the same potential E_1 range of 400-300 mV at (b) 40 °C, (e) 50 °C, and (h) 60 °C. The ln(ln1/(1-*f*)) versus ln *t* plots for Ge electrodes at different E_1 at (c) 40 °C, (f) 50 °C and (i) 60 °C.

To further explore the temperature dependence, the Arrhenius equation is employed to shed light on the sodiation rates under different applied potentials. With the well-established Avrami plots, the natural logarithm of the rate constants (*k*) under different experimental conditions can be extracted from the intercept of ln(ln1/(1-*f*)) vs ln *t* plots at the *y*-axis (Figures 4.10c, 4.10f, 4.10i), which are then plotted against the inverse of the temperatures (Figure 4.11a). Based on the slopes extracted from the linear fittings, the activation energy (E_a) in all cases is calculated and summarized in Figure 4.11b, in which values of ca. 50 kJ·mol^{-1} are obtained (although perhaps due to some unexpected experimental errors, two datasets that do not show a typical Arrhenius-type temperature dependence (hollow dots in Figure 4.11b), which may or may not warrant further investigation).

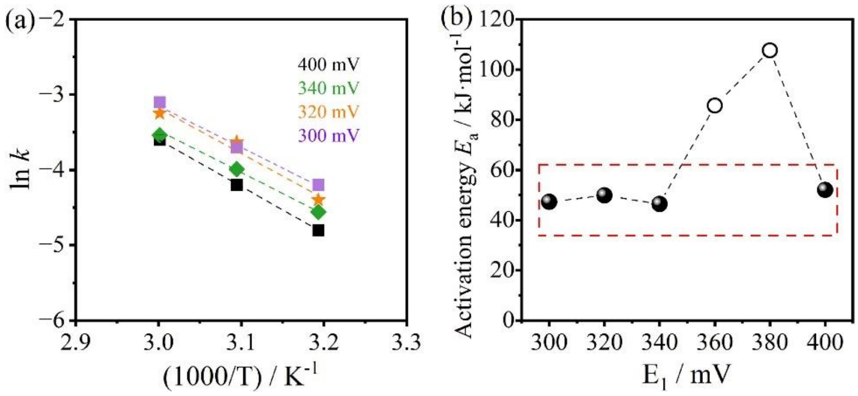

Figure 4.11 (a) Temperature dependence of the rate constant of Ge electrodes under different potentiostatic holds (E_1). (b) The calculated activation energies of the Ge/$NaGe_4$ phase boundary movement by Arrhenius equation at different potentiostatic holds (E_1). Since plots of ln k vs 1000/T obtained at 380 mV and 360 mV are far away from the linearity, these two plots are excluded in Figure 4.11a. Hence the calculated activation energy under potentiostatic hold at 360 and 380 mV is probably not reliable and denoted as hollow dot in Figure 4.11b.

While the obtained E_a represents the minimum energy required for the Ge to $NaGe_4$ phase transition to occur, the Ea for Na diffusion should be larger than this value (i.e., ~50 kJ·mol^{-1}) since this phase transition is characterized to be a diffusion-controlled process by the Avrami analysis. Therefore, we first try to extract the diffusivities using the Cottrell equation (derived from Fick's law of diffusion), which is noted for analyzing diffusion-limited electrochemical reactions in planar electrodes, just like in other studies of alloy anodes [142, 151]. Figure 4.12a shows the current densities as a function of the inverse square root of time measured at different E_1 (280-180 mV) at room temperature, i.e., following the Cottrell equation. One may see that the current (post-kink; single phase region) measured under different potential steps exhibits a strong linear relation with $t^{-1/2}$, with the diffusivities of Na in $NaGe_4$ estimated from the slopes at applied E_1 range of 280-180 mV (Figure 4.12b). It is found that the values of D_{Na} in $NaGe_4$ are in an order of 10^{-12} cm^2·s^{-1}, which is further examined and supported by calculating the D_{Na} using data of the second sodiation (Figure 4.13). The seemly gradual increase trend of D_{Na} as a function of overpotentials observed in Figure 4.12b is assumed to be associated with the reduced diffusion barrier of Na at lower E_1 [142]. The higher overpotentials result in a more pronounced Na concentration difference between the electrode/electrolyte interface and the electrode/Cu foil interface, which drives more Na atoms into the Ge matrix. Upon the sodiation, the amorphous Ge matrix is predicted to be softer since more Na insertion into Ge during the sodiation will induce the formation of weaker ionic bonding (i.e., Na-Ge bond) at the expense of rigid covalent bonding (i.e., Ge-Ge bond) [105]. Therefore, at lower applied E_1, Na atoms could diffuse more easily by jumping via interstitial sites in the softener amorphous $NaGe_4$ structure [142].

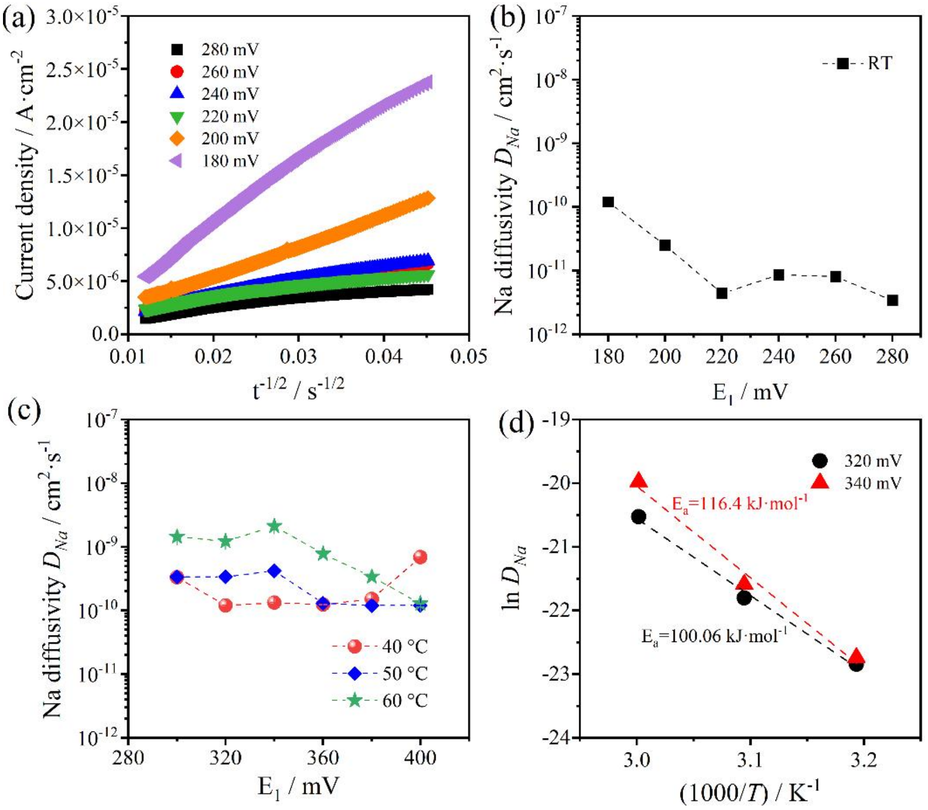

Figure 4.12 (a) The plot of current density vs inverse square root of time for Ge electrodes under different potentiostatic holds (E_1) at room temperature. (b) The diffusivity of Na in $NaGe_4$ as a function of E_1 at room temperature. Note that the diffusivity values are derived from the slope of current density vs. $t^{-1/2}$ (Figure 4.12a). (c) The comparison of Na diffusivities in $NaGe_4$ at elevated temperatures. (d) The temperature dependence of logarithmic Na diffusivity (ln D_{Na}) at E_1 = 320 mV and 340 mV.

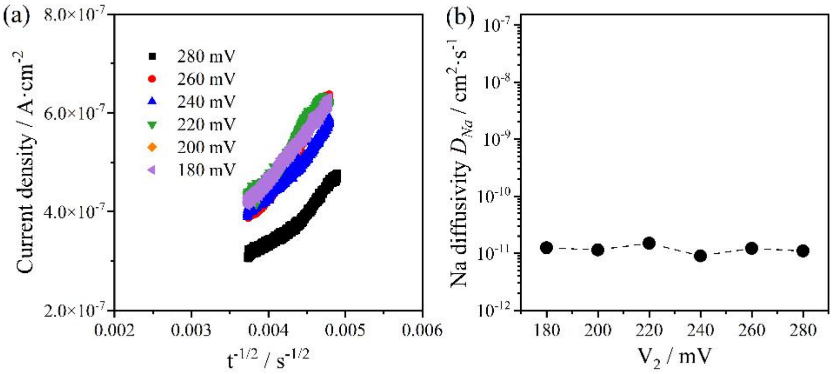

Figure 4.13 (a) The change of current density as a function of the inverse square root of time for Ge electrodes measured in a potential E_1 range of 280-180 mV in the second sodiation at room temperature. (b) The derived Na diffusivity in $NaGe_4$ in the second sodiation process. Note that the Ge electrodes undergo a galvanostatic charge/discharge process at a constant current (1/20 C, i.e., 10 µA) prior to potentiostatic measurements.

Given that the Ge/NaGe$_4$ phase transition is governed by Na diffusion in Ge, the maximum C-rate can be roughly estimated by the time for Na diffusion through the Ge electrode: $3600\, D_{Na} / l^2$ [152], where l denotes the electrode thickness (ca. 850 nm). Herein, although the Na diffusivity in amorphous Ge is not extracted directly, its value should be less than the obtained Na diffusivity in NaGe$_4$: ~10^{-12} cm^2·s^{-1}. In this case, the maximum C-rate for the transition to NaGe$_4$ is approximately less than 0.05 C at room temperature. Namely, the C-rate that the formation of NaGe$_4$ and Na$_{1+x}$Ge occurring one after another should be below 0.05 C. Otherwise, the phases NaGe$_4$ and Na$_{1+x}$Ge are forming simultaneously at a charging C-rate larger than 0.05 C at ambient temperature.

Similar potential-dependent D_{Na} (in NaGe$_4$) are also provided in the plot of D_{Na} vs. E$_1$ at 40 °C, 50 °C and 60 °C (Figure 4.12c), in which the D_{Na} values are derived from the Cottrell fittings at these temperatures in Figure 4.14. Despite smaller variations of D_{Na} with potential at elevated temperatures, the Na diffusion in NaGe$_4$ is found to be faster due to the improved kinetics at higher temperatures. Specifically, the average value of Na diffusivity at 60 °C is ~5.9×10^{-10} cm^2·s^{-1} while the D_{Na} values at 50 °C and 40 °C are roughly 1.2×10^{-10} and 1.5×10^{-10} cm^2·s^{-1}. To evaluate the activation energy required for the Na diffusion in NaGe$_4$, we tentatively plotted the diffusivity values vs. 1000/T at the potential E$_1$ = 340 and 320 mV, as shown in Figure 4.12d. It is observed that the diffusivity exhibits a linear relation assumed by the Arrhenius equation $D = D_0 \exp(-E / kT)$, from which the activation energy is extracted to be ~110 kJ·mol^{-1}. One may notice that the calculated E_a for Na migration in NaGe$_4$ is higher than the E_a for the Ge/NaG$_4$ phase boundary movement. This observation is further consistent with the finding that the Na diffusion is the rate-limiting step during this phase transformation, as it agrees well with the Avrami analysis presented above.

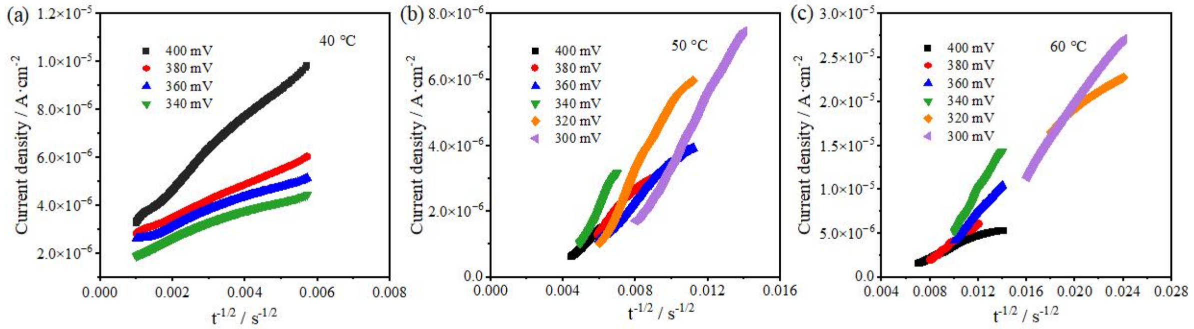

Figure 4.14 Plots of current density versus the square root of time for the Ge electrodes obtained in the same potential E$_1$ range of 400-300 mV at elevated temperatures, (a) 40 °C, (b) 50 °C, (c) 60 °C.

4.3.3 Nucleation and Growth Kinetics of Na$_{1+x}$Ge

Following the KJMA model, the potentiostatic results were further analyzed to shed light on the nucleation and growth mechanism of the Na$_{1+x}$Ge phase. Figure 4.15a shows the relationship between the extent of transformation (f) and time (t) in a fixed potential range of 110-10 mV, from which the Avrami constant n is extracted and presented in Figure 4.15b. The obtained Avrami constants are all centred around 1.2 with small variations under different applied potentials. Two possible interpretations are expected: first, one-dimensional phase growth with a decreasing nucleation rate ($0 < a < 1$, $b = 1$, $c = 1$); second, two-dimensional diffusion-controlled growth with a decreasing nucleation rate ($0 < a < 1$, $b = 2$, $c = 0.5$). It was reported that in the diffusion-controlled phase reaction, the current density decreases with the increase of time while in the phase boundary movement-controlled phase reaction the current density is independent of the time [142]. Given the characteristic of current-time curves in Figure 4.8, the first interpretation for the Avrami constant n ($0 < a < 1$, $b = 1$, $c = 1$) should be more plausible: the further sodiation of $NaGe_4$ to $Na_{1+x}Ge$ probably occurs through decreasing nucleation and a one-dimensional (1*D*) phase boundary movement-controlled growth model.

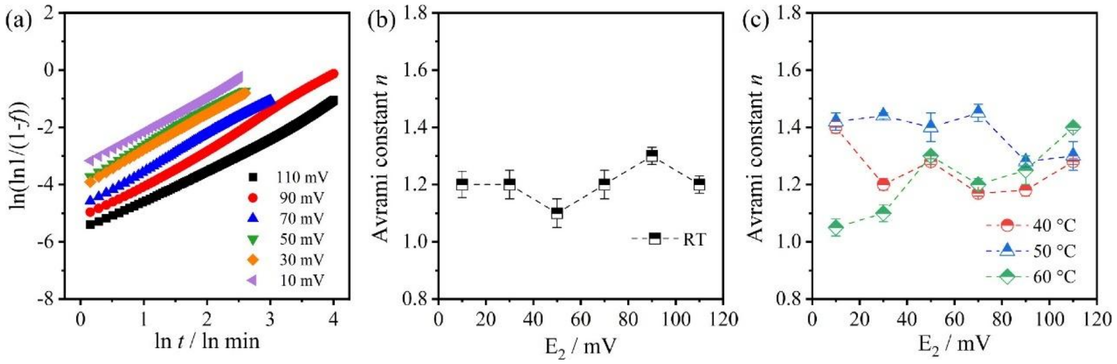

Figure 4.15 (a) Plots of ln(ln1/(1-*f*)) vs. ln *t* after different potentiostatic hold (E_2) at room temperature. (b) The Avrami constant n as a function of E_2 at room temperature. The value of n is obtained from the slope of the ln(ln1/(1-*f*)) vs ln *t* plots (Figure 4.15a) based on the KJMA model. (c) Comparison of the Avrami constant n obtained in a fixed potential E_2 range of 110-10 mV at different temperatures.

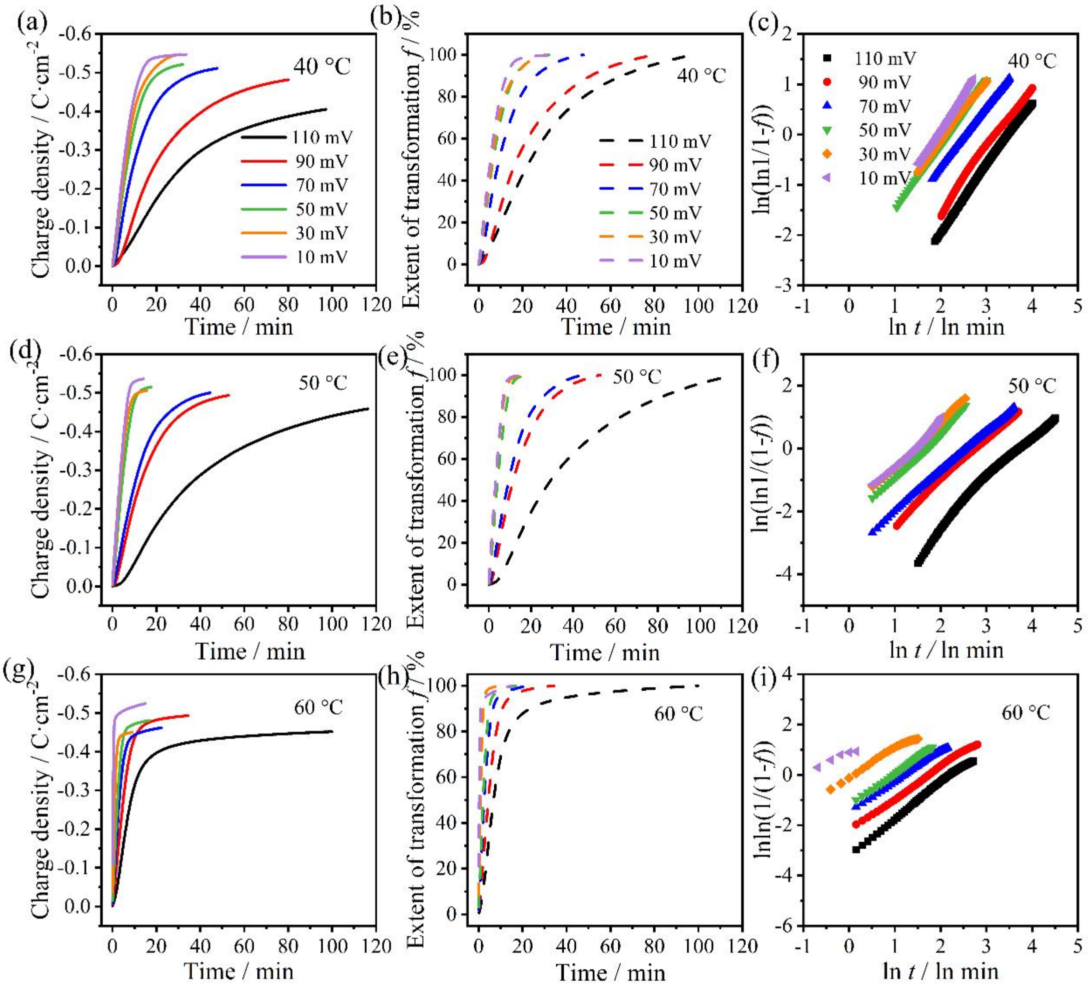

Figure 4.16 The time-dependent charge density for Ge electrode obtained at different potential E_2 at (a) 40 °C, (c), (d) 50 °C and (g) 60 °C. Plots of the transformation to $NaGe_4$ phase (f) versus time at the fixed potential E_2 range of 110-10 mV at (b) 40 °C, (e) 50 °C and (h) 60 °C. The change of ln(ln1/(1-f)) as a function of ln t for Ge electrodes obtained at different E_2 at (c) 40 °C, (f) 50 °C, and (i) 60 °C.

Figure 4.15c compares the Avrami constants n in the same voltage range of 110–10 mV at different temperatures. The Avrami constants at 40 °C, 50 °C, and 60 °C are extracted from Figure 4.16. It is found that the Avrami constants at elevated temperatures all fall into the range of 1.0-1.5, regardless of the potential E_2, which are in well consistency with the Avrami constants at room temperature. These results again suggests the $NaGe_4$/$Na_{1+x}Ge$ phase transformation occurs with 1D phase boundary movement-controlled growth and a decreasing nucleation rate within the chosen temperature range.

The rate constant k of the $NaGe_4$/$Na_{1+x}Ge$ phase boundary movement can be extracted from the intercept of the ln(ln1/(1-f)) vs. ln t plots for the data obtained at room and elevated temperatures (Figure 4.15a and Figure 4.16). Figure 4.17a shows the Arrhenius fittings of the phase transition from $NaGe_4$ to $Na_{1+x}Ge$ at the applied voltage E_2 range of 110-10 mV. As expected, the logarithmic rate constant ln k increases as the temperature rises to 60 °C, following an ideal Arrhenius-type temperature dependence. Also, taking a close look at the rate constant at the same temperature, the value of ln k tends to go up with the decrease of potential E_2, although not obvious. This trend might be the result of the higher overpotential, which accelerates the phase boundary movements and thereby leads to the increased rate constant. Figure 4.17b shows the activation energy (E_a) for the $NaGe_4/Na_{1+x}Ge$ phase transformation estimated from the slope of rate constant against temperature plots (Figure 4.17a) at different potential E_2. It should be noted that the datasets at 110 mV and 10 mV, which do not show a typical Arrhenius-type temperature dependence (hollow dots in Figure 4.17b), are excluded. One can see that the activation energy of the $NaGe_4/Na_{1+x}Ge$ phase boundary movement varies between ~60 and ~80 kJ·mol^{-1} with the decreasing potential E_2, higher than the activation energy required for the Ge/$NaGe_4$ phase transition.

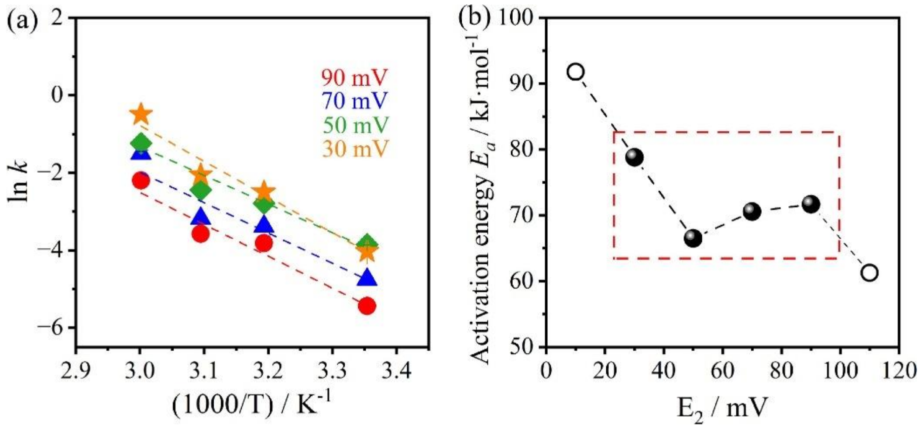

Figure 4.17 (a) Temperature dependence of the rate constant k at different potential E_2. Note that the k values under different conditions are obtained from the intercept of plots of ln(ln1/(1-f)) vs ln t at the y-axis (Figure 4.15a and Figure 4.16c, 4.16f, 4.16i) based on KJMA theory. (b) The calculated activation energies (E_a) for the $NaGe_4/Na_{1+x}Ge$ phase boundary movement as a function of the applied potential E_2.

4.3.4 The Schematic Models for the Sodiation of Ge

Based on the discussion on the nucleation and growth kinetics, we propose two possible schematic models to illustrate how Ge is sodiated electrochemically (Schematic 4.1) considering the sodiation temperatures and rates.

Scenario 4.1 illustrates how the Ge electrode is sodiated to $Na_{1+x}Ge$ at an extremely low C-rate (i.e., 1/100 C) through two steps. In the case of the Ge/$NaGe_4$ phase transformation, the presence of the kinks in current-time curves during the initial sodiation (Figure 4.6) suggests that a significant structural transition occurs through a sharp phase interface (i.e., Ge/$NaGe_4$) propagation (likely the phase boundary hitting the current collector). After the first potential hold at E_0, the Ge electrode forms a saturated solid solution without a phase transition at the given potential (Schematic 4.1a) [153, 154], while additional Na ions accumulate at the electrode/electrolyte interface and will start inserting into Ge when the potential jumps to E_1. At this stage, the new phase $NaGe_4$ nucleates and grows to form a layer on the top of the Ge electrode (blue rectangular region at stage ① in Schematic 4.1a) since it is limited by the slow diffusion (Avrami analysis). Consequently, there should exist a Na concentration gradient in the $NaGe_4$ single phase (stage ② in Schematic 4.1a) at the exact point when the Ge is completely transformed into $NaGe_4$, i.e., the Ge/$NaGe_4$ interface hits the current collector, leading to the kink in current-time curves (Figure 4.6). Afterward, Na continues diffusing from the electrode/electrolyte interface to the electrode/current collector interface to form a homogeneous $NaGe_4$ layer after a certain period of time. This process (stage ② in Schematic 4.1a) does not involve any phase transitions and is considered a simple diffusion process, consistent with the Cottrell equation.

As for the phase transformation from $NaGe_4$ to $Na_{1+x}Ge$, a generalized 1*D* nucleation-growth model is proposed here to interpret the continuing sodiation of $NaGe_4$. In Schematic 1b, an initial potential control at E_0' = 250 mV is used to guarantee a complete formation of $NaGe_4$ (the blue rectangular region in Schematic 4.1b). When the potential further drops to E_2 (110-10 mV), excess Na atoms accumulated on the electrolyte/electrode interface will start migrating into $NaGe_4$, where the nucleation of $Na_{1+x}Ge$ at the expense of $NaGe_4$ is expected. As time goes on, the $Na_{1+x}Ge$ phase grows through the $NaGe_4$/$Na_{1+x}Ge$ interface moving across the thickness of thin film towards the current collector (1*D* growth). Noteworthy, since this phase transition is a reaction-controlled process (Avrami analysis), i.e., the diffusion of Na in $NaGe_4$ is faster than in Ge, the Na incorporation into Ge during this process will result in a more homogeneous distribution of Na in $Na_{1+x}Ge$ layer (dark blue rectangular region in Schematic 4.1b).

At a higher rate (i.e., 1/20 C, Scenario 2), differently, the two processes discussed above likely occur simultaneously. To be specific, when the current is applied, a great number of Na will accumulate on the surface of the Ge electrode, with minor Na diffusing into the Ge bulk to form the Na-Ge solid solution. Once the overpotential is sufficient, $NaGe_4$ will be nucleated on the electrode surface and subsequently grow to form a $NaGe_4$ layer (stage ① Schematic 4.1c). While an extra slow phase boundary movement is expected for the Ge/$NaGe_4$ interface due to the sluggish Na diffusion in Ge, Na can diffuse quite fast in the newly formed $NaGe_4$ layer, in which the $Na_{1+x}Ge$ phase can be nucleated (stage ② Schematic 4.1c). As a result, both the $NaGe_4$ and the $Na_{1+x}Ge$ are forming simultaneously following a 1*D* propagation model until the end of sodiation (stage ③ Schematic 4.1c). In short, the whole sodiation process at the higher rates seems to be controlled by the phase boundary movement of the Ge/$NaGe_4$.

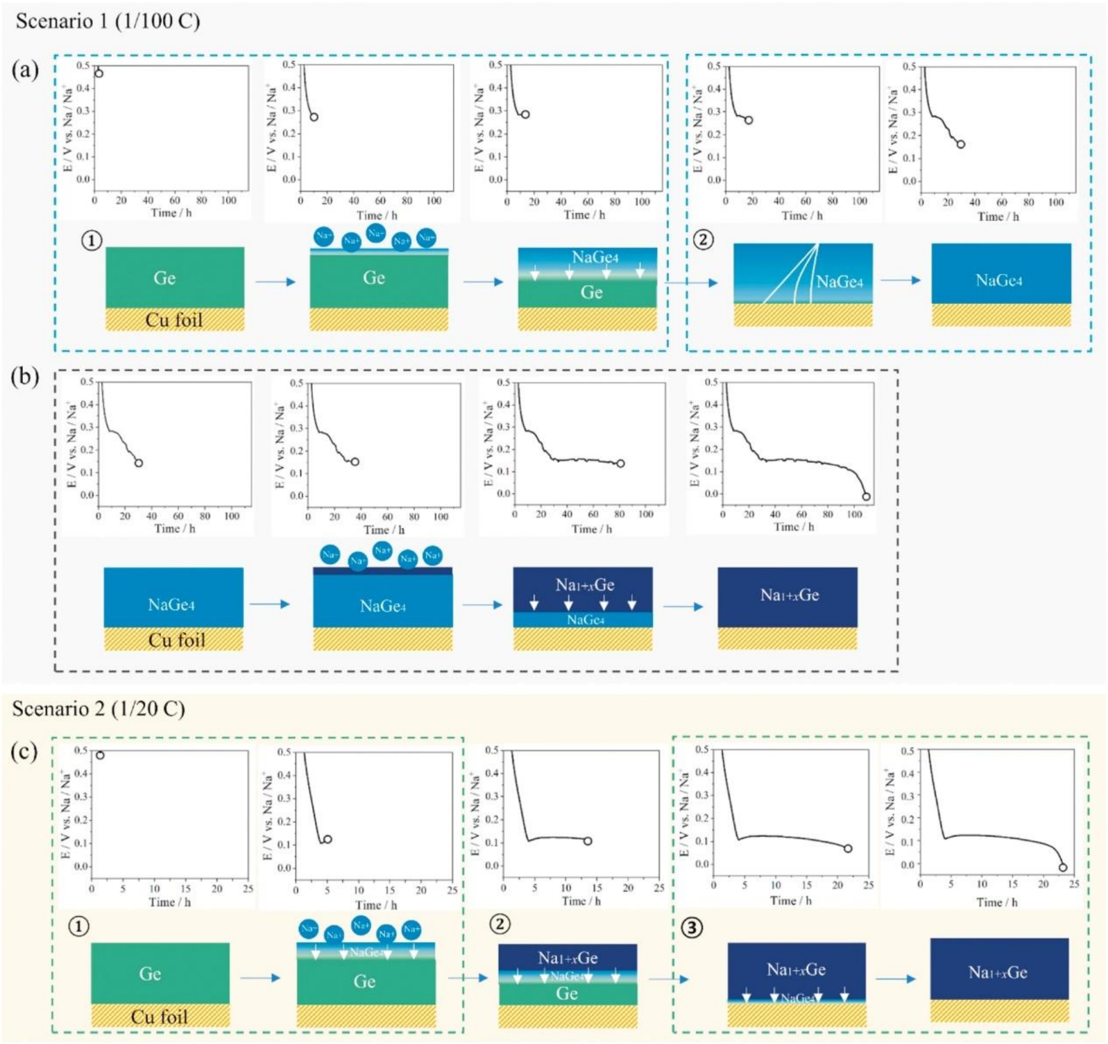

Schematic 4.1 Proposed schematics of initial sodiation of Ge at two C-rates. Scenario 1 depicts how Ge is sodiated at 1/100 C, where (a) shows the interface propagation model for Ge/$NaGe_4$ phase transition while (b) shows the nucleation-growth model for $NaGe_4$/$Na_{1+x}Ge$ phase transition. Scenario 2 illustrates how Na is stored in Ge at 1/20 C. Note that the schematic here focuses on the cross-section view of the electrode, and the white arrows indicate the two-phase interface propagation.

4.4 Conclusion

In this work, the electrochemical sodiation of Ge is investigated by robust electrochemical methods. Ge, located below Si in group IVA, can readily react with Na electrochemically in its amorphous state, delivering a reversible capacity of ~400 mAh·g^{-1} at 1/20 C. The galvanostatic measurement also shows that the Ge electrode undergoes an irreversible structural transition in the initial sodiation, but in the subsequent cycles, the transition is highly reversible. Meanwhile, the generalized sodiation behavior of Ge is found to be kinetically limited by the sodiation temperatures and C-rates. Furthermore, the mechanisms and kinetics of the phase transitions that occurred during the initial sodiation of Ge are systematically investigated using chronoamperometry techniques. A quantitative analysis further shows that both the Ge/$NaGe_4$ and the $NaGe_4/Na_{1+x}Ge$ phase transitions proceed through 1*D* growth, but the rate-limiting step for the former is the diffusion of Na in Ge while the latter is limited by the reaction at $NaGe_4/Na_{1+x}Ge$ interface. These nucleation and growth mechanisms are found to be independent of temperature and applied potential steps within the selected ranges. The diffusivity of Na in $NaGe_4$ is also determined using the Cottrell equation to be in the order of 10^{-12} $cm^2 \cdot s^{-1}$ at room temperature, in contrast to a higher D_{Na} value of ~10^{-10} $cm^2 \cdot s^{-1}$ at 60 °C. By correlating the rate constant with the sodiation temperature, the activation energy required for the phase transition of $Ge/NaGe_4$ and $NaGe_4/Na_{1+x}Ge$ is estimated to be about 50 $kJ \cdot mol^{-1}$ and 70 $kJ \cdot mol^{-1}$, respectively. Lastly, schematic models are proposed and examined to illustrate the sodiation mechanisms of Ge electrodes under a fast and a slow discharge condition. These findings may lay fundamental groundwork for the future development of a Ge-based anode for sodium-ion batteries, and more broadly, such knowledge also offers an implication for the exploration of alloy-type SIB anodes.

Chapter 5: Sodiation kinetics of Sn

5.1 Introduction

Sn is a competitive anode candidate for sodium-ion batteries since it is abundant, cheap, highly conductive, and can electrochemically alloy with sodium to form a $Na_{3.75}Sn$ phase, giving a high specific (847 $mAh\cdot g^{-1}$) and volumetric (~1200 $mAh\cdot cm^{-3}$) capacity [96]. However, Sn electrodes show fast capacity degradation and low coulombic efficiency, which largely hinders commercialization. In general, the poor cycling performance is assumed to be due to significant volume change (~420%) of Sn electrodes during the (de-)sodiation process [155, 156]. This volume change will induce mechanical damage to the electrode (e.g., cracks and pulverization), and cause the loss of electrical contact between the electrode and current collector. Meanwhile, more SEI layers will grow on the newly bared surface of the electrode during the cycling, which will cause the increased consumption of active sodium and finally result in battery failure by depleting the available Na [155]. However, it is worth mentioning that the mechanical failure and SEI continuous growth could not be the only origin of the poor cycling performance of Sn. As the battery's electrochemical performance is essentially dependent on the capability of charge or ions transported from one electrode to another one, the charge transfer or diffusion kinetics should play a critical role in determining the electrochemical performance. Particularly, several recent works have found that the low coulombic efficiency of Sn composite electrodes is probably associated with the dramatically increased electrical resistivity of the NaSn intermediate phase compared to the Sn [102, 149, 157], and revealed that the sluggish charge transfer might be the origin of the kinetic loss that partly causes poor electrochemical performance. Therefore, for Sn electrode a comprehensive understanding of charge transfer or Na diffusion kinetics in the (de-)sodiation is essential to the improvement of electrochemical performance. But to our knowledge, there is a lack of research work revealing the charge/ion transport kinetics in Sn electrodes at present.

Herein, we systematically explore the electrochemical kinetics (e.g., ion diffusion and charge transfer) of Sn electrodes in the (de-)sodiation. Sn foil is used for this study because foil architecture simplifies the research system and avoids the influence of binders or additives in the composite electrode. Over the years, several electrochemical techniques such as galvanostatic intermittent titration technique (GITT), potentiostatic intermittent titration technique (PITT), and electrochemical impedance spectroscopy (EIS), based on the assumption of Fick's laws, have been developed to reveal the ion transport kinetics in electrode materials. The accurate estimation of ion diffusivity can be obtained in the single-phase region using these methods, but they have a limitation in the two-phase region involving phase transformations [104]. Zhu et al developed a new method combining the phase transformation theory and conventional GITT/PITT, which allows us to accurately determine the true diffusivity in individual phases in the two-phase region [158]. Nevertheless, here it is very difficult to employ the method developed by Zhu et al. to extract the diffusivity in individual Na_xSn phases (e.g., NaSn, Na_9Sn_4, $Na_{15}Sn_4$) because its calculation relies on the concentration/composition versus equilibrium potential profiles in each single-phase region, and the sodium-tin phase diagram indicates no single-phase region in the whole composition range. Therefore, in this work, we also employ the traditional technique to explore the apparent chemical diffusivity of sodium in Na_xSn ($0<x<3.75$). Among these techniques, the EIS technique can reveal both the charge transfer and ion diffusion kinetics of electrodes and is thus used here for the kinetic study of Sn electrodes. It should be noted that the obtained diffusivity here is indicative of the apparent Na diffusivity in mixed phases (i.e, Sn and Na_xSn phases), rather than the actual diffusivity in a single NaSn (or Na_9Sn_4, $Na_{15}Sn_4$) phase.

5.2 Results

5.2.1 Electrochemical (De-)Sodiation of Sn Foil Electrodes

Figure 5.1a shows the initial sodiation (discharge)-desodiation (charge) curve of Sn foil electrodes cycled between 0.001-1 V vs. Na/Na^+ at 0.2 mA (~C/100) at ambient temperature (20 °C). For the sodiation, the electrode sequentially undergoes three distinctive voltage plateaus at around 0. 13 V, 0.08 V, and 0.02 V vs. Na/Na^+ respectively, delivering a capacity of ~685 $mAh \cdot g^{-1}$ (~15.4 $mAh \cdot cm^{-2}$), smaller than the theoretical capacity 847 $mAh \cdot g^{-1}$ (assuming the formation of $Na_{15}Sn_4$). The kinetic limitation is probably responsible for the smaller capacity of the Sn electrode even at the extremely low C-rate. A close examination shows that these sodiation plateaus slightly fluctuate, which is also related to the kinetic limitation. In the subsequent desodiation, three desodiation plateaus are observed at ~0.2 V, 0.55 V, and 0.62 V, although the last two plateaus are not evident. Noteworthy, the desodiation profiles become very noisy after the first desodiation plateau at ~0.2 V. This phenomenon is also observed in the Sn thin film electrode [159], which is assumed to be associated with the loss of electrical contact due to the electrode structural damage (e.g., pulverization) caused by significant volume change. After the full desodiation to 1 V vs. Na/Na^+, a capacity of ~600 $mAh \cdot g^{-1}$ is obtained.

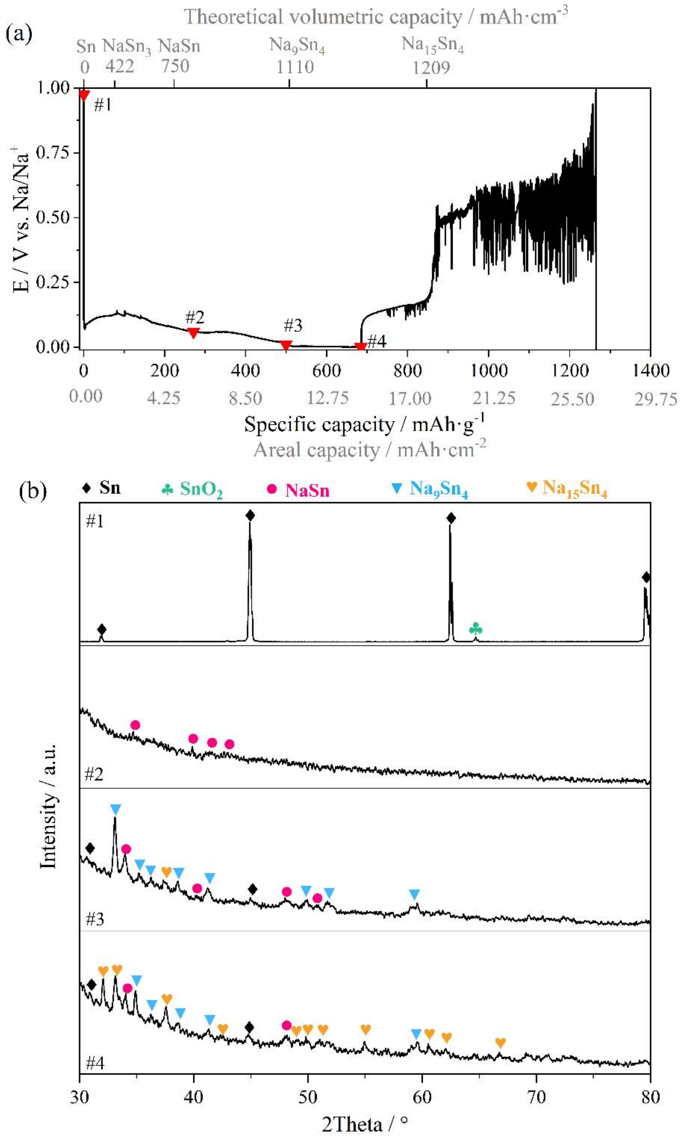

Figure 5.1 (a) The galvanostatic charge-discharge profiles of the Sn electrode cycled at 0.01 C, and (b) The X-ray diffractograms of the Sn electrode before cycling (#1) and at different states of sodiation (i.e., sodiation to 0.1 V (#2), 0.03 V(#3), and 0.001 V(#4)) in cycle 1, which are marked in Figure 5.1a.

To understand what Na-Sn intermetallic phases are formed in the sodiation, we employ the ex-situ XRD technique to characterize the phase composition of Sn electrodes at different depths of sodiation (i.e., DoD). Figure 5.1b shows the XRD diffractograms of the Sn electrode before cycling and after sodiation to 0.1 V, 0.03 V, and 0.001 V (vs. Na/Na$^+$) respectively. The main diffraction peaks in the XRD diffractogram of the pristine Sn foil (#1 in Figure 5.1b) are found to be well consistent with the characteristic peaks of the reference tetragonal Sn phase (PDF #99-0003721). Additionally, a small peak at around 64° matches with the SnO_2 phase (PDF #98-000-0151). At the sodiation to 0.1 V vs. Na/Na$^+$ (~5.5 mAh·cm^{-2}, the end of the first sodiation plateau), no significant diffraction peaks are observed in the diffractogram of the electrode, except for several weak and broad peaks which agree with those of the NaSn phase in PDF card #01-083-1231 (#2 in Figure 5.1b). This suggests the mostly amorphous or nano-crystalline nature of the sodiated phases, or that the phase is not detected due to the limitation of XRD measurement configuration. For the electrode sodiated to 0.03 V vs. Na/Na^+ (the end of the second sodiation plateau), new peaks at around 33.8°, 35°, 42°, 59°, etc that are assigned to the Na_9Sn_4 phase (PDF #01-071-9878) appears, accompanied with the emergence of a small diffraction peak at 37.5° corresponding to $Na_{15}Sn_4$ phase (PDF #01-071-9879) (#3 in Figure 5.1b). Moreover, some peaks that are in agreement with that of the Sn phase, e.g., at ~23°, and NaSn phase, e.g., 34° are also observed. After the full sodiation to 0.001 V vs. Na/Na^+ (the end of the third sodiation plateau), peak at around 34° and 50° that agree with the $Na_{15}Sn_4$ phase appear. Meanwhile, a peak at 33° corresponding to the Na_9Sn_4 phase disappears (#4 in Figure 5.1b). Interestingly, the peak related to the Sn phase is still visible and some peaks corresponding to NaSn and Na_9Sn_4 phases are also detected. These XRD results indicate that the sodiation of Sn foil follows the process $Sn \rightarrow {}_{(amourphous)}NaSn \rightarrow Na_9Sn_4 \rightarrow Na_{15}Sn_4$, which is basically consistent with the previously reported literature [93]. But these phase transformations probably occur simultaneously, given the coexistence of these Na-Sn intermetallic phases.

5.2.2 Morphology Characterization of Sn Foil Electrodes

Macro-scale photography and scanning electron microscopy (SEM) techniques are also employed to explore the photographic and morphological variation of Sn electrodes during the initial (de-)sodiation process. Figure 5.2 shows the top-view photographic and SEM image of the Sn foil electrode before cycling, where the calendaring trace is evident on the electrode surface. Figure 5.3a shows the surface photographic images of the electrode at different depths of discharge (DoD). Upon the 5% sodiation, the surface of the electrode is largely covered by a black-gray layer while the disk shape and sizes do not change. As the sodiation depth increases (particularly after 40% DoD), the electrode surface features undulations, despite the non-uniform color of the electrode. This is assumed to be likely related to the inhomogeneous sodiation-induced stress, which causes the mechanical deformation of the electrode. Besides, some small fragmental debris is also observed on the edge of the electrode after the sodiation beyond 60%. SEM observation (Figure 5.3b) shows that at DoD ≤ 20% the electrode surface looks dense and smooth, and maintains the calendaring trace of the pristine Sn foil (Figure 5.2). For the case of DoD 40%, and 60%, the electrode displays a mossy surface morphology, with many small voids on the electrode surface, and some cracks are also found in the chosen area. As the sodiation depth increases to and beyond 80%, the electrode becomes more catastrophic: larger voids are formed, accompanied by some large cracks on the electrode surface. The formation of pores in the lithiation or sodiation is seldom reported. But noteworthy, for the Na-Sn system, a prior work also reported the presence of pores after the sodiation of the Sn film electrode [159], which is consistent with our finding, and further pointed out that this phenomenon might be related to gas generation due to the electrolyte decomposition.

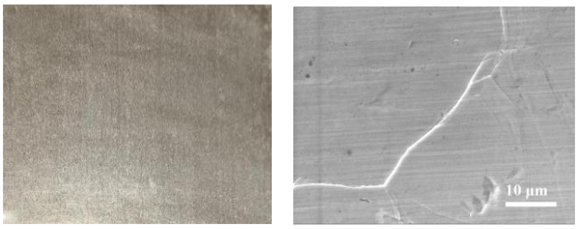

Figure 5.2 The photographic(left) and SEM (right) image of the fresh Sn foil electrode before cycling.

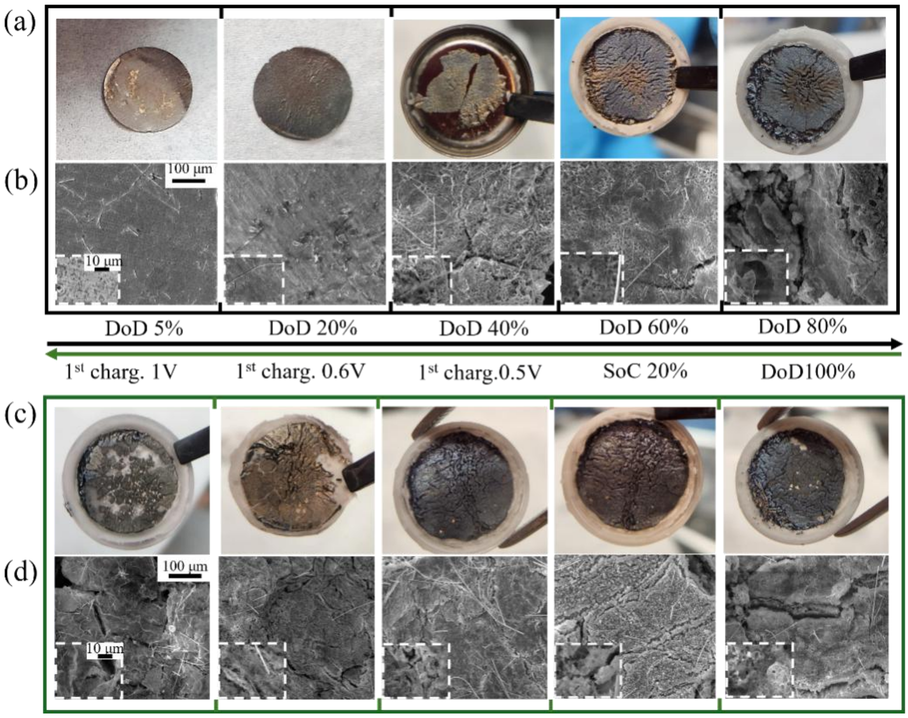

Figure 5.3 (a)(c)The photographic and (b) (d) SEM images of Sn foil electrodes after different depths of discharge (DoD) and states of charge (SoC) in cycle 1 at 0.01 C.

In the desodiation, the electrode integrity can hardly be maintained as more Na is extracted from the electrode (Figure 5.3c). Particularly for the case of desodiation to above 0.5 V, the electrode shows a disk dark shape disintegrated into many small pieces, indicating severe structural damage. This could account for the noise in the desodiation profile of the Sn electrode after 0.5 V. Further SEM analysis on the electrode morphology (Figure 5.3d) shows that the electrode surfaces are all characteristic of cracks and voids during the desodiation process, although the electrode at deep desodiation depth looks relatively smooth and dense compared to the one at shallow desodiation.

5.2.3 The Reversibility of Different Phase Transformations

Here the electrochemical performance of half cells with Sn foil electrodes is examined, as shown in Figure 5.4. When pursuing the full capacity of the Sn electrode (i.e., cycling between 0.001-1 V), the electrode displays a low initial coulombic efficiency (CE) of ~40% (Figure 5.4a). The low CE was also reported by previous works on Sn composite electrodes, which is presumed to be associated with the SEI formation, and the kinetic issues related to ion/electron transport [102, 157]. Compared to the initial cycle, three sodiation plateaus are also observed in the second cycle but they become short and sloping, and the capacity decays to ~8 mAh·cm^{-2} (~377 mAh·g^{-1}). Meanwhile, only two short plateaus occur in the second desodiation, giving a reversible capacity of ~3.5 mAh·cm^{-2} (~164 mAh·g^{-1}), corresponding to a low coloumbic efficiency of ~43%. Even worse, the cell does not work anymore after 3 cycles (Figure 5.4e), which is likely related to the electrode structural damage caused by huge volume change during full cycling.

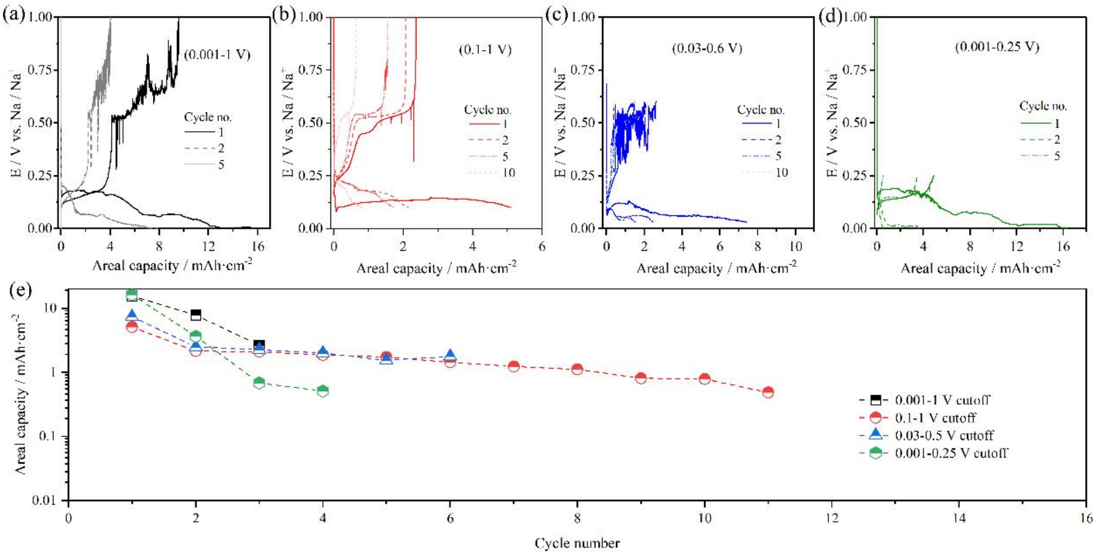

Figure 5.4 The voltage profiles of Sn electrodes at different cutoff voltages, (a) 0.001-1V, (b) 0.1-1 V, (c) 0.03-0.6V, (d) 0.001-0.25 V. (e)The capacity retention of Sn electrodes at the above same voltage windows.

The reversibility of each pair of phase transformation (i.e., Sn/NaSn, NaSn/Na$_9$Sn$_4$, Na$_9$Sn$_4$/Na$_{15}$Sn$_4$) in the Sn electrode is then explored by controlling the cut-off voltages (i.e., 0.1-1 V, 0.03-0.6V, 0.001-0.25 V) to examine the cyclability of partial sodiation. The cell cycled within 0.1-1 V (Figure 5.4b) delivered a sodiation capacity of 5 mAh·cm^{-2} (~220 mAh·g^{-1}), close to the theoretical capacity of NaSn (225 mAh·g^{-1}), but only 43% reversible capacity is obtained in the subsequent desodiation. The incomplete desodiation for this shallow cycling is supposed to be likely related to the kinetic limitation. A close look at the initial voltage profile shows that three short desodiation plateaus (at ~0.28 V, ~0.45 V, and ~0.55 V, respectively) appear, in contrast to one sodiation plateau at ~0.13 V. This implies that three different phase transitions between Sn and Na$_x$Sn (x<1) occur simultaneously at ~0.13 V in the sodiation process, and the observation of this multiple-phase sodiation plateau is probably the result of the overlap of three reactions due to the close reaction potentials and the kinetic limitation in Sn foil electrode [160]. For the case of cycling between 0.03-0.6 V and 0.001-0.25 V (Figure 5.4cd), the electrode delivers a reversible capacity of ~3 mAh·cm^{-2} (~120 mAh·g^{-1}) and ~5 mAh·cm^{-2} (~200 mAh·g^{-1}), and the initial coulombic efficiency of around 68% and 83%, respectively. The capacity retention as a function of cycle number at different voltage windows is plotted in Figure 5.4e. All the cells show poor cycling performance.

5.2.4 Electrochemical Kinetics of Sn Electrodes

From the previous analysis, in addition to the irreversible structural damage (e.g., cracks, and voids in Figure 5.3bd), the kinetic limitation in Sn foil electrodes also plays a role in their electrochemical performance (e.g., coulombic efficiency, cycle life). Here we employ the in-situ EIS to investigate the electrochemical kinetic of Sn electrodes, aiming at understanding the origin of the kinetic limitation responsible for the poor electrochemical performance or the limiting factors (charge transfer or ion diffusion kinetics) for the poor electrochemical performance.

5.2.4.1 Cell Design Optimization

To reliably interpret the electrochemical kinetics of the electrode, we first optimize the appropriate cell configuration for the impedance measurements. Many literatures generally use half-cell configuration for electrochemical characterizations because of the convenience. However, the half-cell configuration seems to be not suitable for our study for several reasons. First, the counter electrode Na metal is prone to react with the electrolyte to form the non-conductive passive layer (SEI) once contacting with the electrolyte, causing a high interfacial resistance [161]. As illustrated in Figure 5.5a, the impedance of Na//Na symmetric cells is much higher than that of Na_xSn//Na_xSn symmetric cells. As a result, in the Na_xSn//Na system, the cell impedance could be dominated by the impedance of the Na counter electrode. Hence it is difficult to distinguish the impedance of the working electrode from the combined impedance spectra (i.e., Na_xSn or Sn). Second, as the counter electrode potential is not stable when the current flows through it, it is hard to control the potential of the working electrodes during the potentiostatic or galvanostatic measurements accurately. Third, the impedance of Na//Na symmetric cells change significantly with the charging time (Figure 5.5b), which also causes difficulty in tracking the impedance variation of the working electrode from the total impedance change. A possible alternative approach here is to introduce an additional reference electrode to construct the three-electrode cell configuration, in which the potential of the working electrode is monitored with respect to the reference electrode and any deviation from the applied potential will be automatically corrected by adjusting the current between the working and counter electrodes [115].

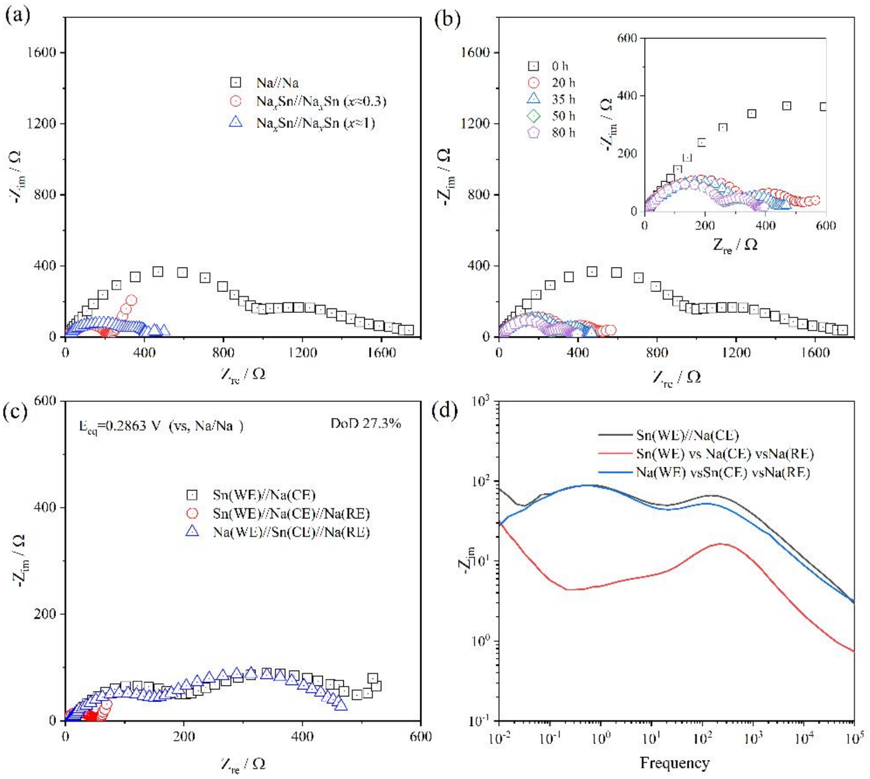

Figure 5.5 (a) Comparison of impedance spectra of Na//Na and $Na_xSn//Na_xSn$ symmetric coin-cells, (b) Impedance spectra of Na//Na symmetric cells at different charge time, (c) Comparison of Nyquist plots and (d) the imaginary part of Sn//Na cell, Sn//Na//Na, and Na//Sn//Na measured by Swagelok three-electrode cell configuration at DoD 27.3%. WE: working electrode, CE: counter electrode, RE: reference electrode.

Moreover, the three-electrode configuration allows measuring the impedance of individual electrodes [162]. As shown in Figure 5.5cd, the impedance spectra of the $Na_xSn//Na$ cell are approximately equal to the sum of the spectra of Na_xSn and metallic Na electrode as working electrode in the three-electrode measurement systems, and the impedance of Na metal dominates the total impedance of the Sn//Na cells both in low-frequency and high-frequency regions. In addition, the impedance of Na (and Na_xSn) electrodes in three-electrode and Na//Na ($Na_xSn//Na_xSn$) symmetric cell systems are close, which further verifies our previous hypothesis. Thereby, the three-electrode cell configuration is used here to accurately track the impedance variation of the Sn electrode during the (de-)sodiation.

5.2.4.2 Analysis of SoC-dependent Charge Transfer and Diffusion Resistance

Figure 5.6 shows the impedance spectra of pristine Sn foil electrodes before the sodiation. The impedance of the Sn electrode displays capacitive behavior, with a very small semicircle observed in very high frequencies, like many metals (e.g., Cu). Figure 5.7b and c shows the impedance change of Sn foil electrodes sodiated to different states in the initial cycle, which are highlighted by bold dots in Figure 5.7a. As the electrode is sodiated, the impedance spectra show three major features: first, an intercept at the *x*-axis at high frequencies, which is usually regarded as the sum of the electrolyte resistance between the working and reference electrode, the contact resistance between the electrode and electrolyte, the resistance of the system connecting line at three-electrode set-up [162]; second, two capacitance semicircles at mid-to-high frequency region, normally originating from the resistance of the surface passivation film (i.e., solid electrolyte interface (SEI)) and charge transfer; third, a straight line at low-frequency region associated with the mass transport process, known as the Warburg region. A careful examination shows that two semicircles are both stretched, probably due to the imperfect electrode surface and/or the overlap of the electrochemical processes. Moreover, with the increasing depth of sodiation (or DoD), the Warburg region becomes less and less obvious. Particularly for the case of DoD >50%, the Warburg region at low frequencies overlaps with the region dominated by the charge transfer at mid-frequencies, resulting in a significant deviation of the ideal straight line. As a result, the impedance spectra are characteristic of two or three semicircles at DoD >50%.

Since the frequency region dominated by SEI and the charge transfer usually overlap under non-blocking conditions (i.e., the Faradic reaction process), and the Warburg region also overlaps with the region of charge transfer, it is difficult to distinguish each of them from the cell impedance [163]. DRT tools are therefore used to help separate the physical and electrochemical processes that occurred in the Sn electrode, with the analysis results (using the Matlab hardware) shown in Figure 5.7de. Detailed information on the DRT technique is given in the Experimental section. Several peaks are observed, indicating the physical and electrochemical processes that occur in the sodiation of Sn electrodes. The nature of these peaks will be analyzed in detail afterward.

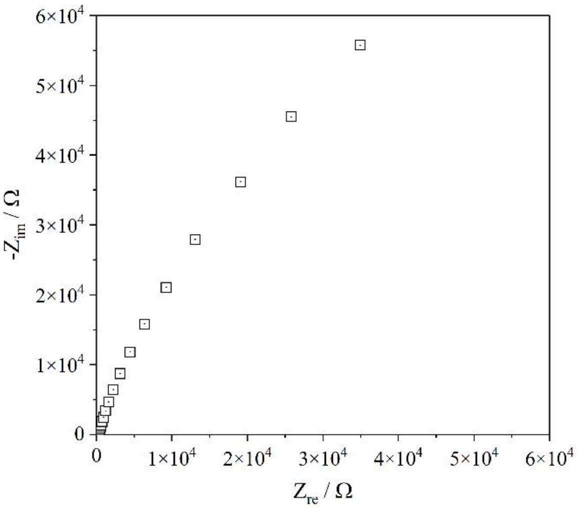

Figure 5.6 The impedance spectra of fresh Sn foil electrodes measured using a 3-electrode setup.

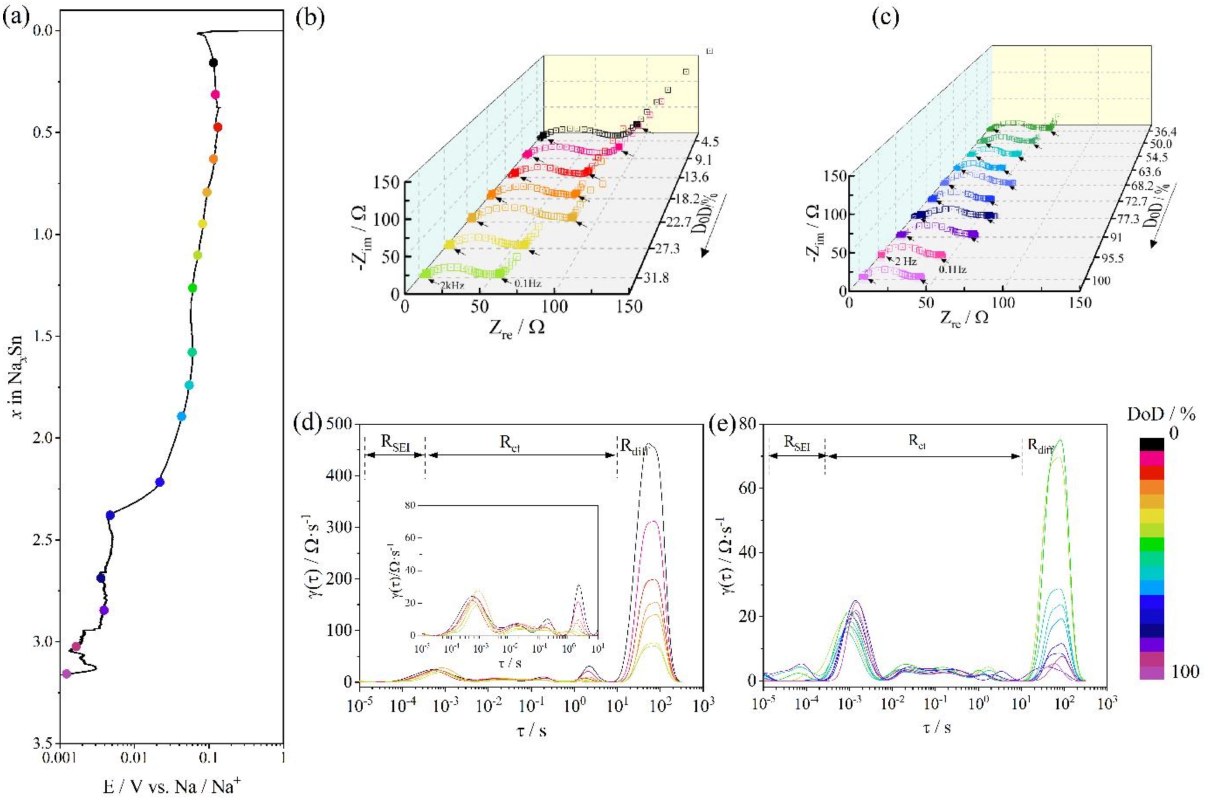

Figure 5.7 The impedance analysis of Sn foil electrodes during the initial sodiation process. (a) The Na content (x)-voltage profile. (b) (c) The Nyquist plots at different DoDs, which are marked in Figure 5.7a. The DRT analysis of the impedance spectra at DoD (d) below 32%, (e) above 32%, corresponding to Figure 5.7b and c, respectively. The measurements are all conducted using a 3-electrode setup with Sn foil, and two Na metal foil as working, counter, and reference electrodes, respectively.

The impedance change of the electrode during the initial desodiation process is also examined. Figure 5.8b and c shows the impedance spectra of the electrode at different SoCs, which is marked by the bold dots in Figure 5.8a. All the spectra feature by capacitive semicircle followed by a straight line. Differently, at low SoC (<46%), two semicircles are observed but only one semicircle at the high-frequency region is visible, especially at SoC larger than 46%. Moreover, as the SoC goes up, the capacitive semicircle becomes less significant, and the cell impedance spectra are characteristic of the straight line (particularly at SoC >70%). DRT technique is also used to distribute the electrochemical process in the initial desodiation of Sn electrodes. Figure 5.8de shows the DRT analysis of the impedance spectra at different SoCs. When combined with the DRT interpretation in Figure 5.7de, one may generally divide the whole relaxation time range into three relaxation time regimes: 10^{-5}-5×10^{-4} s, 5×10^{-4}-10 s, and 10-10^{2} s, which display the different electrochemical processes. The DRT peaks located between 10^{-5}-5×10^{-4}, undergo irreversible evolution in the sodiation and deosidation process. Meanwhile, these peaks tend to become stable after the SoC >52%. These features indicate that the peaks at 10^{-5}-5×10^{-4} are probably the result of the dominant contribution of the ion transport through the surface passivation layer (i.e., SEI). The relaxation process at the range of 5×10^{-4}-10 s is basically reversible in the (de-)sodiation, which could be dominated by the charge transfer. It is also worth mentioning that since the electrode during the sodiation is composed of multiple Na-Sn phases due to the inhomogeneous sodiation and kinetic limitation (XRD results in Figure 5.1b), several DRT peaks at the relaxation time range of 5×10^{-4}-10 s might be associated with different charge transfer processes occurred in Sn or Na_xSn (x<1) phase. Additionally, the peak at 10-10^2 s decreases with the increasing DoD and reversibly increases with the rising SoC, which could be associated with the ion diffusion process. A close examination shows that DRT peaks dominated by the charge transfers tend to overlap with the ones dominated by ion diffusion at high SoCs (e.g., 100% SoC).

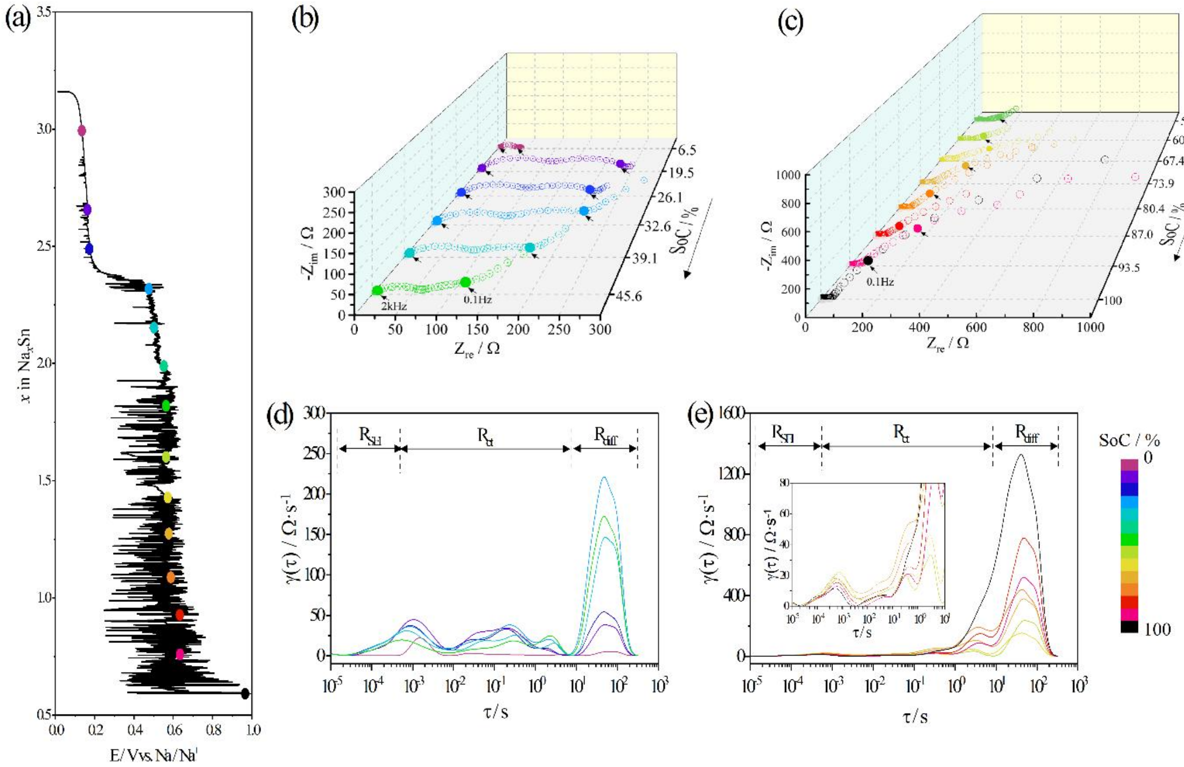

Figure 5.8 The impedance analysis of Sn foil electrodes during the initial de-sodiation process. (a) The sodium content (x)-voltage profile. (b) (c) Nyquist plots at different SoCs. The DRT analysis of the impedance spectra, (d) at SoC below 60%, and (e) beyond 60%.

To quantify the impedance contributed by different electrochemical processes in Sn electrodes, we approximately regarded the real part of the impedance in the frequency range of 100-2 kHz, 2 kHz-0.1 Hz, and below 0.1 Hz as the SEI (R_{SEI}), charge transfer (R_{ct}) and diffusion (R_{diff}) resistance based on the DRT analysis, which is shown in Figure 5.9a. The resistance contributed by SEI, charge transfer, and ion diffusion at different DoDs and SoCs is all extracted from the EIS spectra and plotted in Figure 5.9b and c, respectively. Overall, in the sodiation, the cell impedance is largely dominated by the diffusion and charge transfer resistance at low DoD <30% while the charge transfer resistance tends to dominate the cell impedance.with the DoD going up. In contrast, for the desodiation process, the cell impedance is dominated by the charge transfer resistance at SoC<40%. As the SoC increases from 40% to 90%, both the charge transfer and the diffusion resistance dominate the cell impedance, but at the SoC >90% the diffusion resistance alone dominates the cell impedance.

Specifically, the high-frequency resistance (R_{HF}) of the cells, exacted from the *x*-intercept at high frequencies, basically stays stable at the level of ~2 ohms, independent of DoD and SoC. SEI resistance shows a slight decrease with the increasing DoD and does not change obviously in the desodiation. As for diffusion resistance, it shows an obvious decline as the sodiation proceeds, but increases significantly with the increasing SoC, particularly at SoC >60%, indicating the reversible process of diffusion in the (de-)sodiation. In addition, the value of R_{ct} does not change significantly in the sodiation process. Differently, the charge transfer resistance begins to increase evidently upon the desodiation depth larger than 5%, while maintaining relatively stable after the SoC > 19.5%.

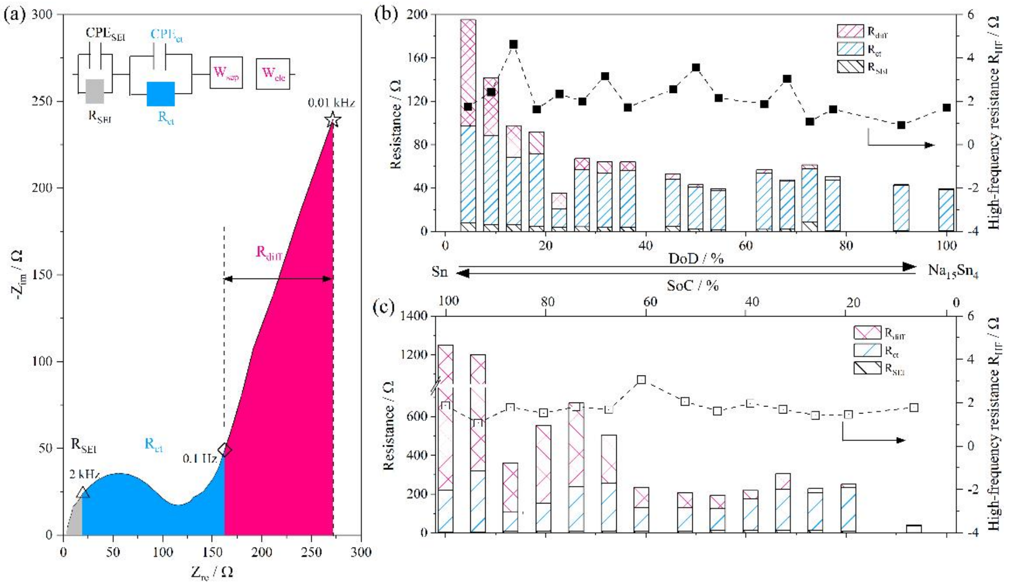

Figure 5.9 (a) An example of resistance contributed by different processes. Comparisons of the high-frequency resistance (R_{HF}), the SEI (R_{SEI}), charge transfer (R_{ct}), and diffusion (R_{diff}) resistance at, (b) different DoDs and (c) different SoCs in cycle 1.

5.2.4.3 Sodium Diffusion Coefficient in Na$_x$Sn

The ion diffusion coefficient is an important indicator for mass transport kinetic in electrodes, which can be extracted from the Warburg impedance in the low-frequency region according to equation 2.6 (Chapter 2), assuming the semi-infinite diffusion model [164]. In this case, the real part (Z_{re}) and imaginary part (Z_{im}) of the impedance behave as $\sigma_w\omega^{-0.5}$ and $-\sigma_w\omega^{-0.5}$ (σ: the Warburg coefficient), which accounts for a 45-degree straight line in low-frequencies in the Nyquist plot. Theoretically, the accurate determination of the Warburg coefficient σ can be obtained from both the frequency-dependent Z_{re} and Z_{im} at the low-frequency region. But since the real part is the accumulation of the impedance contributed by different processes while the imaginary part will reach the minimum (normally close to zero) at the transition from charge transfer to ion diffusion region, the latter seems to reflect a better Warburg behavior [160]. More importantly, in real electrochemical systems, the frequency range dominated by the charge transfer and ion transport are often overlapped particularly when the electrode particle is nanosized (i.e., the diffusion kinetic is relatively fast and the system is limited by the charge transfer). This makes the Warburg behavior very difficult to observe in the real part, thereby resulting in a deviation of impedance spectra from the ideal 45-degree straight line at low-frequencies [160]. In this regard, it seems better to accurately determine the Warburg coefficient by analyzing the frequency-dependent imaginary part. Here inspired by Anne's work [160], we also attempt to extract the Warburg impedance coefficient σ based on the imaginary part Z_{im}. Theoretically, when the $-Z_{im} \cdot \omega^{0.5}$ reaches the minimum value at low frequencies, the system reaches semi-infinite diffusion conditions. Thus, the Warburg impedance coefficient σ can be extracted from the minimum value. For the convenience of determining the diffusion coefficient by Equation 2.6, we establish the relation between $(1/2^{0.5} Z_{im} \omega^{0.5})^2$ and frequency ω, with an example shown in Figures 5.10c and d for the initial sodiation and desodiation process, which are derived from the EIS results in Figures 5.10a and b, respectively. The frequency range reaching the semi-infinite diffusion conditions is clearly observed and marked by a gray-shaded square when the $(1/2^{0.5} Z_{im} \omega^{0.5})^2$ reach the maximum. Therefore, the value of $(1/2^{0.5} \sigma)^2$ can be directly obtained from the maximum value of $(1/2^{0.5} Z_{im} \omega^{0.5})^2$. Similarly, the plot of $(1/2^{0.5} Z_{im} \omega^{0.5})^2$ versus ω at different DoDs and SoCs is presented in Figures 5.10e and f. From these plots, one can clearly see the maximum value $(1/2^{0.5} Z_{im} \omega^{0.5})^2$ for all cases, which determines the accurate value of $(1/2^{0.5} \sigma)^2$ at different potentials. These obtained Warburg coefficient values are all summarized in Figure 5.10g and h. It is observed that the change in $(1/2^{0.5} \sigma)^2$ as a function of DoD and SoC are approximately reversible: the value tends to gradually increase with the climbing DoD, while it undergoes a decrease with the increasing SoC.

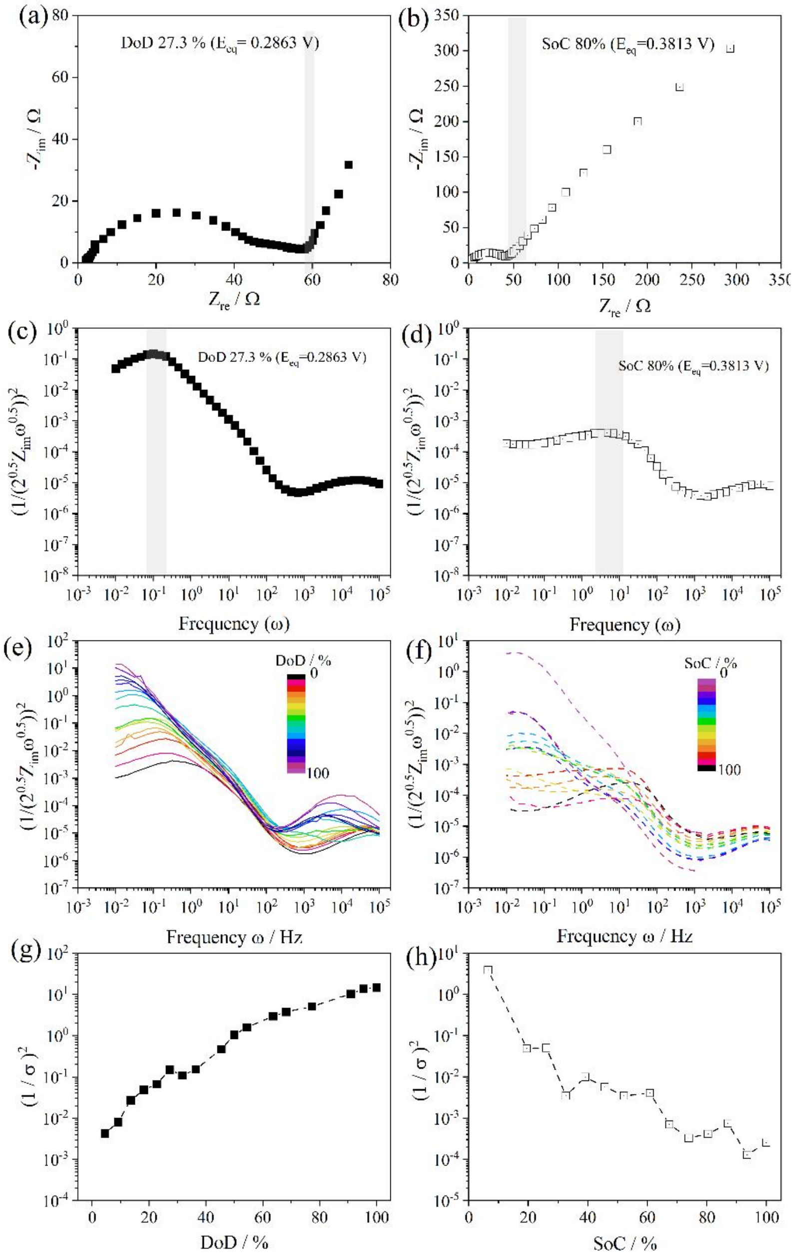

Figure 5.10 The impedance analysis of the Sn//Na//Na three-electrode cells in the sodiation (a, c, e, g) and desodiation (b, d, f, h) process. (a) The impedance spectra measured at 27.3% DoD (the equilibrium potential of the cells is around 0.2863 V vs. Na/Na$^+$). (b) The impedance spectra of the Sn//Na//Na three-electrode cells measured at 80% SoC (the equilibrium potential of the cells is around 0.3813 V vs. Na/Na$^+$). (c) The $(1/2^{0.5}Z_{im}\omega^{0.5})^2$ versus ω plot of the same cell at the same DoD in Figure 5.10a. The shaded region presents the frequency zone in which the semi-infinite conditions approximately approach. (d) The $(1/2^{0.5}Z_{im}\omega^{0.5})^2$ versus ω plot of the same cell at the same SoC in Figure 5.10b. The shaded region presents the frequency zone in which the semi-infinite conditions approximately approach. (e) Frequency-dependent $(1/2^{0.5}Z_{im}\omega^{0.5})^2$ of the cells at different DoDs. (f) Frequency-dependent $(1/2^{0.5}Z_{im}\omega^{0.5})^2$ of the cells at different SoCs. (g) The DoD-dependent $(1/2^{0.5}\sigma)^2$ derived from Figure 5.10e. (h) The SoC-dependent $(1/2^{0.5}\sigma)^2$ derived from Figure 5.10f.

The apparent chemical diffusivity of sodium in Na_xSn at room temperature derived from the above Warburg coefficient values (Figure 5.10 g and h) are plotted as a function of DoD and SoC, as shown in Figure 5.11. The chemical sodium diffusivity is found to vary between 10^{-12}~10^{-18} $cm^2 \cdot s^{-1}$ in the initial cycle. Moreover, the sodium diffusivity tends to be higher at the beginning of the desodiation (or the high sodiation depth), compared to the deep desodiation (or the low sodiation depth). This indicated the faster diffusion kinetics in the high-order Na-Sn phases than low-order Na-Sn phases. In addition, it is observed that the sodium diffusivity in the sodiation seems to be one order of magnitude higher than that in the desodiation, which might be associated with the mossy electrode structure during the sodiation. Many voids are formed in the sodiation and will be filled with liquid electrolytes. This could result in increased active surface area and shortened diffusion distance, thus improving the sodium diffusion kinetics significantly [165].

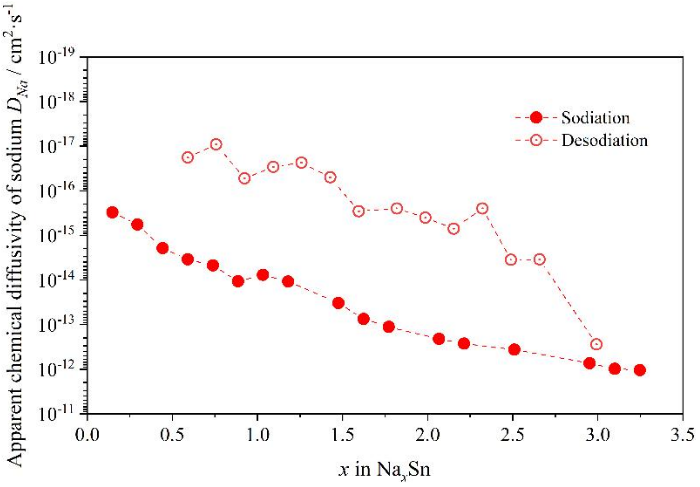

Figure 5.11 Apparent chemical diffusivity of sodium in Na_xSn during the initial sodiation and desodiation process.

5. 3 Discussion

5.3.1 The Implication of the Impedance Analysis

From our previous impedance result (section 5.2.4.2), the dominance of charge transfer and diffusion resistance in the cell impedance at low DoDs <30% suggests that the phase transformation of Sn and low-order Na-Sn phases is governed by both the charge transfer and diffusion process. As the sodiation depth goes up to and beyond 30% (i.e., DoD >30%), the predominant contribution of charge transfer resistance to the cell impedance implies the sluggish charge transfer kinetic as the origin of the kinetic limitation that is partly responsible for the poor cycling stability for the transformations between high-order Na-Sn phases. The important role of charge transfer in the sodiation of Sn electrodes is in agreement with the previous works, which reported the high resistivity of the NaSn phase as the primary origin of the high coulombic efficiency loss in Sn electrodes [102, 149].

For the desodiation, the role that the charge transfer or diffusion kinetics plays in the phase transformations of Sn foil electrodes is slightly different. The dominant role of the charge transfer resistance at low SoC (<40%) indicates that the charge transfer is largely the rate-limiting step for the phase transformations between the high-order Na-Sn phases (e.g., Na_9Sn_4, $Na_{15}Pb_4$). At the SoC of 40-90%, the dominance of charge transfer and diffusion in the cell impedance reveals that the transformation between medium-order Na-Sn phases is probably controlled by the mixed diffusion/charge transfer kinetics. Additionally, the dominant contribution of the diffusion resistance at high SoCs >90% provides an implication that the electrochemical desodiation of Sn electrodes at the end is largely limited by the diffusion kinetic. This is also supported by the low sodium chemical diffusivity (~10^{-17} $cm^{-2} \cdot s^{-1}$) in low-order Na_xSn ($x<1$) calculated from the Warburg coefficient (section 5.2.4.3).

5.3.2 Comparison of Sodium Diffusivity with Other Literature

Figure 5.12 shows comparisons of the apparent chemical diffusivity in this work with the previously reported data on the Sn composite electrode during the initial desodiation process. It is observed that the sodium diffusivity estimated by EIS in this work is roughly 2-3 orders of magnitude lower than the reported results derived by GITT in Sarkar et al's work [104]. This minor discrepancy in the diffusivity is considered to be related to their difference in electrode design (Sn foil in this work vs. micro-sized Sn particle in literature), the electrolyte, and applied methods. Noteworthy, since in this work the estimation of the chemical diffusivity, based on the single-phase EIS technique, does not consider the impact of phase transformation or mechanical stress during the desodiation, the obtained sodium diffusivity reflects the apparent diffusivity of sodium in the Na_xSn phase rather than the true sodium diffusivity value in individual NaSn, Na_9Sn_4, $Na_{15}Sn_4$ phase.

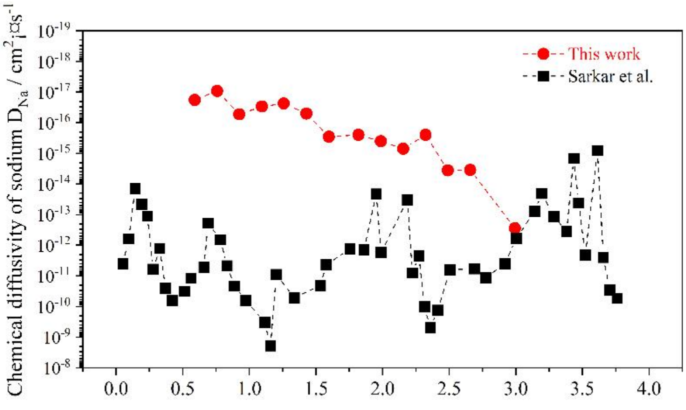

Figure 5.12 The composition-dependent chemical sodium diffusivity in Na_xSn in this work compared with the previously reported diffusivity data in tin composite electrodes (microsized Sn particles) during the initial desodiation (charge) process.

Additionally, in contrast to other electrodes, the sodium diffusivity in Na_xSn is relatively low. For instance, the chemical diffusivity of sodium in Na_xSb is estimated by GITT to be in the order of ~10^{-9} $cm^2\cdot s^{-1}$ [166]. For the P composite electrode and Ge thin film electrode, the sodium diffusivity is calculated to be approximately ~10^{-14} and ~10^{-13} $cm^2\cdot s^{-1}$ respectively [89, 167]. Also, Wang et al reported the sodium diffusivity in bismuth composite electrodes varies between ~10^{-12}-10^{-14} $cm^2\cdot s^{-1}$ during the sodiation [168]. These values are all significantly higher than those in Na_xSn. Therefore, the low sodium diffusion in Na_xSn might be one possible reason for the poor electrochemical performance of Sn foil electrodes.

5. 4 Conclusion

In this work, Sn foil as the SIB electrode is examined using electrochemical techniques and structural analysis. Three distinctive sodiation plateaus are observed in the initial sodiation, giving a specific capacity of ~695 $mAh\cdot g^{-1}$ at 0.01 C. XRD result confirms the simultaneous formation of Na-Sn intermetallic phases (i.e., NaSn, Na_9Sn_4, $Na_{15}Sn_4$), which is ascribed to the kinetic limitation in foil electrode. Cycling tests show the Sn electrode has a short cycle life (i.e., 2-3 cycles) when the full capacity is pursued, which is largely related to the electrode's mechanical damage (e.g., cracks and voids). Also, for partly cycling, the electrode capacity decays quickly to zero in less than 12 cycles. Meanwhile, the initial coulombic efficiency for shallow cycling between 0.1-1V is as low as 40%, implying the kinetic loss related to the charge transfer and/or ion diffusion. To further understand the limiting factors for the electrochemical behavior of Sn electrodes, the in-situ EIS technique is employed to investigate the charge transfer and diffusion kinetics comprehensively. A three-electrode cell configuration rather than a coin cell configuration is used for EIS measurements, which allows accurate tracking of the working electrode impedance. With the help of DRT tools, we separated different electrochemical processes across the whole frequency range and found that the high-frequency resistance (R_{HF}) does not change evidently in all cases. However, the charge transfer resistance undergoes an increase at the very early stage of desodiation. The resistance of ion diffusing through the electrodes tends to be much larger at low DoDs (or high SoCs) than at high DoDs (or low SoCs). By quantifying their contribution to the cell impedance, it is found that both the diffusion resistance and the charge transfer resistance dominated the cell impedance at low DoDs (<30%), implying the sluggish diffusion and charge transfer kinetic may be the origin of the kinetic limitation, while at high DoDs >30%, the cell impedance is dominated by the charge transfer resistance, suggesting the charge transfer is likely the rate-limiting step for the transformation between high-order Na-Sn phases.

Chapter 6: Sodium Insertion into Pb

6. 1. Introduction

Amongst the alloy anode candidates for SIBs, Pb is known to form a highly-sodiated phase of $Na_{15}Pb_4$, yielding a specific capacity of 485 mAh·g^{-1} or 1175 mAh·cm^{-3} (with respect to the volume of $Na_{15}Pb_4$ alloy) [100, 169]. However, Pb or Pb-based materials are often neglected by the community because of their toxicity and environmental impacts, having been subject to notable industrial restrictions in the past, such as RoHS and REACH. With such scrutiny, it is only natural that supply chain tightening has coincided with a recycling rate of Pb that is currently more than 99%, marking one of the highest recycling rates worldwide of elements [97]. As noted in a recently published paper [170], all Pb-containing components are reported to be readily recycled from the Pb-acid batteries. For Na-ion batteries, besides the attractive volumetric capacity, the Pb electrode also possesses the metrics of cost-effectiveness ($2 per kg), high abundance, and acceptable conductivity [100, 169]. In addition, the large atomic size of Pb can offer more interstitial space to accommodate sodium, likely resulting in more favorable sodiation kinetics [100]. Still, common to all alloy anodes, Pb also suffers from volume change-induced structural failure, and therefore a poor cycle life [171]. For example, an early study showed that the electrochemical sodiation of the Pb composite electrode ends at the $Na_{15}Pb_4$ phase with a theoretical capacity of 485 mAh·g^{-1}, giving a volume expansion up to ~365% [172]. This significant volume expansion and contraction makes the cycle life of pure Pb film electrodes less than 20 cycles [79], far from the industrially acceptable level, which renders its practical utilization.

It is well-recognized that the volume change is directly linked to the phase transformations that occur during the electrochemical (de-)sodiation. The sodiation mechanisms of Pb anodes remain poorly understood with only a few works being published over the years. Jow, et al. (1987), for the first time, reported that the alloying of Pb with Na occurs in four steps, leading to the formation of four distinct Na-Pb phases, i.e., $NaPb_3$, NaPb, Na_5Pb_2, and $Na_{15}Pb_4$ [19]. The final sodiation product of Pb is also confirmed by Komaba, et al. that the initial sodiation capacity of 480 mAh·g^{-1} matches ideally with the one calculated based on the atomic ratio of $Na_{3.75}Pb$ [126]. However, a recent study, which comprehensively explored the Na-storage mechanisms of Pb thin film electrodes using *in-situ* X-ray diffraction (XRD) technique, reveals that the electrochemical sodiation of Pb does not completely follow the Na-Pb phase diagram: α-Na_9Pb_4, with a similar structure to Na_9Sn_4, is formed during the sodiation but rather than the earlier suggested Na_5Pb_2 phase [79]. A similar outcome was also reported later by Ali Darwiche et al. [97], whose operando XRD measurements verified the presence of $NaPb_3$, NaPb, Na_9Pb_4, and $Na_{15}Pb_4$ phases during the (de-)sodiation process of the electrode with microsized Pb particles as active material. Again, no Na_5Pb_2 phase was detected. Regardless of whether Na_5Pb_2 or Na_9Pb_4 is a thermodynamically stable phase at room temperature, there is almost no doubt that the electrochemical sodiation of Pb forms different successive intermetallic phases. Given that these Na-Pb phases (e.g., $NaPb_3$, NaPb, Na_9Pb_4/Na_5Pb_2, $Na_{15}Pb_4$) have different crystal structures and mechanical properties (e.g., elastic modulus, shear modulus), the reversibility of each phase transformation should also vary. Therefore, identifying which phase transformation plays a greater impact on the electrochemical performance is essential to assess whether or not solid, non-composite, Pb can be a reliable SIB anode in the future.

Here we use metallic Pb foil electrodes as the model system, because of its simple electrode design[173] and reduced cost [174]. Additionally, the foil presents alternative constraints compared to a composite electrode, whereby expansion and contraction are expected to be buffered to a varying degree by ductile, unreacted Pb. The Na-storage behavior of the Pb electrode in a foil architecture is systematically evaluated thereafter, building fundamental insights into the phase transformations, and discussing their role in causing electrode failure. By deliberately mitigating or circumventing the problematic phase transitions, the prolonged cycle life of Pb electrodes in SIBs can be realized.

6.2 Results

6.2.1 Initial (De-)Sodiation of Pb Foil Electrodes

Figure 6.1a shows the typical sodiation-desodiation (or discharge-charge) profile of the Pb foil electrode cycled at 0.1 mA (~C/177 considering the formation of $Na_{15}Pb_4$). As soon as the sodiation current is applied, the surface potential of the electrode rapidly drops to ~0.25 V (vs. Na/Na^+) and then rises to ~0.3 V. This potential difference of ~50 mV was defined by Wang et al. as the nucleation potential [175], which are regularly observed in alloy anodes for LIBs/SIBs [148]. Three distinct potential plateaus at around 0.3 V, 0.12 V, and 0.08 V vs. Na/Na^+ are observed one after another, delivering a specific capacity of ~480 $mAh \cdot g^{-1}$ (~1170 $mAh \cdot cm^{-3}$) after a sodiation until 1 mV vs. Na/Na^+, evidencing good consistency with previous reports [79, 97]. By extracting the capacities contributed by each potential plateau, it is found that these capacities match the ones upon the formation of $NaPb_3$, Na_9Pb_4/Na_5Pb_2, and $Na_{15}Pb_4$ based on calculations. When the current direction is inverted, the potential curve exhibits four potential plateaus at ~0.15 V, ~0.28 V, ~0.38 V, and ~0.5 V (vs. Na/Na^+), implying four Na-Pb two-phase equilibrium regions. Different from the relatively smooth sodiation curve, the desodiation one is relatively noisy, especially for the second and fourth plateaus. The noisy desodiation curve was also reported in the Sn electrode [159], which might be associated with the loss of electrical contact caused by mechanical damage. After the desodiation to 0.8 V vs. Na/Na^+, a specific capacity of ~450 $mAh \cdot g^{-1}$ is obtained, corresponding to ~93% of the initial sodiation capacity.

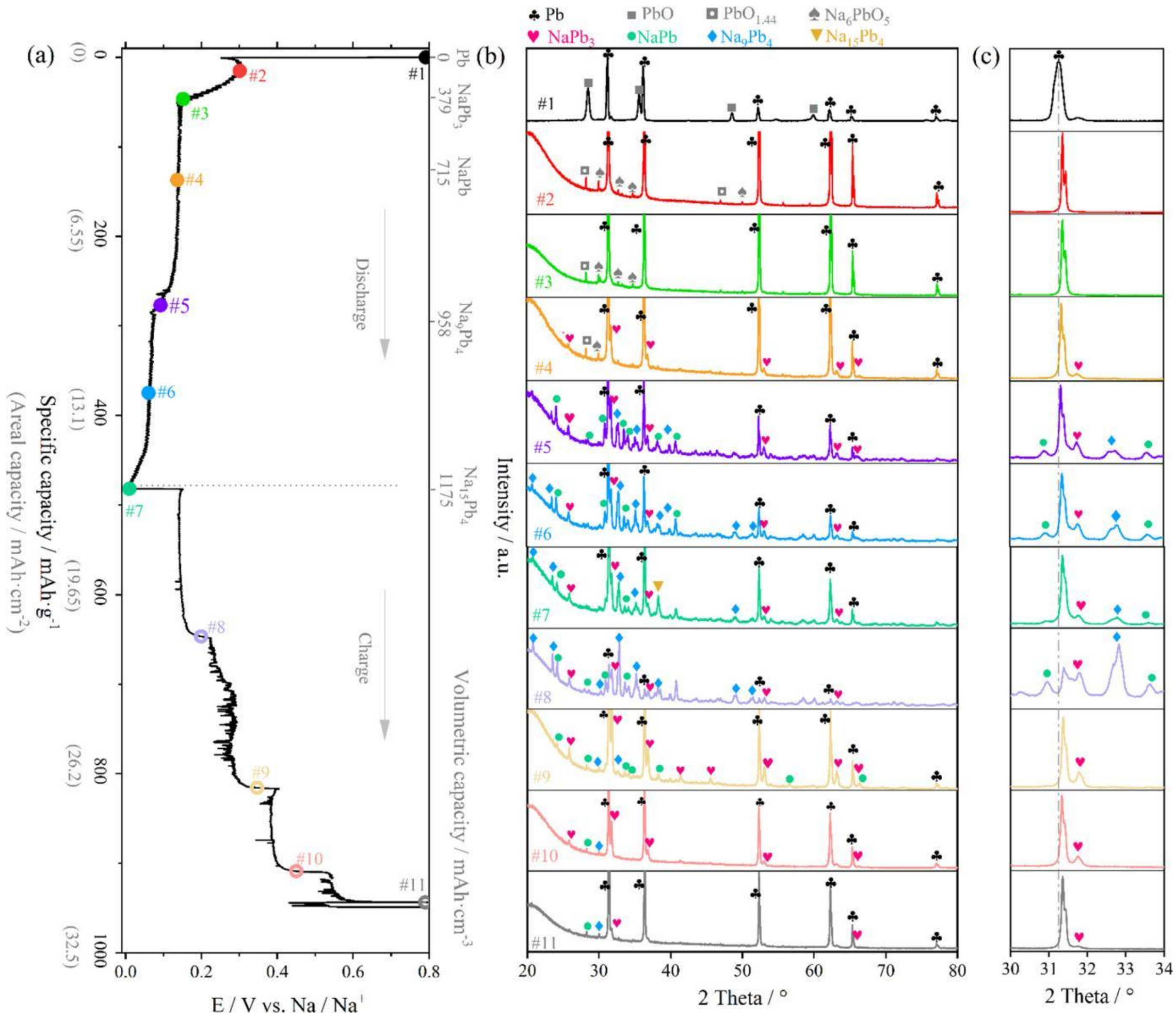

Figure 6.1 (a) The initial galvanostatic profile of a Pb//Na half-cell at a C-rate of 0.1 mA (12 mm electrode disk). (b) The XRD diffractograms of the Pb electrodes at different sodiation or desodiation states, which are highlighted by the colored dots in Figure 6.1a. (c) The enlarged XRD diffractogram in 2θ = 30°–34° for Figure 6.1b.

To examine whether the Na-Pb phases mentioned above are formed and assess their reversibility, a series of XRD tests were performed on the initial sodiation and desodiation of the Pb foil electrode. As shown in Figure 6.1b, prior to the sodiation (dot #1 in Figure 6.1a), the X-ray diffractogram of the pristine Pb foil (#1 in Figure 6.1b) is fitted to be the crystalline Pb phase (PDF #01-072-22773), and the PbO (PDF #00-035-1482), indicating that the surface of the Pb foil has been oxidized. As the sodiation capacity proceeds to ~1.42 mAh·cm^{-2} (dot #3 in Figure 6.1a), the diffractogram generally remains the same except for some additional minor peaks that likely correspond to the Na-Pb oxides (#3 in Figure 6.1b). Besides, no obvious peaks related to Na-Pb phases (i.e., $NaPb_3$) are detected. With further sodiation to a capacity of ~4.43 mAh·cm^{-2} (dot #4 in Figure 6.1a), diffraction peaks corresponding to the $NaPb_3$ phase appear, although the peaks of crystalline Pb remain the most prominent (#4 in Figure 6.1b). No diffraction peaks referring to higher-ordered crystalline Na-Pb phases (e.g., NaPb, Na_9Pb_4) are observed at this point. After the sodiation capacity reaches ~10.4 mAh·cm^{-2} (dot #5 in Figure 6.1a), the diffraction peaks corresponding to the higher-ordered phases of NaPb and Na_9Pb_4 finally appear (#5 in Figure 6.1b), in addition to the remaining $NaPb_3$ and Pb diffraction peaks. Even after the full sodiation to 0.001 V vs. Na/Na$^+$ (dot #7 in Figure 6.1a) at this small current, the typical diffraction peaks corresponding to Pb remain (#7 in Figure 6.1b). Taking a closer look at the two strong peaks at around 31° (Figure 6.1c), which agree with the standard ones of the Pb phase, one may see that they seem to shift slightly towards a higher 2θ angle with the increasing sodiation depth (highlighted by the gray dashed line in Figure 6.1c). One explanation for this peak shift is related to mechanical strain. The localized volume expansion caused by inhomogeneous sodiation compresses the neighboring unsodiated Pb grains, resulting in a decreased plane distance and thereby shifting the diffraction peak rightward (Bragg's law). Another possibility may have something to do with the thick Pb foil samples. As the phase boundary moves into the electrode, the diffraction from the Pb phase moves deeper into the electrode along the z-axis (i.e., a longer pathway for the X-ray). In this way, when the detector gets the diffracted X-ray from the sample, it may have already rotated to a slightly higher angle degree (given the scanning speed of 5°/min), thereby resulting in a larger measured 2θ, i.e., a rightward shifting peak. In either case, future studies are warranted.

Moreover, no strong evidence proves the presence of $Na_{15}Pb_4$, i.e., only one typical diffraction peak at 2θ = ~38° may be contributed by the $Na_{15}Pb_4$ phase (PDF #03-065-3168) while others can hardly be distinguished due to the peak overlapping. It is noted that the diffractogram of the fully sodiated Pb foil (to 0.001 V) also exhibits the features of a mixture of crystalline $NaPb_3$, NaPb, and Na_9Pb_4. The XRD results suggest that some of the phase transformations during sodiation are probably occurring simultaneously rather than sequentially, otherwise, peaks corresponding to the three Na-Pb phases (i.e., $NaPb_3$, NaPb, Na_9Pb_4) should not have been concurrently observed to such an extent.

When the electrode is desodiated to ~0.2 V vs. Na/Na$^+$ (dot #8 in Figure 6.1a), a typical diffraction peak at ~38.2° that is likely corresponding to $Na_{15}Pb_4$ diminishes, and more peaks appear simultaneously, which agrees with the typical diffraction peaks of Na_9Pb_4 reported by Ellis et al [79] (#8 in Figure 6.1b). The desodiation of the Pb foil anode to 0.35 V vs. Na/Na$^+$ (dot #9 in Figure 6.1a) results in the absence of some typical diffraction peaks that may originate from Na_9Pb_4 (e.g., at around 23.5°, 35°, 49°), and the presence of new peaks that may be contributed by NaPb (e.g., at 38°, 56°, 66.5°) and $NaPb_3$ (e.g., at 42° and 45°) (#9 in Figure 6.1b). For the electrode desodiated to 0.45 V vs. Na/Na$^+$ (dot #10 in Figure 6.1a), the prominent features of the diffractogram are consistent with those of $NaPb_3$ and Pb from the PDF cards #01-072-22773 and #03-065-3283, while some small peaks that are in line with standard peaks of Na_9Pb_4 and NaPb phases are also visible (#10 in Figure 6.1b). When the electrode is desodiated to 0.8 V vs. Na/Na$^+$ (dot #11 in Figure 6.1a), the main diffraction peaks of the diffractogram are in line with those of the metallic Pb phase, with minor peaks that may originate from $NaPb_3$, NaPb, or Na_9Pb_4 phases (#11 in

Figure 6.1b).

To summarize, multiple Na-Pb intermetallic phases are involved in the sodiation of the Pb foil electrode. These phases are suggested to be likely $NaPb_3$ NaPb, Na_9Pb_4/Na_5Pb_2, and $Na_{15}Pb_4$ based on the electrochemical data and the previous reports on Pb micro-sized particles[97] and thin films [79].

6.2.2 Surface Morphology Evolution of Pb Foil Electrodes

The surface morphology changes of the Pb foil anodes during the initial cycle are characterized by taking photographic and scanning electron microscopy (SEM) images. Figure 6.2 shows the photographic images and the corresponding SEM images taken at different states of (dis-)charge. Upon a 5% DoD (~0.85 mAh), the electrode is mostly covered by a sodiated layer and maintains its disk geometry (Figure 6.2a). With a deeper sodiation, i.e., 20% DoD, the electrode surface and shape do not change significantly by eye observation. The electrodes with ≥ 40% DoD, on the contrary, can hardly maintain their integrity and may break into parts after disassembly. Since the electrode with 80% DoD seems to hold its overall structure, it is suggested that the external force coming from the disassembly of the coin cell may partly be responsible for the structure collapse of the electrodes with 40%, 60%, and 100% DoD. Low- and high-magnification SEM images of the electrode at the same DoD are provided in Figure 6.2b. At 5% DoD, the sodiated layer grown on the electrode surface exhibits a shape of emerging spherical protrusions while the un-sodiated portion retains the same appearance as its pristine state with the rolling trace (Figure 6.3). When the DoD is higher, the features of the electrode surface do not seem to change significantly, and no obvious cracks are found in the chosen observation region. However, when the DoD reaches 80%, some small cracks on top of the protrusions (high-magnification SEM) can be observed. The electrode with 100% DoD becomes more catastrophic since the structure of protrusions opens up, leading to severe cracking.

From photographic images (Figure 6.2c), the electrode with 20% SoC completely loses its disk shape. With a higher SoC, the electrode seems to follow a trend that the higher the SoC, the lower the electrode integrity is. Especially when the SoC is beyond 60%, the electrode breaks into parts after disassembly. This structural damage may partly explain the noisy potential profile in Figure 6.1a. The SEM observations (Figure 6.2d) show that with the increasing SoC, the cracked protrusions on the electrode surface do not seem to be as evident as those in 0% SoC (i.e., 100% DoD). For instance, only some smaller cracks can be identified in the electrode surface at 100% SoC (green arrow in Figure 6.2d). Meanwhile, the surfaces of the electrodes with ≥ 40% SoC appear to be flatter, evidenced by the island-like protrusions that are not as compact, and the surface of the fully desodiated electrode seems to become mossy (highlighted by circles in Figure 6.2d). In addition, it should be noted that some glass fibers (marked in the red arrow in Figure 6.2b and 2d) are still observed on the electrode surface, although the electrode samples were rinsed using pure DMC solvents three times after the disassembly. This might be related to the stack pressure, which causes some glass fibers tightly attached to the rough surface of the electrode.

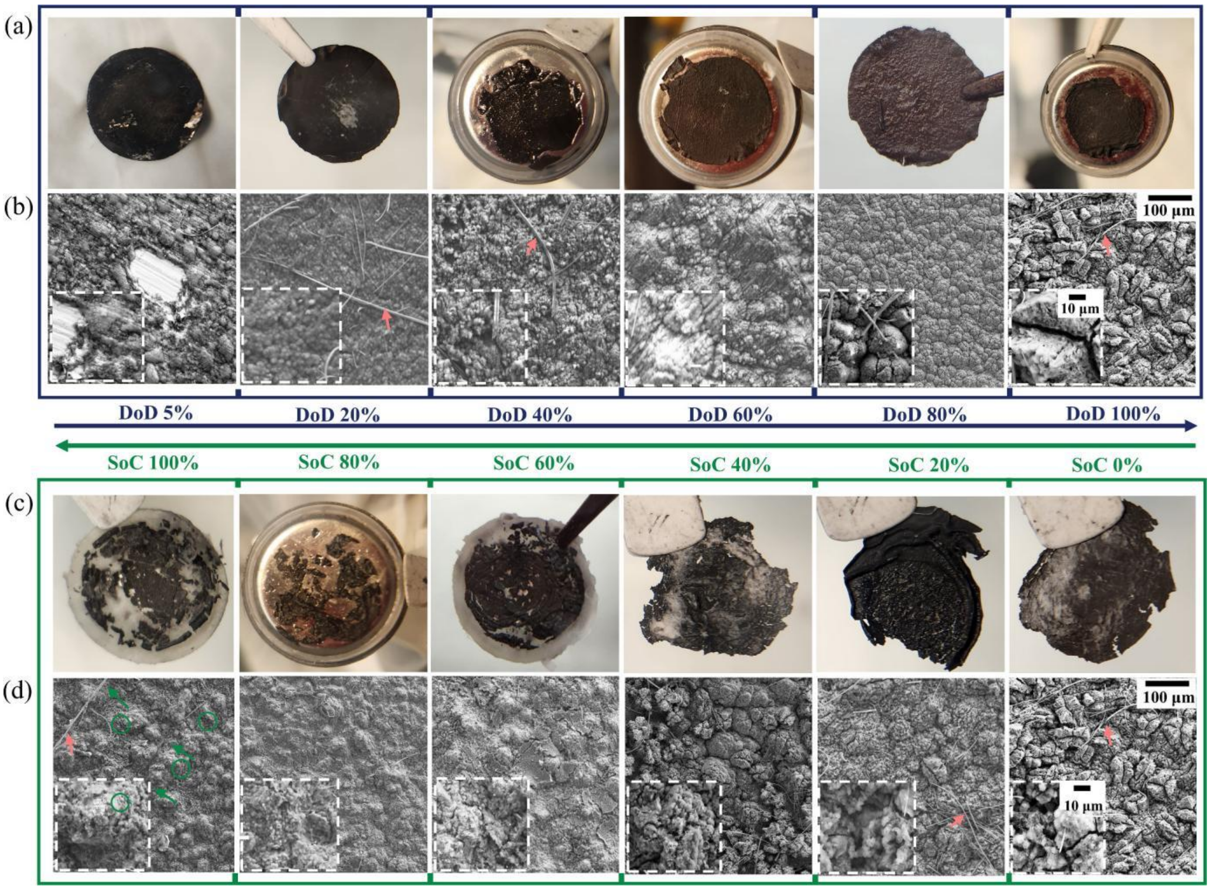

Figure 6.2 (a) (c) The photographic images and (b) (d) the corresponding SEM images (bottom) of the Pb foil electrode surface at different sodiation (or desodiation) states during the initial cycle. It is noted that the photographs were taken on the rinsed electrode sample at different DoD or SoC in the glovebox. The cracks and voids are highlighted in green arrows and circles, while the residue glass fiber on the electrode surface is marked in red arrows.

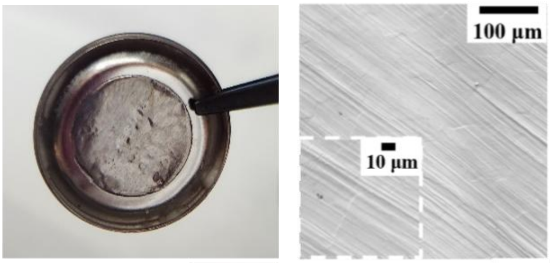

Figure 6.3 The photographic (left) and SEM images (right) of pristine Pb foil.

6.2.3 Reversibility of Different Phase Transformations

Theoretically, the full sodiation of Pb upon the formation of $Na_{15}Pb_4$ will give rise to a volume expansion of ~ 365%, which could induce huge internal strain in the electrode, therefore leading to mechanical damage like cracking (as shown in Figure 6.2b and d) and pulverization [97]. As anticipated, the galvanostatic charge-discharge (GCD) results (Figures 6.4a and b) show that the Pb foil electrode cycled within 0.001-0.8 V stops functioning after only 3 cycles, and the failure mechanisms have not been reported yet. Taking a close look at the GCD curves, one can see that there are four potential plateaus during the second sodiation, in contrast to three ones in the initial sodiation. The second desodiation becomes even more catastrophic with a significantly noisier potential profile.

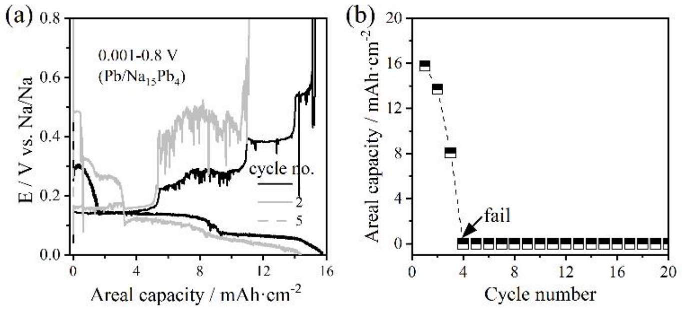

Figure 6.4 (a) The galvanostatic profiles of the Pb foil electrode during the 1st, 2nd and 5th cycles at 0.1 mA (12 mm electrode disk) with a potential range of 0.001–0.8 V. (b) The cycling performance of the Pb foil electrodes under the same charge-discharge conditions.

Identifying which phase transformations are largely responsible for the electrode failure and strategically eliminating their negative impact from the electrochemical cycling is essential to prolong the cycle life of Pb foil electrodes. Here we systematically explore the reversibility of each pair of phase transformations (both directions) by controlling the cutoff voltages during GCD cycling. Figure 6.5a-d shows the voltage profiles of Pb foil electrodes cycled within 0.4-0.8V, 0.15-0.45V, 0.09-0.35 V, and 0.001-0.2 V vs. Na / Na^+, aiming to examine Pb/$NaPb_3$, $NaPb_3$/NaPb, NaPb/Na_9Pb_4, Na_9Pb_4/$Na_{15}Pb_4$, respectively, in isolation. The electrodes after the initial cycle deliver the areal capacities of ~1.1 mAh·cm^{-2} (~33.6 mAh·g^{-1}), ~2.4 mAh·cm^{-2} (73.3 mAh·g^{-1}), ~4.8 mAh·cm^{-2} (146.6 mAh·g^{-1}), and ~7 mAh·cm^{-2} (213.8 mAh·g^{-1}) for these four pairs of phase transformations, respectively, which are in line with their theoretical capacities. In general, cycling stability should be reversely correlated to the depth of sodiation because a deeper sodiation induces higher volume change considering the initial geometry of the Pb foil. As anticipated, the cycling data of the first three phase transformations (i.e., Pb/$NaPb_3$/NaPb) agree with the trend described just before (Figure 6.5e). For instance, the electrode cycled within 0.4-0.8 V (largely Pb//$NaPb_3$) gives the best cycling performance, maintaining ~86% of its initial capacity after 130 cycles. Specifical attention should be paid to the last two pairs of phase transformations where the trend no longer stands. Cycling within 0.09-0.35 V (i.e., largely NaPb//Na_9Pb_4) shows the fastest capacity degradation: It can merely survive 3 cycles (same as full sodiation cycling in Figure 6.4) before its failure (i.e., 10% capacity retention). On the contrary, the electrode cycled between 0.001 and 0.2 V shows a better lifetime of approximately 12 cycles. These cycling tests of the electrode at the two cutoff voltages which were repeated a couple of times (Figures 6.6 and 6.7), can well support the unexpected trends. The poorer reversibility of 0.09-0.35 V cycling indicates that other factors in addition to the volume change also play a critical role in the phase transformations.

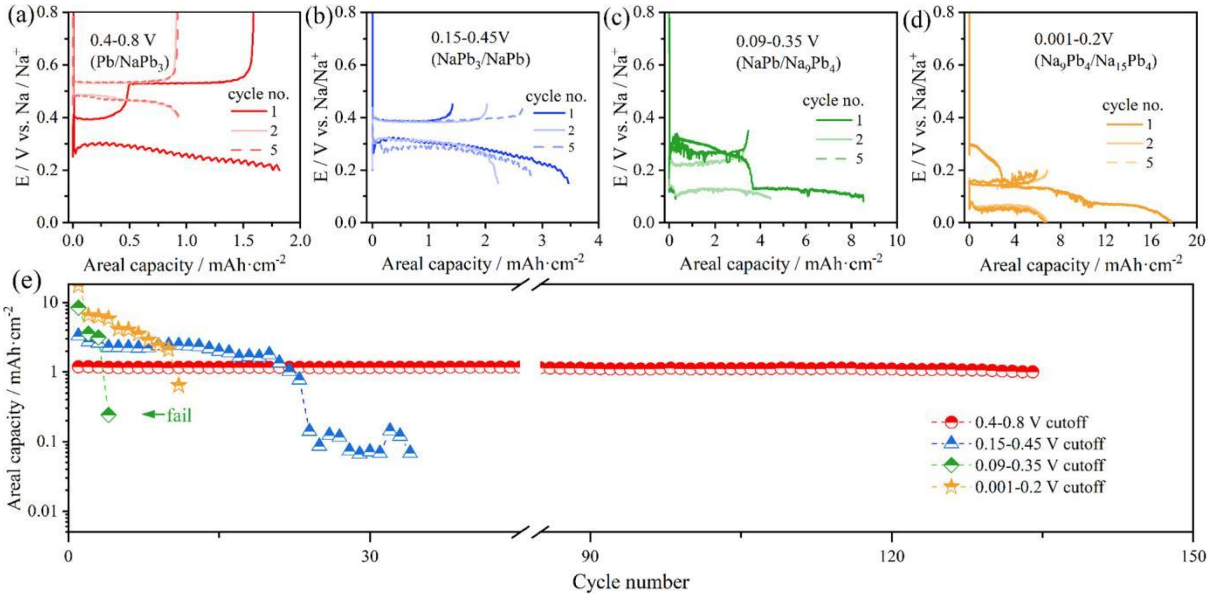

Figure 6.5 The galvanostatic profiles of the Pb foil electrode during the 1st, 2nd and 5th cycles, obtained from cycling at 0.1 mA with different voltage windows: (a) 0.4–0.8 V, (b) 0.15–0.45 V, (c) 0.09–0.35 V, (d) 0.001–0.2 V. (e) The capacity retention for the cycling within the same cutoff voltages.

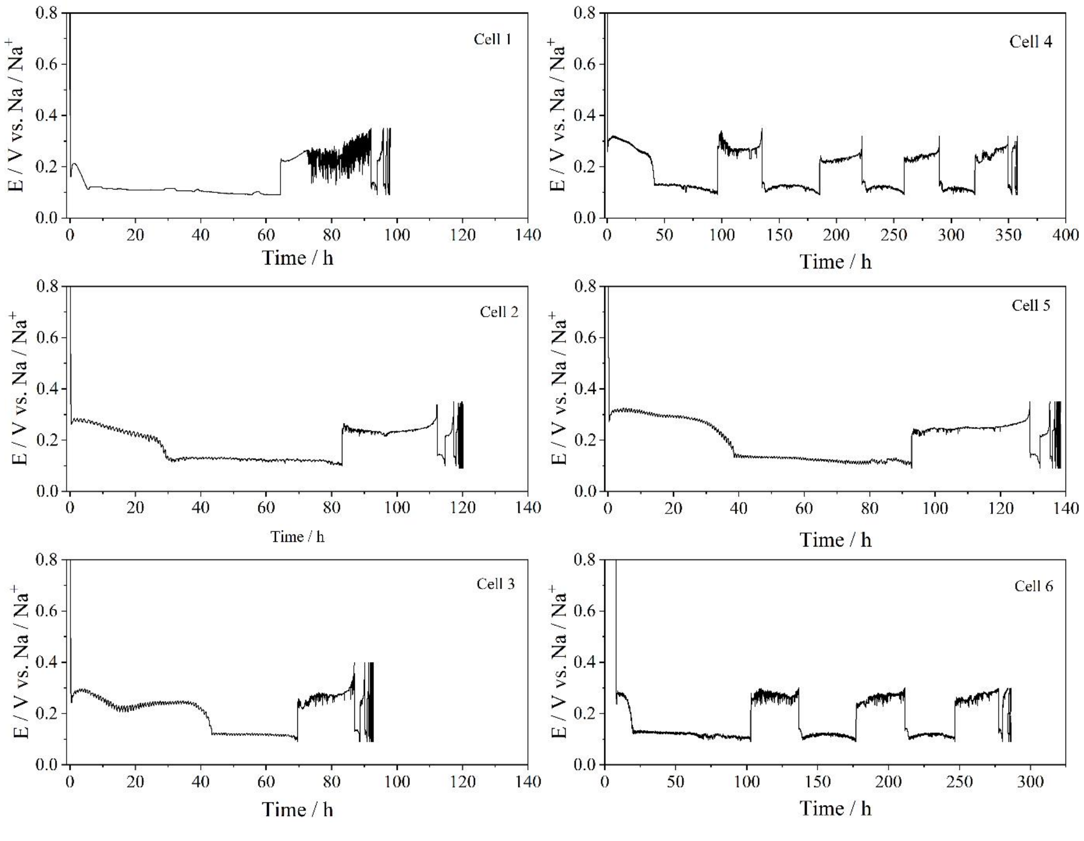

Figure 6.6 The full voltage profiles of Pb foil electrodes cycled between 0.09-0.35 V. The cells do not work after 2-4 cycles.

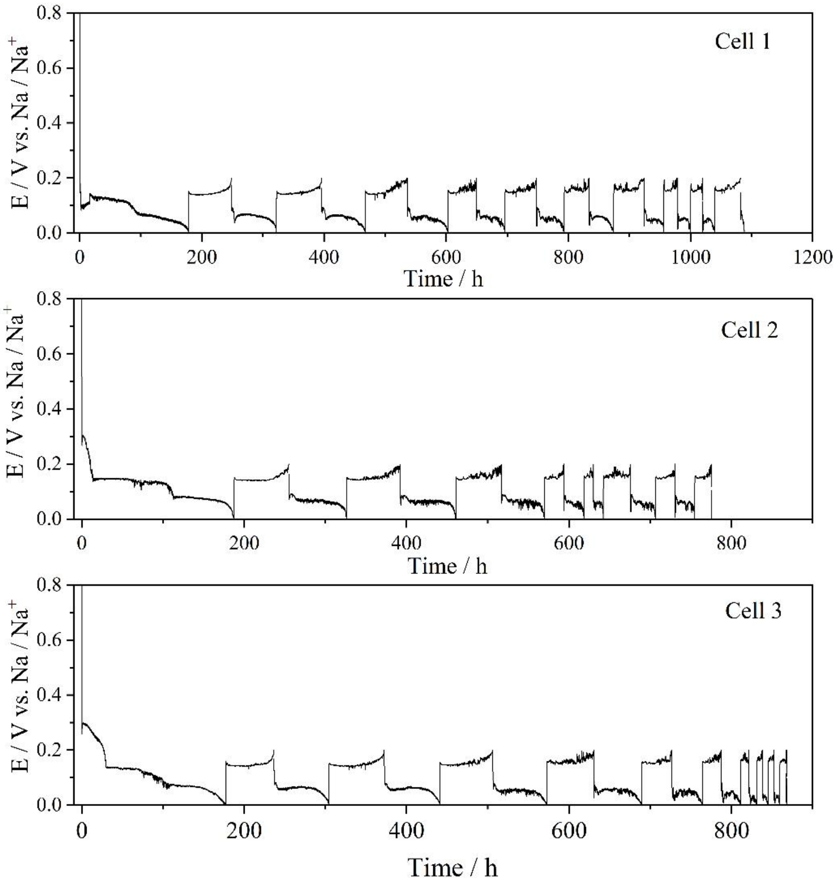

Figure 6.7 The full voltage profiles of Pb foil electrodes cycled between 0.001-0.2 V.

6.2.4 Microstructural Change during Different Transformations

SEM images (Figure 6.8) of the electrode after different cycles within the above-mentioned voltage windows may provide implications on why these phase transformations perform differently. In the case of 0.4-0.8 V, and 0.15-0.45 V, both electrode surfaces are relatively flat, and retain some trace of calendaring after 1st cycle (Figure 6.8a and 6.8b). Moreover, no evident electrode destruction is observed after 15 cycles in the above-mentioned two cases: No obvious cracks, voids, or pulverization. This structural stability can largely explain the better cycling stability of these two pairs of phase transformations. Differently, some signs of mechanical damage for the electrode are observed in the other two cycling scenarios with deeper sodiation, i.e., between 0.09-0.35 V and 0.001-0.2 V (Figure 6.c-6d). Particularly for the former case, many voids and small cracks seem to appear on the electrode surface after the 5th cycle (Figure 6.8c).

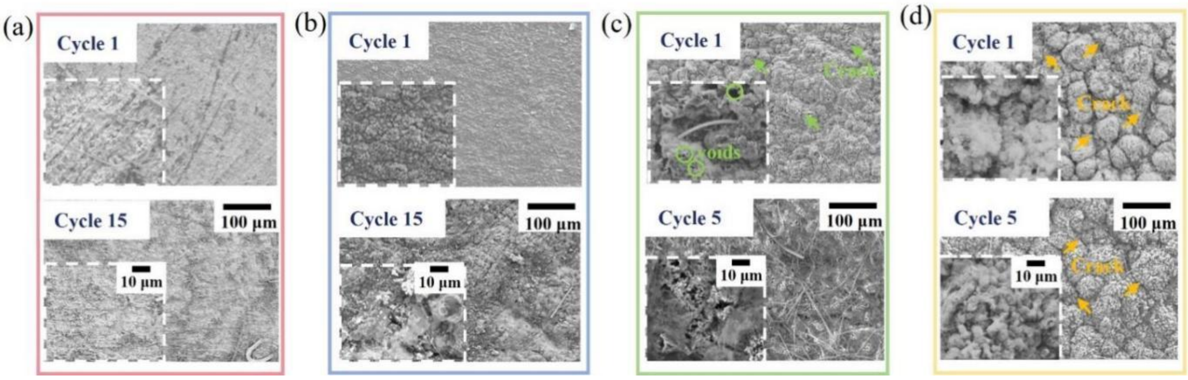

Figure 6.8 The surface SEM images of the Pb electrode after the 1st and 15th cycles at voltage windows of (a) 0.4-0.8V and (b) 0.15-0.45 V. The SEM images of the Pb electrode after the 1st and 5th cycles at voltage windows of (c) 0.09-0.35 V, (d) 0.001-0.2 V.

To further understand the poor reversibility of the NaPb/Na_9Pb_4 phase transformation, the morphological change of the electrode in 1st and 2nd cycling between 0.09-0.35 V vs. Na/Na^+ are characterized (Figure 6.9). The first sodiation to 0.09 V (Figure 6.9a) gives rise to some cracks on the protrusions, although the overall electrode integrity is maintained. After the subsequent desodiation to 0.35 V, the electrode surface exhibits porous and mossy features (circles in Figure 6.9b). Despite no study reporting the formation of the voids in the desodiated Pb, it seems not surprising since many alloy electrodes, e.g., Sn(-Li), Si(-Li), and Al(-Li), are reported to be porous after selective dealloying processes [148, 176, 177]. As the electrode is sodiated to 0.09 V for the second time, most voids remain (Figure 6.9c), which appear to become larger when desodiating to 0.35 V (Figure 6.9d). These physical damages could partly explain the poorest cyclability of the Pb foil electrode in the voltage range of 0.09-0.35 V.

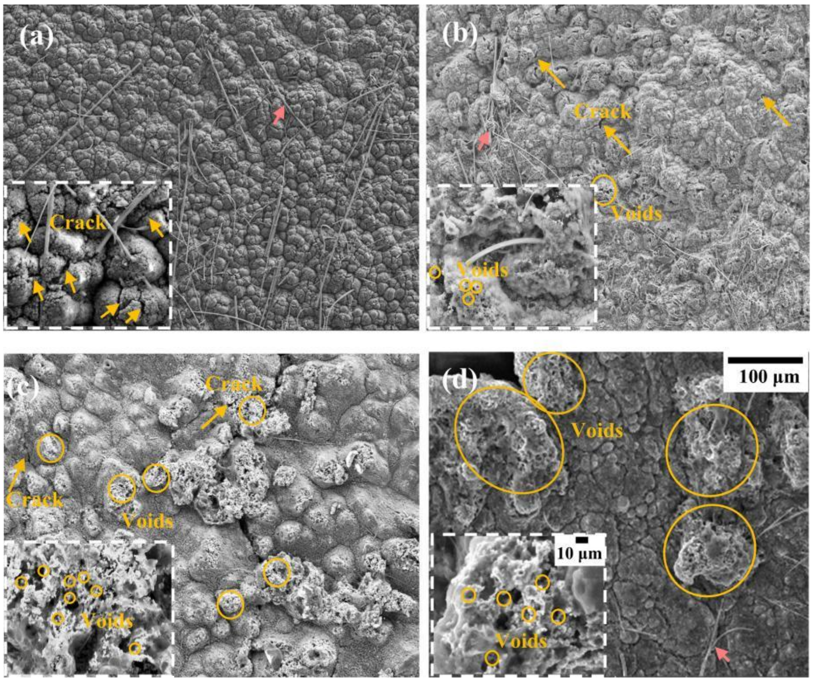

Figure 6.9 SEM images of the Pb foil electrodes at different states when limited to the problematic phase transformations: (a) 1st sodiation to 0.09 V, (b) 1st desodiated to 0.35 V, (c) 2nd sodiation to 0.09 V and (d) 2nd desodiation to 0.35 V. Cracks are denoted by yellow arrows while voids are denoted by yellow circles. The glass fibers remaining on the electrode surface are also marked by red arrows.

6.2.5 Cycling Performance Evaluation of Full Cells

Given the problematic transformations, the Pb electrode is suggested to be utilized by largely cycling Pb/$NaPb_3$ or Pb/NaPb, depending on the capacity contributed by the cathode. Stable long-term cycling is a prerequisite to the practical application of rechargeable batteries. Here we evaluate the cycling stability of the Pb foil electrode in a full cell configuration with $Na_3V_2(PO_4)_3$ (NVP) as the cathode. Noteworthy, to minimize the catalytic effect of Pb, a small amount of sodium is pre-stored in the Pb electrode surface layer (i.e., chemical presodiation), causing an open circuit voltage of ~2.4 V for the NVP//Pb full cells (vs ~ 0.6 V for the cell with the NVP cathode and a fresh Pb anode). The galvanostatic profiles of NVP//Pb, Pb//Na, and NVP//Pb, are provided in Figure 6.10a, of which the NVP//Pb full cell is characterized to have two flat and long plateaus at ~3.2 and ~2.9 V for charge and discharge, respectively. Figure 6.10b shows the 1st, 5th, 50th, 100th, 200th, and 300th GCD curves of the NVP//Pb full cell within the voltage range of 2.2-3.6 V vs. Na/Na^+ at 0.15 $A\cdot g_{-NVP}^{-1}$ (~0.15 $mA\cdot cm^{-2}$). Furthermore, the cycling performance of the NVP//Pb full cell (Figure 6.10c) displays that at 0.15 $A\cdot g_{-NVP}^{-1}$ the reversible capacity of the cells gradually goes down to ~65 $mAh\cdot g_{-NVP}^{-1}$ after 300 cycles, corresponding to approximately 60% of the initial capacity.

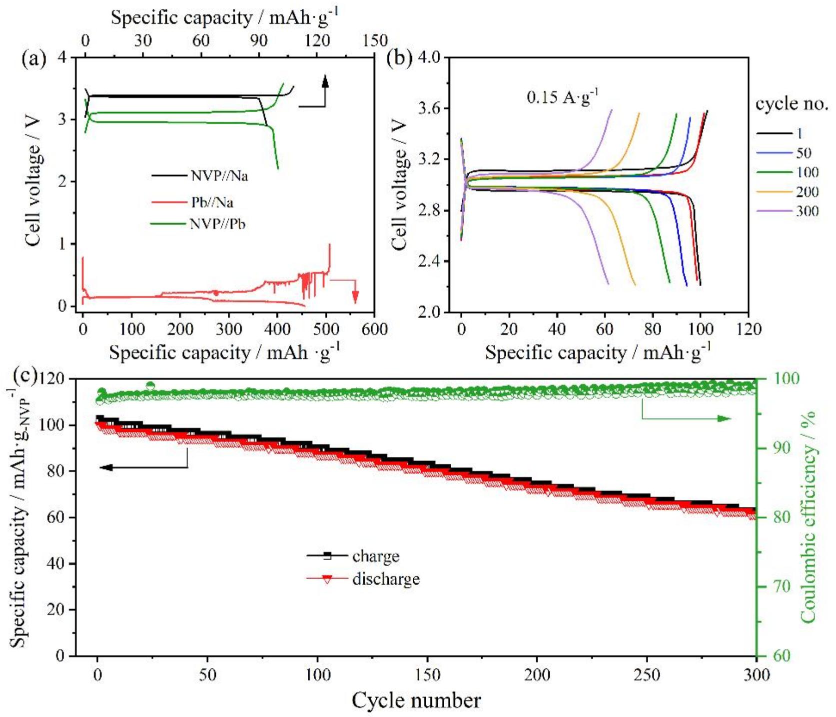

Figure 6.10 (a) The initial GCD curves of a Pb//Na half-cell, an NVP//Na half-cell, and a NVP//Pb full cell cycled at 0.1 mA (0.15 $A \cdot g_{\text{-NVP}}^{-1}$). (b) The 1st, 5th, 50th, 100th, 200th and 300th galvanostatic profiles and (c) the long-term cycling performance of NVP//Pb full cells at 0.15 $A \cdot g_{\text{-NVP}}^{-1}$.

6.3 Discussion

6.3.1 Situation of Pb (Sn) Electrode

While Pb is generally not considered to be a competitor in the search for suitable SIB anodes due to its toxicity and only limited research has been reported regarding Pb-based materials since the first exploration in 1987, there remains questionable whether Pb electrodes should be abandoned. Till now, though Pb is toxic, Pb-acid batteries (PABs) are the most commonly reported battery system and still dominate the global energy storage markets (e.g., ~70% market occupied by PABs in 2018 [10]). For the grid-scale field, the rapid development of LIBs in past decades makes them quite competitive in emerging large-scale energy storage applications[34], while PABs have still been the most well-adapted choice for medium to large-scale energy storage systems. However, both technologies are facing their bottlenecks with the relatively low energy density of the former and the uneven Li source distribution of the latter. This situation seems to offer an opportunity for low-cost SIBs, particularly with cheap and abundant materials as electrodes (such as Pb) for large-scale energy storage practices. In addition to the application promise, the previously reported encouraging electrochemical results of Pb composite electrodes [97], e.g., high capacity retention of ~83% after hundreds of cycles [172] and a lifespan of >1000 cycles at ~1 mA [171], seems to further demonstrate the feasibility of Pb as SIB electrodes. Overall, Pb, with appropriate recycling, might be a practical SIB electrode and worthy of further investigation. Nevertheless, even though the cycle stability of Pb electrodes was partly improved by using micro-sized Pb particles and suitable electrolytes to some extent over the past years [97, 171], the cycle life and coulombic efficiency are not sufficient for the commercialization application. Additionally, there is a lack of understanding of the critical factors determining the cycling stability of Pb electrodes.

Differently, Sn, the upper neighbor of Pb, has been widely investigated as an SIB electrode over the past decades. It is anticipated that the knowledge accumulated by Sn could partly shed light on the electrochemical sodiation of Pb. On the one hand, both Sn and Pb are low-melting point metals with similar electrical resistivity (115 $n\Omega \cdot cm^{-2}$ for Sn vs. 208 $n\Omega \cdot cm^{-2}$ for Pb), mechanical hardness (Mohs hardness: 1.5 for Sn and Pb) [178]. On the other hand, the sodiation of Pb is analogous to that of Sn, by successively forming $NaSn_3$($NaPb_3$), NaSn(NaPb), Na_9Sn_4(Na_9Pb_4), and $Na_{15}Sn_4$($Na_{15}Pb_4$) [93, 159]. Further, the sodiated Na_xPb and Na_xSn phases with the same stoichiometry also have the same crystal structure and show analogous trends in the change of electrical resistivity and mechanical property with the increasing Na content. Namely, the Na inclusion is predicted to result in a significant elastic softening for the Na-Sn (or Na-Pb) electrode [105], and the Na-richer Na-Pb intermetallic phases are more resistive than the Na-poor ones at elevated temperatures, in line with the reported higher resistivity of NaSn than Sn [179]. Given these physio-chemical similarities, it is therefore hoped that the dominant factor determining the capacity fade for different phase transformations of Pb electrodes in this study could benefit from the established understanding of the Sn electrode through analogous reasoning.

6.3.2 Clarification of Na-Pb Phases during Sodiation

Here our electrochemical results are integrated with the published Na-Pb phase diagram to clarify the intermetallic phases during the sodiation. From Figure 6.11, in general, the intermetallic Na-Pb phases detected by XRD largely agree with the binary phase diagram [79] but the simultaneous formation is suggested instead of sequential, explaining why the single-phase region (i.e., #7) does not solely exhibit the diffraction peaks that correspond to the specific phase.

Upon the initial sodiation (the shaded region near the origin in Figure 6.11), the Pb electrode is probably saturated with Na to form a solid solution with the maximum Na content of ~2 at% at room temperature while maintaining the original crystal structure, although the electrolyte breakdown and sodiation of the thick surface Pb oxides should not be neglected. However, the Pb(Na) solid solution should be limited to a very thin layer on the electrode surface considering that Na diffusion is extra slow in pristine Pb foil (including Pb oxides), i.e., $\sim 10^{-13}$ $cm^2 \cdot s^{-1}$ [109]. As the sodiation continues, Na atoms keep accumulating on the electrode surface until the nucleation of the new $NaPb_3$ phase (the potential dip highlighted by an arrow in Figure 6.11).

Although the endpoint of the first potential plateau (#3 in Figure 6.11) is located around the $NaPb_3$ region, the XRD results do not seem consistent (#3 in Figure 6.1b). This mismatch is acknowledged by the inhomogeneous nucleation of Na-Pb phases, which is often observed in alloy electrodes in Li- and Na-based systems [180-182]. It is reported that subsequent phase transformations tend to occur along certain crystal planes or orientations in alloy electrodes [183-186]. Furthermore, the sluggish kinetics (i.e., the slow Na diffusion in Pb) are suggested to be responsible, such that over-sodiation may occur at the positions (e.g., phase boundaries, dislocations, etc.) that are accidentally not hit by the X-ray. It should be noted that the β phase (i.e., 28 at% to 35 at% Na) indicated by the phase diagram published in 1968 [187] is not observed electrochemically, nor in the previous reports [79, 97], thereby is intentionally excluded from Figure 6.11.

On the first half of the second sodiation plateau (#4 of Figure 6.11) where a coexistence of $NaPb_3$ and NaPb is expected, the diffraction peaks corresponding to $NaPb_3$ are detected. The lattice parameters of the $NaPb_3$ phase are refined from the XRD results to be $a=b=c=0.488$ nm, consistent with the reported ones [97], further supporting that $NaPb_3$ is the first sodiation phase other than the β phase presented in the phase diagram [79]. This long potential plateau terminates with the stoichiometry of Na_9Pb_4 (#5 in Figure 6.11), where all the diffraction peaks referring to $NaPb_3$/NaPb/Na_9Pb_4 are observed. The simultaneous phase formation may be caused by the different kinetical behaviors of each phase, akin to the sodiation of Ge [188], but specific investigations are required to further quantify to what extent this is happening. As indicated by the phase diagram, the presence of Na_5Pb_2 remains debatable. An early study claimed that Na_5Pb_2 is formed by melting Na and Pb with identical atomic ratios but without the support of XRD results [172]. On the contrary, Ellis et al. and Derwiche et al. confirmed the presence of Na_9Pb_4, instead of Na_5Pb_2, after sodiating a Pb electrode by in situ XRD technique [79, 97]. Given that the literature of Pb anode remains largely limited, we try to shed light on the formation of Na_5Pb_2 by discussing the analogical Na_5Sn_2, which is reported to be metastable, and its formation seems to be suppressed electrochemically [94].

The last potential plateau ends at a point where the atomic ratio of Na/Pb calculated from electrochemical data nicely agrees with that presented in the phase diagram. However, some stubborn Pb regions are not fully sodiated to reach the $Na_{15}Pb_4$ phase, as indicated by the X-ray diffractogram (#7 in Figure 6.1b). The incomplete sodiation of these regions may be restricted by the huge mechanical strain caused by the volume expansion that compresses the neighboring grains, subsequently shifting the sodiation potential towards a lower level, even below 0 V [189]. This explanation can be evidenced by the minor peak shift of the Pb phase toward a higher 2θ degree in the diffractogram (gray dashed line in Figure 6.1c), which is characteristic of significant mechanical strain. Similar observations were also reported in other alloy electrodes, such as Al and Sn, in Li-based systems [159].

To summarize, from our XRD results of the simultaneous formation of multiple phases, the electrochemistry on Pb foil electrodes suggests that the overall electrode equilibrium during the initial cycle should be described as:

$$Pb \xleftrightarrow{Na} NaPb_3(NaPb,\ Na_9Pb_4,\ Na_{15}Pb_4)$$

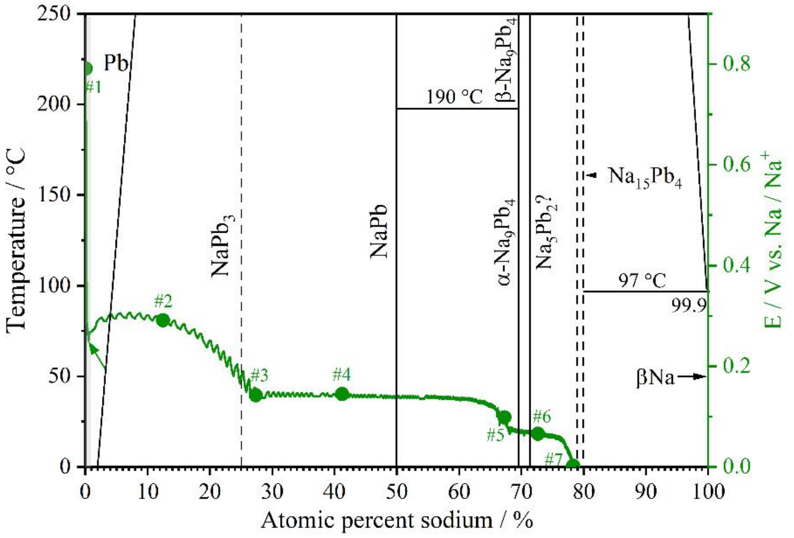

Figure 6.11 The initial discharge curve of Pb foil electrodes integrated with the Na-Pb phase diagram. It is noted that the highlighted dots here are consistent with those in Figure 6.1a.

6.3.3. Impact of Crystal Structures on Electrode Reversibility

The sodiation of Pb induces a significant crystal rearrangement by forming multiple Na-Pb intermetallic phases, i.e., cubic $NaPb_3$, tetragonal NaPb, orthorhombic Na_9Pb_4, and cubic $Na_{15}Pb_4$. The different lattice parameters, which are summarized in Table 6.1, can give rise to a change in unit cell volume and atomic interactions, thereby affecting the reversibility of these phase transformations.

The unit cell volumes of these phases are distinctively different due to Na incorporation. It is common that the shallower the sodiation/lithiation (i.e., less volume expansion), the better the reversibility is, which seems to hold true for the Na-Pb system as well. However, we have already noted that the NaPb/Na_9Pb_4 and the Na_9Pb_4/$Na_{15}Pb_4$ transformation do not follow the trend. The former undergoes a lattice volume expansion of ~115.3%, smaller than that of the latter (~142.1%) but exhibits worse reversibility (Figure 6.5). This observation suggests that other factors either caused by or independent from the volume change are also governing the reversibility of the phase transformations. For instance, it is known that significant mechanical stresses can accumulate near the phase boundaries where the lattice mismatch is more pronounced [190]. This interpretation is consistent with the observation of the stubborn unsodiated regions discussed previously. As soon as the stress is too large to be accommodated, mechanical failures are expected at the phase interface, leading to electrode degradation.

Table 6.1 The structural information of multiple Na-Pb intermetallic phases

Na-Pb Phase	Crystal structure	Lattice parameters			Calculated volume expansion	Relative volume expansion from the prior phase	Pb-Pb bond length (nm)	Na-Pb bond length (nm)
		a (nm)	*b* (nm)	*c* (nm)				
Pb	Cubic	0.4950	0.4950	0.4950	/	/	0.3130	/
$NaPb_3$[97]	Cubic	0.4873	0.4873	0.4873	~26.0 %	~26.0 %	0.3100	0.3469
NaPb[97]	Tetragonal	1.0580	1.0580	1.7740	~100.6 %	~73.4 %	0.3148	0.3550
Na_9Pb_4[79]	Orthorhombic	0.5471	0.945	3.0356	~215.9 %	~115.3 %	0.3141 or 0.2428	0.3000
$Na_{15}Pb_4$[97]	Cubic	1.3316	1.3316	1.3316	~358.0 %	142.1 %	/	0.3265

Note: The volume expansion and bond length are calculated based on the lattice parameters of the Na-Pb phases.

Different atomic interactions are expected in each Na-Pb intermetallic phase due to the differences in the Pb-Pb (~0.313 nm in Pb) and the Na-Na (~0.364 nm in Na) bonds. The Pb-Pb bonds in pristine Pb exhibit weakly covalent characteristics: Four valence electrons of the Pb atom are shared with those of the neighboring ones to form the chemical bonds. The electronic structure and the smaller length make the Pb-Pb bonds quite strong. As Na is incorporated into Pb, the Pb atoms will be gradually surrounded by Na atoms, and thereby the Pb-Pb bonds will be replaced by the newly formed Na-Pb bonds. As we can see from Table 6.1, the substitution of shorter Pb-Pb bonds by Na-Pb bonds with larger bond lengths (i.e., roughly 0.3469 nm in $NaPb_3$ and 0.3550 nm for NaPb) could induce an elastic softening in Na-Pb upon the transformation from Pb to NaPb, indicating lower stiffness for both $NaPb_3$ and NaPb than Pb. However, further Na inclusion can cause stronger interatomic interaction, indicated by shorter Na-Pb bond lengths of Na_9Pb_4 (0.3000 nm) and $Na_{15}Pb_4$ (0.3265 nm). Consequently, the stiffness of both phases should be higher than that of $NaPb_3$, which can partly explain why the reversibility of NaPb/Na_9Pb_4 and Na_9Pb_4/$Na_{15}Pb_4$ is worse than that of Pb/$NaPb_3$ and $NaPb_3$/NaPb.

6.3.4 Impact of Mechanical Properties on Electrode Reversibility

It is well-adopted that mechanical properties (e.g., ductility or brittleness) should also play critical roles in the reversibility of the transformations of Pb electrodes, especially since the stiffness has been briefly discussed above.

The mechanical properties of each Na-Pb phase vary, evidenced by the DFT-calculated elastic, bulk, and shear moduli [105], which are also summarized in Table 6.2. The ductility of each phase can be estimated by the ratio of bulk to shear modulus (B/G). It is found that Pb and $NaPb_3$ are relatively ductile, as indicated by higher B/G ratios of 3.19 and 3.90 respectively, whereas the higher-ordered Na-Pb phases (e.g., NaPb, $Na_{15}Pb_4$) tend to become more brittle, supported by the low B/G ratios (<2). Noteworthy, these mechanical moduli of the Na_9Pb_4 phase are absent, it is proposed that the Na-Sn system (e.g., Na_9Sn_4) may be used to shed light on the Na_9Pb_4 phase considering the similarity and the analogous nature of Na-Pb with Na-Sn alloys in physio-mechanical properties [105]. Also, the B/G ratio of the Na_9Pb_4 phase should not be distinctively different from that of NaPb or $Na_{15}Pb_4$, although requiring further confirmation. As a result, for the Pb/$NaPb_3$ and $NaPb_3$/NaPb transformations, the ductile Pb and $NaPb_3$ can act as a buffer to accommodate the (de-)sodiation-induced mechanical stress by plastically deforming Pb or $NaPb_3$, thereby preventing the possible crack formation and enabling a long cycle life. In contrast, the NaPb/Na_9Pb_4/$Na_{15}Pb_4$ transformations may be more susceptible to cracking due to the higher brittleness of these phases, let alone their volume changes are more pronounced than those of Pb/$NaPb_3$/NaPb. This interpretation is evidenced by the SEM observation of the electrode surface with no obvious crack or other mechanical damage (e.g., pulverization, loss of electrical contact, etc.) after 15 cycles when the electrode is limited to the Pb/$NaPb_3$/NaPb transformations (Figure 6.8a-b). On the contrary, obvious cracks and voids on the electrode surface are observed in (Figure 6.9, and Figure 6.8c-d) during the cycling among NaPb/Na_9Pb_4/$Na_{15}Pb_4$. The crack and void formation on the electrode surface exposes the fresh Pb underneath to the electrolyte, facilitating secondary SEI formation and causing cyclic irreversible Na consumption, and thereby giving poor electrode reversibility.

Table 6.2 The mechanical, electrical, and electrochemical properties of Na-Pb phases

Metal	Elastic modulus (E)[105]	Bulk Modulus (B)[105]	Shear Modulus (G)[105]	B/G[105]	Electrical resistivity at 723K / (Ohm·m)[103, 179]	Na diffusivity in M or Na-M/($cm^2 \cdot s^{-1}$)
Pb	35.45	41.68	13.06	3.19	~1.00	$\sim 10^{-16}$[109]
$NaPb_3$	23.23	32.94	8.43	3.90	~1.50	/
NaPb	24.54	15.04	9.99	1.50	~2.20	$\sim 5 \times 10^{-17}$[191]
Na_9Pb_4	N/A	N/A	N/A	N/A	~3.30	/
$Na_{15}Pb_4$	17.14	13.14	6.68	1.96	~4.00	$\sim 1 \times 10^{-17}$[191]

6.3.5 Impact of Electrical Resistivity on Electrode Reversibility

In electrochemical systems like SIBs, electrical conductivity directly affects electron migration. The different electrical resistivities of each Na-Pb phase may also partly explain their different reversibility.

To date, while no experimental data can be found regarding how the Na incorporation influences the electrical conductivity of the sodiated Pb at ambient temperature, one theoretical study recently predicts an increased resistivity of NaPb Zintl phase in contrast to the unsodiated Pb, which may negatively affect the electrochemical performance of the Pb@PbO-C composite electrode [100]. Moreover, an early study reported that the electrical resistivity of Na-Pb alloy goes up apparently with the increased Na content till ~80 at.% Na content at 723 K (Table 6.2) [179]. Like Pb, the Sn electrode is found to be more resistive during sodiation at room temperature: a remarkable increase in the electrical resistivity by 6-8 orders of magnitude is observed by the transformation of pristine Sn to the NaSn phase. The higher overall impedance hinders the Na insertion(extraction) into(out from) the Na-Sn electrode, resulting in capacity loss [157], which may hold true for the analogous Na-Pb system.

On top of the intrinsic electrical conductivity, the lattice volume change and mechanical stress/damage discussed above could aggravate the negative impact of electrical conductivity on the electrode reversibility. It was reported that the stressed NaSn exhibits an electrical resistivity that is 2-3 orders of magnitude higher than the stress-free one [149]. Back to Pb, the mechanical stress induced by the volume change of the NaPb/Na_9Pb_4/$Na_{15}Pb_4$ transformations is larger than that of Pb/$NaPb_3$/NaPb ones. As a result, the increase in resistivity due to stress for the former case is likely larger than the latter one. On the other hand, the mechanical damage, e.g., cracks and voids (Figure 6.8c-d) is accompanied by the local electric disconnections, giving a higher electrical resistivity. The growth of secondary SEI, which is non-conductive, will also lead to a deterioration in electrical conductivity.

6.3.6 The Impact of Diffusion Kinetics on Electrode Reversibility

The Na diffusion kinetics seem to play an important role in the cycling stability of Pb electrodes since the XRD results suggest that a small amount of Na is trapped in the Na-Pb electrode that is desodiated to 0.8 V vs. Na/Na^+ (#11 in Figure 6.1b). While the Na trapping behaviors are rarely reported for Pb anode, rich literature can be found on the well-established Li-based chemistries where Li trapping is commonly ascribed to sluggish diffusion kinetics [192]. The diffusion-controlled Li trapping would give rise to the loss of active Li, thus leading to capacity degradation over cycling [193]. In the case of Pb electrodes, the trapped Na may also be associated with the different kinetic behaviors of different Na-Pb intermetallic phases. It should be noted that the kinetic limitations might be more pronounced in the metallic Pb foils than in their composite counterparts [79].

The kinetic behaviors of the Na-Pb intermetallic phases remain poorly understood, with only three Na diffusivity values being calculated (Table 6.2). The SEM images (Figure 6.9) may be used to shed light on the sodium diffusivity in Na-rich Na-Pb phases. Considerable voids in the electrode (Figure 6.9) after the desodiation when limited to the NaPb/Na_9Pb_4 transformations, in contrast to no obvious voids for the Na_9Pb_4/$Na_{15}Pb_4$ (Figure 6.8d). The void formation is a well-known phenomenon in the interdiffusion process of metal alloy compounds since the dealloying strategy has been widely used to produce nanoporous alloy materials [194]. Meanwhile, many studies also reported the formation of pores in alloy electrodes in the desodiation or delithiation process, including Sn [176], Al [148], Si [195], and Ge [196]. It is generally considered that the voids and/or pores formation is a result of fast delithiation or desodiation kinetics [195]. The discussion seems contradictory to the theoretically calculated Na diffusivity of ~10^{-16} $cm^2 \cdot s^{-1}$ in $Na_{15}Pb_4$, around 1 order of magnitude slower than that in pristine Pb. In any case, systematic investigations using robust techniques,or advanced instruments are needed to extract reliable Na diffusivities in these Na-Pb phases.

6.3.7 Strategic Utilization of Pb Foil Electrodes

Given the poorest reversibility of NaPb/Na_9Pb_4, it is reasonable to strategically eliminate this problematic phase transformation by controlling the cutoff voltage from the electrochemical reactions of Pb anodes to prolong the cycle life and enable its utilization. This idea is further verified by the improved cycling performance of the Pb foil anode cycling within 0.15-0.8 V vs. Na/Na^+ (Figure 6.12**)** compared to the case of full sodiation-desodiation. To be specific, the Pb foil electrode delivers a reversible capacity of ~2.9 $mAh \cdot cm^{-2}$ after 20 cycles, corresponding to ~85% of the initial desodiation capacity.

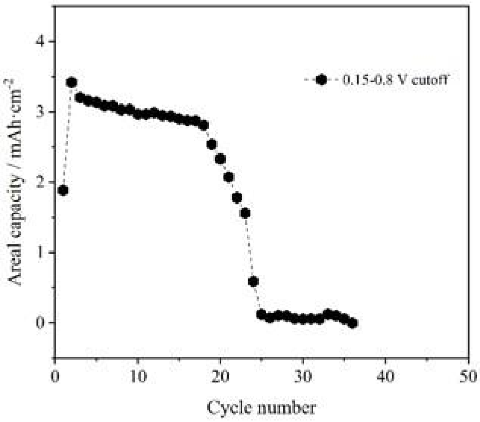

Figure 6.12 Cycling performance of Pb//Na half cells strategically cycled within 0.15-0.8 V at 0.1 mA.

The suitability of Pb foil as an SIB anode is evaluated by considering practical application in terms of energy density. Figure 6.13a shows the Ragone plot of Na-ion cells with the Pb foil anode and other typical anodes (i.e., HC [197-199], Sn [198, 200], Sb@TiO_2 [201], Sb@CNT [202], and graphite [203]). It is noted that the gravimetric energy density here is all normalized to the weight of the cell stack, including the cathode, anode, separator, electrolyte, and current collector. The detailed parameters for the energy density calculation of the cells with $NaMn_{0.44}O_2$ cathode and 30 μm Pb foil anode (abbreviated as NMO//30Pb) are shown in Table 6.3. From Figure 6.13a, one can see that the reported gravimetric energy data of the Na-ion cells ranges between 2-70 $Wh \cdot kg^{-1}$, most of which are higher than that of PABs (green zone, 30-40 $Wh \cdot kg^{-1}$ [204]), highlighting the competitiveness of SIBs over Pb-acid batteries in energy density. The NMO//30Pb cell stands between these reported results, delivering a gravimetric energy density of approximately 35 $Wh \cdot kg^{-1}$ (red star in Figure 6.13a), slightly higher than PABs though lower than the present SIBs level (e.g., ~90-140 $Wh \cdot kg^{-1}$ (cell-level energy) [205]). This superiority of the Pb foil electrode in energy density is more pronounced when looking at the much higher volumetric energy density of the NMO//30Pb from Figure 6.14, ~170 Wh·L^{-1}, than that of PABs. Notably, the NMO areal capacity is 0.9 mAh·cm^{-2}, much lower than the areal capacity requirement for the commercial battery (~2-3 mAh·cm^{-2} per side) [206]. To better evaluate the future potential of Pb foil, the typical O3 and P2 type cathodes with an areal capacity of around 3 mAh·cm^{-2} are used for the energy density recalculation. Figures 6.13b and c present the extrapolated gravimetric and volumetric energy density at stack level for different Na-ion cells with Pb foil anode and other typical anodes (i.e., hard carbon (HC), Sn/C, Sb/C, P/C, and $Na_2Ti_3O_7$ (NTO)). The simplified stack structures of the cells are shown in Figure 6.13d and the detailed parameters of the cell components for the energy density calculation are given in Table 6.4 [207]. While the cells with 30 μm-thick Pb foil anodes in this work exhibit a higher gravimetric energy density than the one with NTO anodes, the value is found to be roughly 20-30% lower than the other cells with hard carbon or alloy anodes (Figure 6.13b). Intriguingly, the Pb foil anodes are more competitive in terms of volumetric energy density. As illustrated in Figure 6.13c, the cells with Pb foil electrodes display the highest volumetric energy density (roughly 700 Wh·L^{-1}) among all the cells including those with Sn or Sb alloys anodes, which are regarded as the promising high-volumetric capacity anodes for SIBs. However, it is worth mentioning that the ratio of Pb foil (30 μm-thick) anode to cathode capacity is ~5.22, much higher than the normal level of N/P ratio (1.1-1.2) in commercial batteries [206]. For a better comparison, a 6 μm-thick Pb foil, which gives a more realistic N-to-P ratio (~1.09) is used to recalculate the energy density. By doing so, the superiority of the Pb foil anode becomes evident: Both the gravimetric (~180 Wh·Kg^{-1}) and the volumetric energy density (850 Wh·L^{-1}) are the highest among all the cells presented in Figures 6.13b and c. In this regard, Pb seems to be a feasible SIB electrode candidate and worth our further investigation, especially taking the low cost and abundance of Pb into account.

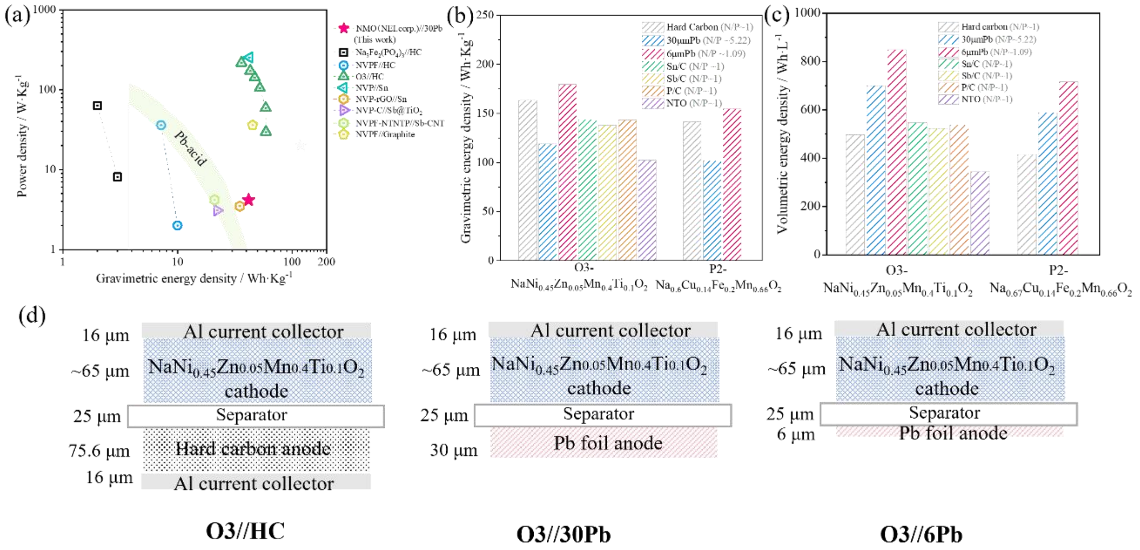

Figure 6.13 (a) The gravimetric Ragone plot of the Na-ion full cells with 30 μm-thick Pb foil anode in comparison with the recently reported Na-ion cells. It is noted that the PABs energy density given here (green region) is based on the whole cell weight while other data are all based on the weight of the stack (including cathode, anode, current collector, separator, and electrolyte). (b) The calculated gravimetric and (c) volumetric energy density comparison for different Na-ion full cells with Pb foil and other typical anodes. Detailed information for the cell components is given in Table 6.4. (d) The stack configurations for the energy density calculations.

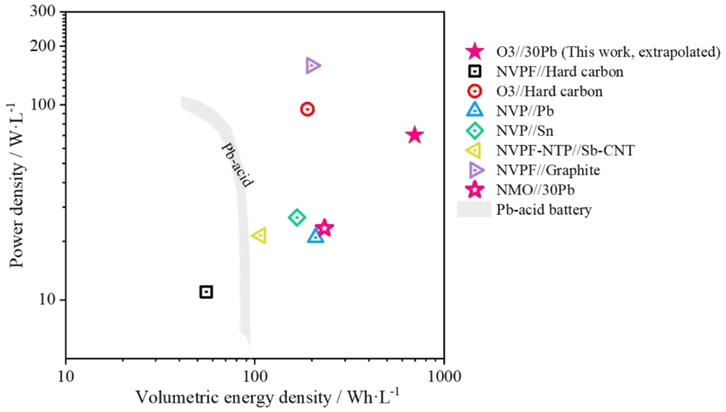

Figure 6.14 Volumetric Ragone plots of Pb foil compared to other typical anodes in Na-ion batteries.

Table 6.3 Parameters for the stack-level energy density calculation of NMO//30Pb full cells

NMO// 30Pb full cell		
Positive electrode ($NaMn_{0.44}O_2$)	Areal capacity	0.9 mAh·cm^{-2}
	Cathode thickness/weight	72 µm / 9.72 mg
	Al foil thickness /weight	16 µm / 4.88 mg
Separator (Celgard)		25 µm / 3.8 mg
Electrolyte		~23.53 mg
Negative electrode(Pb)	Areal capacity	~15.7 mAh·cm^{-2}
	Anode thickness/weight	30 µm / 38 mg
Total stack thickness		143 µm
Total stack weight		79.93 mg
Average voltage		~2.7 V
Cell areal capacity		0.9 mAh·cm^{-2}
Volumetric energy density		~170 Wh·L^{-1}
Gravimetric energy density		~35 Wh·kg^{-1}

Table 6.4 Detailed parameters of the full Na-ion cells for the stack-level gravimetric and volumetric energy density calculations. Two kinds of cathodes with 65 μm-thick active material, namely O3-$NaNi_{0.45}Zn_{0.05}Mn_{0.4}Ti_{0.1}O_2$ (O3) and P2-$Na_{0.67}Cu_{0.14}Fe_{0.2}Mn_{0.66}O_2$ (P2) are used, with the areal capacity of approximately 3 mAh·cm^{-2}. These data are referred to literature [207].

Cathode		Anode		Separator weight (mg) / thickness (μm)	Electrolyte weight (mg)	Current collector	Average Voltage (V)	Areal capacity/ mAh·cm^{-2}	Stack weight (mg) / thickness (μm)	**Gravimetric energy density** (Wh·kg^{-1})	**Volumetric energy density** (Wh·L^{-1})
Active materials	Thickness (μm) / weight (mg)	Active materials	Thickness (μm) /weight (mg), diameter 12 μm disks								
O3	65/20.13mg	Hard carbon	75.6/10.77	~3.8 /25	~23.53	2 Al (16 μm/4.88 mg)	~3.2	3.07	67.99/197.6	163.33	497.16
O3	65/20.13mg	Pb foil	30/38			1 Al (16 μm/4.88 mg)	~3.1	3.07	90.34/136	119.08	699.78
O3	65/20.13mg	Pb foil	6/7.6			1 Al (16 μm/4.88 mg)	~3.1	3.07	59.86/112	179.66	849.7
O3	65/20.13mg	Sn/C	23.8/5.5			2 Al (16 μm/4.88 mg)	~2.6	3.07	62.72/145.80	143.86	547.5
O3	65/20.13mg	Sb/C	30.7/8.08				~2.6	3.07	65.30/152.70	138.17	522.7
O3	65/20.13mg	P/C	20.4/3.32				~2.5	3.07	60.54/142.40	143.31	539
O3	65/20.13mg	NTO	83.1/20.66				~2.3	3.07	77.88/205.10	102.5	344.3
P2	65/18.8mg	Hard carbon	79.3/10.77			2 Al (16 μm/4.88 mg)	~2.6	3.21	66.66/201.30	141.53	414.6
P2	65/18.8mg	Pb foil	30/38			1 Al (16 μm/4.88 mg)	~2.5	3.21	89.01/136	102	590.01
P2	65/18.8mg	Pb foil	6/7.6			1 Al (16 μm/4.88 mg)	~2.5	3.21	58.61/112	154.78	716.5

Calculations for the gravimetric (E_G) and volumetric (E_V) energy density at stack level:

$$E_G(Wh{\cdot}kg^{-1}) = \frac{Capacity \times Average\ \ potential}{Weight\ \ of\ \ stack\ (cat\,hode + anode + electrolyt\,e + separator\ + current\ co\,llector)}$$

$$E_V(Wh{\cdot}L^{-1}) = \frac{Capacity \times Average\ \ potential}{Volume\ \ of\ \ stack\ (cat\,hode + anode + electrolyt\,e + separator\ + current\ co\,llector)}$$

6.4 Conclusion

The Pb foil electrode exhibits an initial specific capacity of ~480 mAh·g^{-1} (areal capacity of ~16 mAh·cm^{-2}) at 0.1 mA but stop functioning after only 3-4 cycles. The XRD tests support the formation of the four Na-Pb intermetallic phases during sodiation, namely $NaPb_3$, NaPb, Na_9Pb_4, and $Na_{15}Pb_4$. It is found that some stubborn Pb regions are not sodiated even after the deep sodiation to 0.001 V vs. Na/Na$^+$, while Na trapping is observed in the Na-Pb electrode after desodiating to 0.8 V vs. Na/Na$^+$, perhaps due to the sluggish kinetics and/or complex microstructures. The SEM observations show that electrode morphology changes dramatically during electrochemical cycling. The surface morphology of the Pb foil is found to be more catastrophically evolving with a higher Na content during the initial sodiation while Na extraction seems to result in the formation of cracks, voids, and mossy structure, largely explaining the fast capacity fading. To understand which phase transformation makes a greater contribution to capacity fade, the reversibility of each pair of phase transformations is explored in isolation. Generally and reasonably, poorer reversibility of the phase transformations is expected at a higher sodiation depth (i.e., a higher volume change as compared to pristine Pb). Unexpectedly, we identified that the reversibility between NaPb and Na_9Pb_4 is noticeably poorer than that between Na_9Pb_4 and $Na_{15}Pb_4$, though both phase transformation pairs cause comparable volume changes. Not only can the poorest reversibility of the problematic phase transformations be well supported by the SEM analysis, but it is also well-aligned with the literature regarding the lattice volumes, mechanical properties, electrical resistivity, and kinetic behaviors of these Na-Pb phases. Lastly, we proposed that the Pb electrode should be cycled within a narrower voltage range to largely exclude the problematic phase transformations. It is anticipated that this study can provide guidance for better utilization and development of Pb foil electrodes in SIBs.

Chapter 7: Summary and Future Recommendations

7.1 Thesis Summary

7.1.1 General Summary

This thesis explores different fundamental aspects (e.g., mechanism, kinetics, reversibility) of phase transformations in group IVA alloy anodes, relying on robust electrochemical and structural characterization techniques. The investigation of the Na-Si system (**Chapter 3**) sheds light on the possible factors limiting the sodiation of Si, e.g., sluggish ion transport kinetic, narrow interstitial atomic space, poor electrical conductivity, and weak atomic interaction, etc.

In the deep dive into the sodiation kinetics of the Na-Ge system (**Chapter 4**), the potentiostatic technique reveals the sodiation mechanism (i.e., the interface propagation vs. nucleation-growth mechanism) of the irreversible Ge/$NaGe_4$ and reversible $NaGe_4$/$Na_{1+x}Ge$ phase transformations by analyzing their current-time response characteristics. With the detailed interpretation of important kinetic parameters based on the KJMA model, we further determine the role of sodium diffusion or phase boundary movement on phase transformations, providing an insight into the nature of the Na insertion into Ge. Additionally, two new sodiation models are proposed, illustrating how Na is stored in Ge at low and high C-rates.

In **Chapter 5,** the cell configuration is optimized for the in-situ EIS measurements, which allows us to track the impedance evolution of Sn foil electrodes reliably. The impedance analysis shows how the impedance spectra change with increasing (de-)sodiation depths. With the help of the DRT tool, the contribution of the charge transfer or diffusion resistance to the cell impedance is further quantified at different states, providing an insight into the limiting factors for the phase transformation between low-order Na-Sn phases or high-order Na-Sn phases. Moreover, the frequency-dependent impedance imaginary part is used to more accurately determine the Na diffusivity in Na_xSn (in the order of $\sim 10^{-12}$-10^{-18}), given that the frequency ranges dominated by diffusion and charge transfer overlaps.

The fundamental investigation of the Na-Pb system (**Chapter 6)** reveals the sodiation mechanism of Pb foil electrodes, proceeding by the simultaneous formation of Na-Pb intermediate phases (i.e., $NaPb_3$, NaPb, Na_9Pb_4, $Na_{15}Pb_4$) due to the kinetic limitation. Also, an examination of the reversibility of phase transformations shows the fastest capacity decay in Pb foil electrodes occurs in the transformation between NaPb and Na_9Pb_4, giving new insight into the origin of the poor cycle life of Pb foil anode. In addition, the identification of this problematic transformation offers Pb foil a simple pathway to improve cycling stability, possibly enabling the utilization of the Pb electrode in the future.

Table 7.1 A summary of the electrochemical properties of Na-Sn, Na-Ge, Na-Pb (this thesis), compared to hard carbon and Li-Al alloy electrodes (our group results)

Phase transformations		Gravimetric capacity (areal capacity) / mAh·g^{-1} (mAh·cm^{-2})	Average voltage (vs.Na/Na^{+}) / V	Average voltage in Full cells / V	Electrode-level Gravimetric/Volumetric Energy density / (Wh·g^{-1}/Wh·cm^{-3})	Calculated Volume change / %	Cycle life	Apparent sodium diffusivity at room temperature/ cm^{2}·s^{-1}
Hard carbon/NaC_8 (Baseline)		~350	~0.1 V	~3.20	1.12 / 1.63	~7.4 [208]	2-300	~10^{-10} [208]
Na-Ge	Ge/$NaGe_4$	~90	~0.3	~3.00	0.25 / 1.10	~31.8	NA	~10^{-15}-10^{-12}
	$NaGe_4$/$Na_{1.38}Ge$	~350	~0.12	~3.18	0.82 / 2.53	~181	20	~10^{-12}-10^{-10}
Na-Sn	Sn/$Na_{15}Sn_4$	~720 (16)	~0.1	~3.2	2.74 / 3.92	~381.6	3-4	10^{-12}-10^{-18}
	Sn/NaSn	~ 225 (5)	~0.2	3.10	0.59 /2.50	~106.2	10-20	10^{-15}-10^{-17}
	NaSn/Na_9Sn_4	~230 (5.1)	~0.12	3.18	0.51 / 1.72	~108.4	<10	10^{-13}-10^{-15}
	Na_9Sn_4/$Na_{15}Sn_4$	~339 (6)	~0.06	3.24	0.51 / 1.35	~167.0	<10	10^{-12}-10^{-13}
Na-Pb	Pb/$Na_{15}Pb_4$	~467 (15.7)	~0.1	~3.2	1.56 / 3.78	~358	3-4	NA
	Pb/$NaPb_3$	~34 (1.15)	~0.45	2.85	0.09 / 0.87	~26	150	NA
	$NaPb_3$/NaPb	~73.3 (2.5)	~0.3	3.00	0.20 / 1.21	~74.6	20-30	NA
	NaPb/Na_9Pb_4	~146.6 (5)	~0.13	3.17	0.38 / 1.64	~115.3	3-5	NA
	Na_9Pb_4/$Na_{15}Pb_4$	~213.8 (7.2)	~0.08	3.22	0.49 / 1.69	~142.1	10-20	NA
Li-Al	Al/LiAl	~1007.1(8.16)	~0.35	3.0	2.40 / 4.18	~95	4-5	~10^{-11}
	Li-poor/Li-rich LiAl [209]	~212 (1.7)	0.3	3.05	0.51 / 0.88	~1.4	~200	~10^{-7}
	LiAl/$Li_{2-x}Al$ [145]	994 (8.05)	~0.12	3.28	2.15 / 2.96	~101	100 (60% retention) [145]	~10^{-9}

The energy density of the full cell is calculated, assuming a 3.3 V NVP cathode or 3.4 V LFP. The volumetric capacity of hard carbon is calculated based on the density of 1.5 g·cm^{-3}. For the Na-Ge system, the Ge thin film is used while 30 μm-thick Sn, Pb, and Al foil are used for the Na-Sn, Na-Pb, and Li-Al systems.

7.1.2 Summary of the Electrochemical Properties of M_{IVA} Electrodes

While Si, Ge, Sn, and Pb are from the same groups, they behave slightly differently when alloying with Na electrochemically. Table 7.1 summarizes the electrochemical properties of group IVA alloy anodes in this thesis, in contrast to the most potentially commercialized SIB anode, hard carbon, from the literature and Al foil anodes in LIBs from our group's past research.

(a) The sodiation mechanism

Both crystalline and amorphous Si electrodes show little sodiation capacity even at elevated temperatures experimentally, despite the presence of Na-Si phases theoretically (**Chapter 3**). For the Na-Ge system, Na can only reversibly insert into amorphous Ge, but not crystalline one. The electrochemical sodiation of Ge, occurring through the formation of amorphous $NaGe_4$ followed by the simultaneous formation of NaGe and $NaGe_3$, is found to be kinetically limited, which accounts for a final sodiated phase $Na_{1+x}Ge$ with different stoichiometry at different C-rates or temperatures (**Chapter 4**). Differently, the neighboring Sn and Pb, are both active to Na electrochemically at room temperature, regardless of their crystalline states. Also, the sodiation of Sn and Pb foils undergoes the Na-Sn or Na-Pb intermediate phases with the same stoichiometry and follows similar mechanisms, proceeding by the simultaneous formation of these Na-Sn or Na-Pb phases due to kinetic limitation (**Chapters 5 and 6**). Overall, Ge seems to be the turning point among group IVA elements from unfavorable sodiation to favorable one, and Sn shares more similarity to Pb in the sodium storage mechanism.

(b) Energy density, volume change, diffusivity, and cycle life

The calculated volume expansion of group IVA alloy anodes induced by the sodiation is linearly increased with the increasing Na content (Figure 7.1a). Figure 7.1b summarizes the volumetric energy density of Ge, Sn, and Pb electrodes as a function of volume change. All the electrodes show a similar trend in the volumetric energy density: the larger the volume change is, the higher the energy density is, but the increase rate is decreasing. Intriguingly, the volumetric energy density of these alloy electrodes is close if the same volume change is induced during the (de-)sodiation. For instance, for Sn and Pb foil electrodes, a volumetric energy density of around 3.7 $Wh\cdot cm^{-3}$ will be achieved when the electrodes are fully sodiated to $Na_{15}Sn_4$ or $Na_{15}Sn_4$ phase (i.e., a volume expansion of around 360% is induced). For Ge, the volumetric energy density is close to 3 $Wh\cdot cm^{-3}$ if the sodiation terminates at $Na_{1.38}Ge$. These energy density values for Group IVA alloy electrodes are 2-3 times higher than that of hard carbon.

Taking a look at each pair of phase transformations in Ge, Sn, and Pb electrodes (Table 7.1), the energy density contributed by the transformation between low-order Na-M_{IVA} (M_{IVA}=Ge, Sn, Pb) phases is normally lower than that of hard carbon, and the corresponding volume change is larger than hard carbon. In contrast, for the transformations between low-order Na-M_{IVA} (M_{IVA}=Ge, Sn, Pb) phases, the obtained energy density is higher than hard carbon, but the sodiation-induced volume expansion is significantly larger.

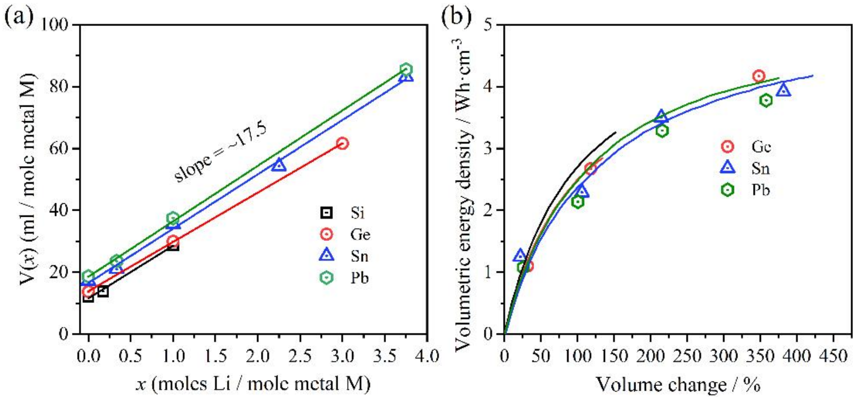

Figure 7.1 (a) Theoretical molar volumes as a function of Na content (*x*) (b) The calculated volumetric energy density of Na_xM as a function of volume change. It is noted that the hollow dots in Figure 7.1b denote the energy density calculated based on the experimental results in this thesis while the solid line denotes the estimated energy density of group IVA alloy anodes obtained from the literature [92].

Regarding the apparent Na diffusivities, the values in the Na-Ge and Na-Sn phases obtained experimentally are lower than that of (sodiated) hard carbon, particularly for the Na-Sn system (Table 7.1). Meanwhile, when compared to the Li-Al systems, their diffusivity values show less competitiveness. Specifically, for the Na-Ge system, sodium seems to diffuse more slowly in the Ge and Na-poorer Na-Ge phases than in the Na-richer Na-Ge phases (**Chapter 4**). This trend is also observed in the Na-Sn system, namely, the faster diffusion kinetic in Na-richer Na-Sn phases than in Na-poorer Na-Sn phases (**Chapter 5**). These diffusion results provide a theoretical basis for the prediction of their rate capability.

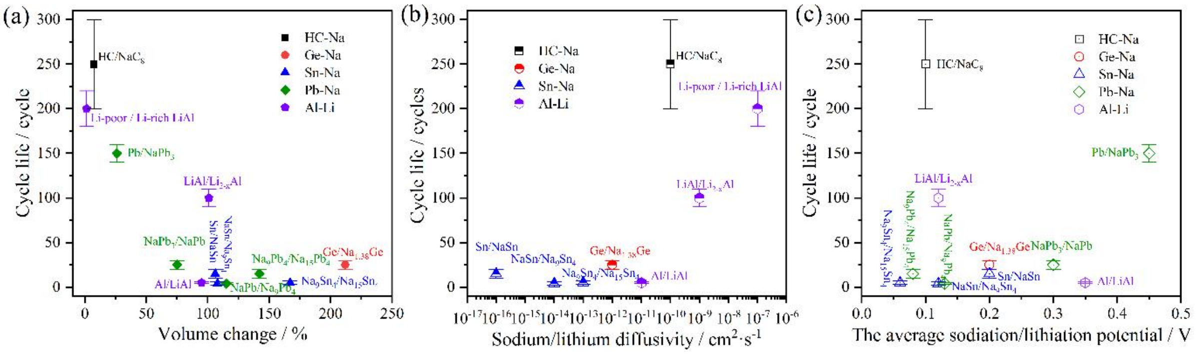

Figure 7.2 Plots of (a) cycle life versus volume change, (b) cycle life versus sodium/lithiation diffusivity, and (c) cycle life versus average sodiation/lithiaion potential (vs. Na/Na^+ or Li/Li^+) of Ge, Sn foil, and Pb foil electrodes (this work) compared to hard carbon (HC) [60] and Al foil electrodes [145, 209] (our group results).

For the cycling performance, the Pb foil electrode can be cycled around 150 times when partly utilized (i.e., limited between $Pb/NaPb_3$ transformation, **Chapter 6**), while the Sn foil stops functioning less than 12 cycles, regardless of full or partial utilization (**Chapter 5**) and Ge electrode can survive about 20 cycles.

Further, the correlation of the cycle life with the volume change, diffusivity, and the sodiation potential of different phase transformations in Ge, Sn, and Pb electrodes is established, as shown in Figure 7.2. Overall, the faster diffusion and the smaller volume change, the better the cycle life. Also, the electrode cycle life shows less dependence on the sodiation or lithiation potential, compared to the volume change and ion diffusivity.

7.2 Future Recommendations

Several possible directions for future work on group IVA alloy anodes, inspired by the research in this thesis, remain to be explored.

The first direction is to thoroughly elucidate the sodiation mechanism and kinetics of these alloy anodes across a broad range of temperatures. The kinetics of Ge electrodes at higher temperatures have been conducted in this thesis, but the temperature influence on the phase transformations of Sn/Pb is not unknown. It is worth systematically investigating the temperature-dependent sodiation kinetics and mechanism of Sn/Pb anodes, particularly considering that some metastable Na-Sn phases (e.g., $NaSn_5$, Na_5Sn_2) and Na-Pb phase (i.e., Na_5Pb_2) might be formed at higher temperatures.

The second direction is to understand the origin of capacity loss on these electrodes with different thicknesses or at different C-rates and temperatures. Pursuing the goal of high energy density batteries necessitates the use of high-loading mass and thicker electrodes (e.g., Ge), which results in sluggish diffusion kinetics. Further, different from the conventional composite electrodes, the dense metallic foil electrodes (e.g., Pb) with no additives have a larger transport kinetic barrier, which limits the electrode performance. Therefore, an understanding of kinetic loss related to the charge transfer or ion diffusion is crucial, since it guides the design and utilization of these alloy foil electrodes to achieve good electrochemical performance. The framework developed in this work is also suitable for these kinetic studies.

The third direction should focus on the performance optimization of these alloy electrodes, particularly Sn/Pb foil electrodes. Sn and Pb are the most promising anodes to be commercialized among the group IVA, given their low cost, abundance, and high gravimetric/volumetric capacity. However, our previous studies show that when partial capacity (2 $mAh \cdot cm^{-2}$) is pursued, the Sn/Pb foil electrode displays a lifetime of below 20 and 60, respectively, which are far below the industrial requirements. One promising strategy for minimizing the capacity loss could be rational design (e.g., nanostructure or surface coating) and composition optimization of Sn-alloy or Pb-alloy foil electrodes. Recently Arumugam Manthiram's group has introduced a new approach to develop nano-structural alloy foils for lithium batteries, which is reported to perform more stable than pure metal foil electrodes [210-212]. This strategy is also expected to be extended to sodium batteries and improve the cycling stability of Sn/Pb alloy foils. In addition, electrolyte optimization may be another possible strategy to enhance electrode stability by forming a stable and uniform SEI layer on the electrode/electrolyte interface.

The final direction is to further explore the sodiation of Si, understanding the true factors limiting sodium inclusion. Although no success has been made on the sodiation of Si at present, Si is also worthy of future attention given its great promise as a SIB anode due to the economic and theoretical capacity metric. As this thesis suggests the narrow interstitial space is one possible factor limiting the Na insertion, strategically introducing the tensile stress into Si to enlarge the interstitial space of Si, e.g., through adjusting the sputtering conditions (for Si thin film) or annealing or mechanical stretching, might be a feasible way to enable the sodiation of Si. In addition, defective engineering (e.g., mechanically rolling or incorporating the conductive elements) could be also possible to facilitate the sodium incorporation into Si by lowering the nucleation barrier.

References

1. N. Khan, S. Dilshad, R. Khalid, A. R. Kalair, and N. Abas, *Energy Storage,* **1** (3), e49 (2019).
2. J. Mitali, S. Dhinakaran, and A. Mohamad, *Energy Storage and Saving,* **1** (3), 166-216 (2022).
3. C. Delmas, *Advanced Energy Materials,* **8** (17), 1703137 (2018).
4. A. G. Olabi, C. Onumaegbu, T. Wilberforce, M. Ramadan, M. A. Abdelkareem, and A. H. Al – Alami, *Energy,* **214** (2021).
5. S. O. Amrouche, D. Rekioua, T. Rekioua, and S. Bacha, *International journal of hydrogen energy,* **41** (45), 20914-20927 (2016).
6. Q. Abbas, M. Mirzaeian, M. R. Hunt, P. Hall, and R. Raza, *Energies,* **13** (21), 5847 (2020).
7. T. Zheng, (2021).
8. J. Garche and L. Jürissen, *The Electrochemical Society Interface,* **24** (2), 39 (2015).
9. R. Nigam, K. D. Verma, T. Pal, and K. K. Kar, *Handbook of Nanocomposite Supercapacitor Materials II: Performance,* 463-481 (2020).
10. P. P. Lopes and V. R. Stamenkovic, *Science,* **369** (6506), 923-924 (2020).
11. S. Sarmah, Lakhanlal, B. K. Kakati, and D. Deka, *Wiley Interdisciplinary Reviews: Energy and Environment,* **12** (2), e461 (2023).
12. J.-M. Tarascon, *Joule,* **4** (8), 1616-1620 (2020).
13. Z. Šimić, D. Topić, G. Knežević, and D. Pelin, *International journal of electrical and computer engineering systems,* **12** (1), 53-65 (2021).
14. K. C. Divya and J. Østergaard, *Electric power systems research,* **79** (4), 511-520 (2009).
15. W. Johnson and W. Worrell, *Synthetic Metals,* **4** (3), 225-248 (1982).
16. K. Chayambuka, G. Mulder, D. L. Danilov, and P. H. Notten, *Advanced energy materials,* **10** (38), 2001310 (2020).
17. C. Delmas, J.-J. Braconnier, C. Fouassier, and P. Hagenmuller, *Solid State Ionics,* **3** 165-169 (1981).
18. K. Mizushima, P. Jones, P. Wiseman, and J. B. Goodenough, *Materials Research Bulletin,* **15** (6), 783-789 (1980).
19. A. Mendiboure, C. Delmas, and P. Hagenmuller, *Journal of Solid State Chemistry,* **57** (3), 323-331 (1985).
20. J. Braconnier, C. Delmas, and P. Hagenmuller, *Materials Research Bulletin,* **17** (8), 993-1000 (1982).
21. N. Yabuuchi, K. Kubota, M. Dahbi, and S. Komaba, *Chemical reviews,* **114** (23), 11636-11682 (2014).
22. D. Stevens and J. Dahn, *Journal of the Electrochemical Society,* **147** (4), 1271 (2000).
23. D. Stevens and J. Dahn, *Journal of The Electrochemical Society,* **148** (8), A803 (2001).
24. K. Chayambuka, G. Mulder, D. L. Danilov, and P. H. Notten, *Advanced Energy Materials,* **8** (16), 1800079 (2018).
25. Y. Gao, H. Zhang, J. Peng, L. Li, Y. Xiao, L. Li, Y. Liu, Y. Qiao, and S. L. Chou, *Carbon Energy,* e464 (2024).
26. J. Deng, W. B. Luo, S. L. Chou, H. K. Liu, and S. X. Dou, *Advanced Energy Materials,* **8** (4), 1701428 (2018).
27. K. Chayambuka, M. Jiang, G. Mulder, D. L. Danilov, and P. H. Notten, *Electrochimica Acta,* **404** 139726 (2022).

28. A. Bauer, J. Song, S. Vail, W. Pan, J. Barker, and Y. Lu, *Advanced Energy Materials,* **8** (17), 1702869 (2018).

29. R. Xiaohui, L. Yaxiang, Q. Xingguo, Z. Quan, K. Weihe, T. Kun, C. Liquan, and H. Yongsheng, *Energy Storage Science and Technology,* **9** (2), 515 (2020).

30. Y. S. Hu, S. Komaba, M. Forsyth, C. Johnson, and T. Rojo, Vol. 3, p. 1900184. Wiley Online Library, 2019.

31. K. Abraham, *ACS Energy Letters,* **5** (11), 3544-3547 (2020).

32. L. Xiang, J. Jin, J. Zhang, C. Ma, B. Xiang, and W. Sun, *in* "IOP Conference Series: Earth and Environmental Science", Vol. 898, p. 012020. IOP Publishing, 2021.

33. D. J. MacKay, *Sustainable Energy-without the hot air*, Bloomsbury Publishing (2016).

34. J. Yin, H. Lin, J. Shi, Z. Lin, J. Bao, Y. Wang, X. Lin, Y. Qin, X. Qiu, and W. Zhang, *Electrochemical Energy Reviews,* **5** (3), 2 (2022).

35. J. Besenhard, *Carbon,* **14** (2), 111-115 (1976).

36. M. S. Dresselhaus and G. Dresselhaus, *Advances in Physics,* **30** (2), 139-326 (1981).

37. Y. Li, Y. Lu, P. Adelhelm, M.-M. Titirici, and Y.-S. Hu, *Chemical Society Reviews,* **48** (17), 4655-4687 (2019).

38. M.-M. Titirici, P. Adelhelm, and Y.-S. Hu, *Sodium-Ion Batteries: Materials, Characterization, and Technology, 2 Volumes*, John Wiley & Sons (2022).

39. S. Qiao, Q. Zhou, M. Ma, H. K. Liu, S. X. Dou, and S. Chong, *ACS nano,* **17** (12), 11220-11252 (2023).

40. B. Jache and P. Adelhelm, *Angewandte Chemie International Edition,* **53** (38), 10169-10173 (2014).

41. S. C. Jung, Y.-J. Kang, and Y.-K. Han, *Nano Energy,* **34** 456-462 (2017).

42. J. Park, Z. L. Xu, G. Yoon, S. K. Park, J. Wang, H. Hyun, H. Park, J. Lim, Y. J. Ko, and Y. S. Yun, *Advanced materials,* **32** (4), 1904411 (2020).

43. H. Kim, J. Hong, Y. U. Park, J. Kim, I. Hwang, and K. Kang, *Advanced Functional Materials,* **25** (4), 534-541 (2015).

44. I. Hasa, X. Dou, D. Buchholz, Y. Shao-Horn, J. Hassoun, S. Passerini, and B. Scrosati, *Journal of Power Sources,* **310** 26-31 (2016).

45. A. P. Cohn, K. Share, R. Carter, L. Oakes, and C. L. Pint, *Nano letters,* **16** (1), 543-548 (2016).

46. Z. Zhu, F. Cheng, Z. Hu, Z. Niu, and J. Chen, *Journal of Power Sources,* **293** 626-634 (2015).

47. W. Xiao, Q. Sun, J. Liu, B. Xiao, P.-A. Glans, J. Li, R. Li, J. Guo, W. Yang, and T.-K. Sham, *Nano Research,* **10** 4378-4387 (2017).

48. Z. L. Xu, J. Park, G. Yoon, H. Kim, and K. Kang, *Small Methods,* **3** (4), 1800227 (2019).

49. M. Goktas, C. Bolli, E. J. Berg, P. Novák, K. Pollok, F. Langenhorst, M. v. Roeder, O. Lenchuk, D. Mollenhauer, and P. Adelhelm, *Advanced Energy Materials,* **8** (16), 1702724 (2018).

50. B. Jache, J. O. Binder, T. Abe, and P. Adelhelm, *Physical Chemistry Chemical Physics,* **18** (21), 14299-14316 (2016).

51. H. Kim, J. C. Hyun, D. H. Kim, J. H. Kwak, J. B. Lee, J. H. Moon, J. Choi, H. D. Lim, S. J. Yang, and H. M. Jin, *Advanced Materials,* **35** (12), 2209128 (2023).

52. F. Xie, Z. Xu, Z. Guo, and M.-M. Titirici, *Progress in Energy,* **2** (4), 042002 (2020).

53. Y. Cao, L. Xiao, M. L. Sushko, W. Wang, B. Schwenzer, J. Xiao, Z. Nie, L. V. Saraf, Z. Yang, and J. Liu, *Nano letters,* **12** (7), 3783-3787 (2012).

54. J. Ding, H. Wang, Z. Li, A. Kohandehghan, K. Cui, Z. Xu, B. Zahiri, X. Tan, E. M. Lotfabad, and B. C. Olsen, *ACS nano,* **7** (12), 11004-11015 (2013).

55. B. Zhang, C. M. Ghimbeu, C. Laberty, C. Vix - Guterl, and J. m. Tarascon, *Advanced Energy Materials,* **6** (1), 1501588 (2016).

56. Y. Li, Y. S. Hu, M. M. Titirici, L. Chen, and X. Huang, *Advanced energy materials,* **6** (18), 1600659 (2016).

57. C. Bommier, T. W. Surta, M. Dolgos, and X. Ji, *Nano Letters,* **15** (9), 5888-5892 (2015).

58. Y. Yang, C. Wu, X. X. He, J. Zhao, Z. Yang, L. Li, X. Wu, L. Li, and S. L. Chou, *Advanced Functional Materials,* **34** (5), 2302277 (2024).

59. M. Zhang, Y. Li, F. Wu, Y. Bai, and C. Wu, *Nano Energy,* **82** 105738 (2021).

60. N. Sun, H. Liu, and B. Xu, *Journal of materials chemistry a,* **3** (41), 20560-20566 (2015).

61. H. Tan, D. Chen, X. Rui, and Y. Yu, *Advanced Functional Materials,* **29** (14), 1808745 (2019).

62. A. A. Yaroshevsky, *Geochemistry International,* **44** 48-55 (2006).

63. K. Song, C. Liu, L. Mi, S. Chou, W. Chen, and C. Shen, *Small,* **17** (9), 1903194 (2021).

64. Y. R. Lim, F. Shojaei, K. Park, C. S. Jung, J. Park, W. I. Cho, and H. S. Kang, *Nanoscale,* **10** (15), 7047-7057 (2018).

65. J. Zhang, Y.-X. Yin, and Y.-G. Guo, *ACS Applied Materials & Interfaces,* **7** (50), 27838-27844 (2015).

66. Y. Kim, K. H. Ha, S. M. Oh, and K. T. Lee, *Chemistry–A European Journal,* **20** (38), 11980-11992 (2014).

67. R. Le Ruyet, J. Kullgren, A. J. Naylor, and R. Younesi, *Journal of The Electrochemical Society,* **169** (6), (2022).

68. M. Obrovac, L. Christensen, D. B. Le, and J. R. Dahn, *Journal of The Electrochemical Society,* **154** (9), A849 (2007).

69. J. Ni, L. Li, and J. Lu, *ACS Energy Letters,* **3** (5), 1137-1144 (2018).

70. Y. Zhu, Y. Wen, X. Fan, T. Gao, F. Han, C. Luo, S.-C. Liou, and C. Wang, *ACS nano,* **9** (3), 3254-3264 (2015).

71. Y. Fu, Q. Wei, G. Zhang, and S. Sun, *Advanced Energy Materials,* **8** (13), 1703058 (2018).

72. S. Sarkar and S. C. Peter, *Journal of Materials Chemistry A,* **9** (9), 5164-5196 (2021).

73. R. Shao, Z. Sun, L. Wang, J. Pan, L. Yi, Y. Zhang, J. Han, Z. Yao, J. Li, and Z. Wen, *Angewandte Chemie,* **136** (11), e202320183 (2024).

74. M. Lao, Y. Zhang, W. Luo, Q. Yan, W. Sun, and S. X. Dou, *Advanced Materials,* **29** (48), 1700622 (2017).

75. A. Darwiche, C. Marino, M. T. Sougrati, B. Fraisse, L. Stievano, and L. Monconduit, *Journal of the American Chemical Society,* **134** (51), 20805-20811 (2012).

76. J. He, Y. Wei, T. Zhai, and H. Li, *Materials Chemistry Frontiers,* **2** (3), 437-455 (2018).

77. J. Sottmann, M. Herrmann, P. Vajeeston, Y. Hu, A. Ruud, C. Drathen, H. Emerich, H. Fjellvag, and D. S. Wragg, *Chemistry of Materials,* **28** (8), 2750-2756 (2016).

78. M. Lao, Y. Zhang, W. Luo, Q. Yan, W. Sun, and S. X. Dou, *Adv Mater,* **29** (48), (2017).

79. L. Ellis, B. Wilkes, T. Hatchard, and M. Obrovac, *Journal of The Electrochemical Society,* **161** (3), A416 (2014).

80. J. Zhou, J. Chen, M. Chen, J. Wang, X. Liu, B. Wei, Z. Wang, J. Li, L. Gu, and Q. Zhang, *Advanced Materials,* **31** (12), 1807874 (2019).

81. Z. Hu, X. Li, J. Qu, Z. Zhao, H. Xie, and H. Yin, *Journal of Power Sources,* **496** 229830 (2021).

82. Y. H. Kim, J. H. An, S. Y. Kim, X. Li, E. J. Song, J. H. Park, K. Y. Chung, Y. S. Choi, D. O. Scanlon, and H. J. Ahn, *Advanced Materials,* **34** (27), 2201446 (2022).

83. X. Li, J. Ni, S. Savilov, and L. Li, *Chemistry–A European Journal,* **24** (52), 13719-13727 (2018).

84. S.-M. Zheng, Y.-R. Tian, Y.-X. Liu, S. Wang, C.-Q. Hu, B. Wang, and K.-M. Wang, *Rare Metals,* **40** 272-289 (2021).

85. H. Xie, W. P. Kalisvaart, B. C. Olsen, E. J. Luber, D. Mitlin, and J. M. Buriak, *Journal of materials chemistry A,* **5** (20), 9661-9670 (2017).

86. Y. Zhu, C. Wang, Z. Cheng, Q. Yao, J. Su, B. Chen, J. Yang, and Y. Qian, *Chemical Communications,* **58** (33), 5140-5143 (2022).

87. S. C. Jung, D. S. Jung, J. W. Choi, and Y.-K. Han, *The journal of physical chemistry letters,* **5** (7), 1283-1288 (2014).

88. S. C. Jung, H.-J. Kim, Y.-J. Kang, and Y.-K. Han, *Journal of Alloys and Compounds,* **688** 158-163 (2016).

89. P. R. Abel, Y.-M. Lin, T. de Souza, C.-Y. Chou, A. Gupta, J. B. Goodenough, G. S. Hwang, A. Heller, and C. B. Mullins, *The Journal of Physical Chemistry C,* **117** (37), 18885-18890 (2013).

90. X. Lu, E. R. Adkins, Y. He, L. Zhong, L. Luo, S. X. Mao, C.-M. Wang, and B. A. Korgel, *Chemistry of Materials,* **28** (4), 1236-1242 (2016).

91. W. Hume-Rothery, *Journal of the Chemical Society (Resumed),* 947-963 (1928).

92. V. L. Chevrier and G. Ceder, *Journal of The Electrochemical Society,* **158** (9), (2011).

93. L. D. Ellis, T. D. Hatchard, and M. N. Obrovac, *Journal of the Electrochemical Society,* **159** (11), A1801 (2012).

94. L. Baggetto, P. Ganesh, R. P. Meisner, R. R. Unocic, J.-C. Jumas, C. A. Bridges, and G. M. Veith, *Journal of power sources,* **234** 48-59 (2013).

95. J. W. Wang, X. H. Liu, S. X. Mao, and J. Y. Huang, *Nano letters,* **12** (11), 5897-5902 (2012).

96. Z. Li, J. Ding, and D. Mitlin, *Accounts of chemical research,* **48** (6), 1657-1665 (2015).

97. A. Darwiche, R. Dugas, B. Fraisse, and L. Monconduit, *Journal of Power Sources,* **304** 1-8 (2016).

98. J. Songster and A. Pelton, *Journal of phase equilibria,* **13** 67-69 (1992).

99. J. Sangster and A. Pelton, *Journal of phase equilibria,* **18** (3), 295 (1997).

100. J. Park, J. Han, J. Gim, J. Garcia, H. Iddir, S. Ahmed, G.-L. Xu, K. Amine, C. Johnson, and Y. Jung, *Chemistry of Materials,* (2023).

101. C.-Y. Chou, M. Lee, and G. S. Hwang, *The Journal of Physical Chemistry C,* **119** (27), 14843-14850 (2015).

102. Y.-S. Choi, Y.-W. Byeon, J.-P. Ahn, and J.-C. Lee, *Nano Letters,* **17** (2), 679-686 (2017).

103. W. Calaway and M.-L. Saboungi, *Journal of Physics F: Metal Physics,* **13** (6), 1213 (1983).

104. S. Sarkar, A. Verma, and P. P. Mukherjee, *Journal of The Electrochemical Society,* **168** (9), 090550

(2021).

105. M. Mortazavi, J. Deng, V. B. Shenoy, and N. V. Medhekar, *Journal of Power Sources,* **225** 207-214 (2013).

106. A. Kohandehghan, K. Cui, M. Kupsta, J. Ding, E. Memarzadeh Lotfabad, W. P. Kalisvaart, and D. Mitlin, *Nano Letters,* **14** (10), 5873-5882 (2014).

107. Y. W. Byeon, J. P. Ahn, and J. C. Lee, *Small,* **16** (52), e2004868 (2020).

108. J.-H. Park, Y.-S. Choi, Y.-W. Byeon, J.-P. Ahn, and J.-C. Lee, *Nano Energy,* **65** 104041 (2019).

109. Y. Deng, J. Zheng, Q. Zhao, J. Yin, P. Biswal, Y. Hibi, S. Jin, and L. A. Archer, *Small,* **18** (37), 2203409 (2022).

110. G. Oyama, Y. Yamada, R.-i. Natsui, S.-i. Nishimura, and A. Yamada, *The Journal of Physical Chemistry C,* **116** (13), 7306-7311 (2012).

111. J. Miao, B. Wang, and C. V. Thompson, *Physical Review Materials,* **4** (4), 043608 (2020).

112. J. Miao, B. Wang, and C. V. Thompson, *Journal of The Electrochemical Society,* **167** (9), (2020).

113. Y. Orikasa, T. Maeda, Y. Koyama, T. Minato, H. Murayama, K. Fukuda, H. Tanida, H. Arai, E. Matsubara, Y. Uchimoto, and Z. Ogumi, *Journal of The Electrochemical Society,* **160** (5), A3061-A3065 (2013).

114. J. Miao. Massachusetts Institute of Technology, 2018.

115. A. C. Lazanas and M. I. Prodromidis, *ACS Meas Sci Au,* **3** (3), 162-193 (2023).

116. Y. Barsukov and J. R. Macdonald, *Characterization of materials,* **2** 898-913 (2012).

117. A. C. Lazanas and M. I. Prodromidis, *ACS Measurement Science Au,* **3** (3), 162-193 (2023).

118. R. Morasch, B. Suthar, and H. A. Gasteiger, *Journal of The Electrochemical Society,* **167** (10), 100540 (2020).

119. M. Shi, Z. Chen, and J. Sun, *Cement and Concrete Research,* **29** (7), 1111-1115 (1999).

120. Y. Lu, C.-Z. Zhao, R. Zhang, H. Yuan, L.-P. Hou, Z.-H. Fu, X. Chen, J.-Q. Huang, and Q. Zhang, *Science advances,* **7** (38), eabi5520 (2021).

121. S. Dierickx, A. Weber, and E. Ivers-Tiffée, *Electrochimica Acta,* **355** 136764 (2020).

122. Y. Zhang, Y. Chen, M. Li, M. Yan, M. Ni, and C. Xia, *Journal of power sources,* **308** 1-6 (2016).

123. B. A. Boukamp, *Electrochimica acta,* **154** 35-46 (2015).

124. F. Ciucci and C. Chen, *Electrochimica Acta,* **167** 439-454 (2015).

125. H. Morito, T. Yamada, T. Ikeda, and H. Yamane, *Journal of alloys and compounds,* **480** (2), 723-726 (2009).

126. S. Komaba, Y. Matsuura, T. Ishikawa, N. Yabuuchi, W. Murata, and S. Kuze, *Electrochemistry Communications,* **21** 65-68 (2012).

127. S. Y. Sayed, W. P. Kalisvaart, E. J. Luber, B. C. Olsen, and J. M. Buriak, *ACS Applied Energy Materials,* **3** (10), 9950-9962 (2020).

128. F. Legrain, O. I. Malyi, and S. Manzhos, *Computational materials science,* **94** 214-217 (2014).

129. X. Yi, W. Li, Z. Li, P. Zhou, Z. Ma, and L. Sun, *Journal of Materials Chemistry C,* **7** (48), 15375-15381 (2019).

130. Z. Di, R. Okuyama, E. Nomura, and Y. Matsumaru, *Journal of Power Sources;(Switzerland),* **47** (1994).

131. L. Xijiang, R. Xiong, S. Pengcheng, and Z. Di, *Materials Science and Engineering: A,* **280** (1), 54-57 (2000).

132. M. H. Tahmasebi, D. Kramer, H. Geßwein, T. Zheng, K.-C. Leung, B. T. W. Lo, R. Mönig, and S. T. Boles, *Journal of materials chemistry A,* **8** (9), 4877-4888 (2020).

133. M. Shimizu, H. Usui, K. Fujiwara, K. Yamane, and H. Sakaguchi, *Journal of Alloys and Compounds,* **640** 440-443 (2015).

134. Z. Hu, S. Zhang, C. Zhang, and G. Cui, *Coordination Chemistry Reviews,* **326** 34-85 (2016).

135. G.-K. Sung, K.-H. Nam, J.-H. Choi, and C.-M. Park, *Electrochimica Acta,* **331** (2020).

136. H. Shen, Z. Ma, B. Yang, B. Guo, Y. Lyu, P. Wang, H. Yang, Q. Li, H. Wang, and Z. Liu, *Journal of Power Sources,* **433** 126682 (2019).

137. L. Hu, C. Shang, L. Huang, X. Wang, and G. Zhou, *Ionics,* **26** (2), 719-726 (2019).

138. T. L. Kulova, A. M. Skundin, I. y. M. Gavrilin, Y. O. Kudryashova, I. K. Martynova, and S. A. Novikova, *Batteries,* **8** (8), 98 (2022).

139. C. Yue, Y. Yu, S. Sun, X. He, B. Chen, W. Lin, B. Xu, M. Zheng, S. Wu, J. Li, J. Kang, and L. Lin, *Advanced Functional Materials,* **25** (9), 1386-1392 (2015).

140. W. Wei, Y. Zhang, L. Liang, K. Wang, Q. Zhou, Y. Zhou, and H. Wang, *Materials Chemistry Frontiers,* **5** (21), 7778-7786 (2021).

141. L. Baggetto, J. K. Keum, J. F. Browning, and G. M. Veith, *Electrochemistry Communications,* **34** 41-44 (2013).

142. J. Miao and C. V. Thompson, *Journal of The Electrochemical Society,* **165** (3), A650 (2018).

143. Y. Jiang, G. Offer, J. Jiang, M. Marinescu, and H. Wang, *Journal of The Electrochemical Society,* **167** (13), 130533 (2020).

144. I. A. Courtney, J. Tse, O. Mao, J. Hafner, and J. R. Dahn, *Physical Review B,* **58** (23), 15583 (1998).

145. T. Zheng, J. Zhang, W. Jin, and S. T. Boles, *ACS Applied Energy Materials,* **6** (3), 1845-1852 (2023).

146. S. Rakshit, A. S. Pakhare, O. Ruiz, M. R. Khoshi, E. Detsi, H. He, V. A. Sethuraman, and S. P. V. Nadimpalli, *Journal of The Electrochemical Society,* **168** (1), (2021).

147. F. Shi, Z. Song, P. N. Ross, G. A. Somorjai, R. O. Ritchie, and K. Komvopoulos, *Nature communications,* **7** (1), 11886 (2016).

148. T. Zheng, D. Kramer, M. H. Tahmasebi, R. Mönig, and S. T. Boles, *ChemSusChem,* **13** (22), 5910-5920 (2020).

149. Y.-W. Byeon, Y.-S. Choi, J.-P. Ahn, and J.-C. Lee, *Journal of Power Sources,* **343** 513-519 (2017).

150. P. Hubberstey and R. J. Pulham, *Journal of the Chemical Society, Faraday Transactions 1: Physical Chemistry in Condensed Phases,* **70** 1631-1635 (1974).

151. T. Zheng, D. Kramer, M. H. Tahmasebi, R. Mönig, and S. T. Boles, *ChemSusChem,* **13** (5), 974-985 (2020).

152. P.-C. Tsai, B. Wen, M. Wolfman, M.-J. Choe, M. S. Pan, L. Su, K. Thornton, J. Cabana, and Y.-M. Chiang, *Energy & Environmental Science,* **11** (4), 860-871 (2018).

153. G. Pekar and A. Singaevsky, *Materials Science in Semiconductor Processing,* **64** 10-15 (2017).

154. R. Newman. IOP Publishing, 1978.

155. W. Liu, X. Chen, C. Zhang, H. Xu, X. Sun, Y. Zheng, Y. Yu, S. Li, Y. Huang, and J. Li, *ACS applied*

materials & interfaces, **11** (26), 23207-23212 (2019).

156. C. Kim, H. Kim, M. K. Sadan, M. Jeon, G. Cho, J. Ahn, K. Kim, K. Cho, and H. Ahn, *Small,* **17** (50), e2102618 (2021).
157. Y.-S. Choi, Y.-W. Byeon, J.-P. Ahn, and J.-C. Lee, *Journal of Materials Chemistry A,* **6** (20), 9428-9436 (2018).
158. Y. Zhu and C. Wang, *The Journal of Physical Chemistry C,* **114** (6), 2830-2841 (2010).
159. T. Li, U. Gulzar, X. Bai, M. Lenocini, M. Prato, K. E. Aifantis, C. Capiglia, and R. Proietti Zaccaria, *ACS Applied Energy Materials,* **2** (1), 860-866 (2019).
160. H. V. Anne. Universidad del País Vasco-Euskal Herriko Unibertsitatea, 2019.
161. C. Trejo, K. Scanlan, and A. Manthiram, *Journal of The Electrochemical Society,* **171** (4), (2024).
162. J. Song, H. Lee, Y. Wang, and C. Wan, *Journal of Power Sources,* **111** (2), 255-267 (2002).
163. S. Oswald, D. Pritzl, M. Wetjen, and H. A. Gasteiger, *Journal of The Electrochemical Society,* **167** (10), 100511 (2020).
164. C. Ho, I. Raistrick, and R. Huggins, *Journal of The Electrochemical Society,* **127** (2), 343 (1980).
165. R. Ruess, S. Schweidler, H. Hemmelmann, G. Conforto, A. Bielefeld, D. A. Weber, J. Sann, M. T. Elm, and J. Janek, *Journal of The Electrochemical Society,* **167** (10), 100532 (2020).
166. L. Baggetto, P. Ganesh, C.-N. Sun, R. A. Meisner, T. A. Zawodzinski, and G. M. Veith, *Journal of Materials Chemistry A,* **1** (27), 7985-7994 (2013).
167. A. Skundin, D. Gryzlov, T. Kulova, Y. Kudryashova, and A. Kuz'mina, *International Journal of Electrochemical Science,* **15** (2), 1622-1633 (2020).
168. C. Wang, D. Du, M. Song, Y. Wang, and F. Li, *Advanced Energy Materials,* **9** (16), (2019).
169. R. Amatya and R. Ram, *Journal of electronic materials,* **41** 1011-1019 (2012).
170. J. Eaves-Rathert, K. Moyer-Vanderburgh, K. Wolfe, M. Zohair, and C. L. Pint, *Energy Storage Materials,* (2022).
171. C. Kim, H. Kim, M. K. Sadan, M. Jeon, G.-B. Cho, T.-H. Nam, K.-K. Cho, J.-H. Ahn, and H.-J. Ahn, *Journal of Alloys and Compounds,* **886** 161240 (2021).
172. T. Jow, L. Shacklette, M. Maxfield, and D. Vernick, *Journal of The Electrochemical Society,* **134** (7), 1730 (1987).
173. T. Zheng and S. T. Boles, *ACS omega,* **7** (42), 37867-37872 (2022).
174. B. T. Heligman and A. Manthiram, *ACS Energy Letters,* **6** (8), 2666-2672 (2021).
175. C. Wang, Y. Meng, G. Ceder, and Y. Li, *Journal of the Electrochemical Society,* **155** (9), A615 (2008).
176. T. Li, U. Gulzar, R. Proietti Zaccaria, C. Capiglia, S. A. Hackney, and K. Aifantis, *The Journal of Physical Chemistry C,* **123** (24), 15244-15250 (2019).
177. S. C. DeCaluwe, B.-M. Dhar, L. Huang, Y. He, K. Yang, J. P. Owejan, Y. Zhao, A. A. Talin, J. Dura, and H. Wang, *Physical Chemistry Chemical Physics,* **17** (17), 11301-11312 (2015).
178. B. Pandit, M. T. Sougrati, B. Fraisse, and L. Monconduit, *Nano Energy,* **95** 107010 (2022).
179. C. v. d. Marel, A. B. v. Oosten, W. Gertsma, and W. v. d. Lugt, *Journal of Physics F: Metal Physics,* **12** (10), 2349-2361 (1982).
180. K. Dong, H. Markötter, F. Sun, A. Hilger, N. Kardjilov, J. Banhart, and I. Manke, *ChemSusChem,* **12** (1), 261-269 (2019).

181. X. Yan, F. Ye, Y. Zhang, L. Lin, B. Sa, F. Liu, J. Li, L. Wang, J. Lin, and Q. Xie, *Chemical Engineering Journal,* **440** 135827 (2022).

182. B. Horstmann, J. Shi, R. Amine, M. Werres, X. He, H. Jia, F. Hausen, I. Cekic-Laskovic, S. Wiemers-Meyer, and J. Lopez, *Energy & Environmental Science,* **14** (10), 5289-5314 (2021).

183. S. W. Lee, M. T. McDowell, J. W. Choi, and Y. Cui, *Nano letters,* **11** (7), 3034-3039 (2011).

184. T. Zheng, X. Wang, E. Jain, D. Kramer, R. Mönig, M. Seita, and S. T. Boles, *Scripta Materialia,* **188** 164-168 (2020).

185. M. Pharr, K. Zhao, X. Wang, Z. Suo, and J. J. Vlassak, *Nano letters,* **12** (9), 5039-5047 (2012).

186. Y.-S. Choi, J.-H. Park, J.-P. Ahn, and J.-C. Lee, *Chemistry of Materials,* **31** (5), 1696-1703 (2019).

187. G. Lamprecht, L. Dicks, and P. Crowther, *The Journal of Physical Chemistry,* **72** (5), 1439-1441 (1968).

188. J. Zhang, T. Zheng, K.-w. E. Cheng, K.-h. Lam, and S. T. Boles, *Journal of The Electrochemical Society,* **170** (10), 100518 (2023).

189. V. A. Sethuraman, V. Srinivasan, A. F. Bower, and P. R. Guduru, *Journal of the Electrochemical Society,* **157** (11), A1253 (2010).

190. D. A. Santos, J. L. Andrews, Y. Bai, P. Stein, Y. Luo, Y. Zhang, M. Pharr, B.-X. Xu, and S. Banerjee, *Materials Horizons,* **7** (12), 3275-3290 (2020).

191. Y. H. Kim, J. H. An, S. Y. Kim, X. Li, E. J. Song, J. H. Park, K. Y. Chung, Y. S. Choi, D. O. Scanlon, H. J. Ahn, and J. C. Lee, *Adv Mater,* **34** (27), e2201446 (2022).

192. P. J. Crowley, K. P. Scanlan, and A. Manthiram, *Journal of Power Sources,* **546** 231973 (2022).

193. Y. Li, X. Zheng, Z. Cao, Y. Wang, Y. Wang, L. Lv, W. Huang, Y. Huang, and H. Zheng, *Energy Storage Materials,* **55** 660-668 (2023).

194. J. Erlebacher, M. J. Aziz, A. Karma, N. Dimitrov, and K. Sieradzki, *nature,* **410** (6827), 450-453 (2001).

195. X. Lu, T. D. Bogart, M. Gu, C. Wang, and B. A. Korgel, *The Journal of Physical Chemistry C,* **119** (38), 21889-21895 (2015).

196. T. D. Bogart, X. Lu, M. Gu, C. Wang, and B. A. Korgel, *RSC advances,* **4** (79), 42022-42028 (2014).

197. Y. Cao, Y. Liu, D. Zhao, X. Xia, L. Zhang, J. Zhang, H. Yang, and Y. Xia, *ACS Sustainable Chemistry & Engineering,* **8** (3), 1380-1387 (2019).

198. A. Ponrouch, R. Dedryvère, D. Monti, A. E. Demet, J. M. Ateba Mba, L. Croguennec, C. Masquelier, P. Johansson, and M. R. Palacín, *Energy & Environmental Science,* **6** (8), (2013).

199. L. Mu, S. Xu, Y. Li, Y. S. Hu, H. Li, L. Chen, and X. Huang, *Advanced materials,* **27** (43), 6928-6933 (2015).

200. M. Song, C. Wang, D. Du, F. Li, and J. Chen, *Science China Chemistry,* **62** 616-621 (2019).

201. N. Wang, Z. Bai, Y. Qian, and J. Yang, *Adv Mater,* **28** (21), 4126-4133 (2016).

202. (!!! INVALID CITATION !!! 61).

203. Z.-L. Xu, G. Yoon, K.-Y. Park, H. Park, O. Tamwattana, S. Joo Kim, W. M. Seong, and K. Kang, *Nature Communications,* **10** (1), 2598 (2019).

204. Z. Cao and B. Wei, *Energy Environ. Sci.,* **6** (11), 3183-3201 (2013).

205. A. Rudola, A. J. Rennie, R. Heap, S. S. Meysami, A. Lowbridge, F. Mazzali, R. Sayers, C. J. Wright,

and J. Barker, *Journal of Materials Chemistry A,* **9** (13), 8279-8302 (2021).

206. H. Li, *Joule,* **3** (4), 911-914 (2019).

207. I. Hasa, S. Mariyappan, D. Saurel, P. Adelhelm, A. Y. Koposov, C. Masquelier, L. Croguennec, and M. Casas-Cabanas, *Journal of Power Sources,* **482** 228872 (2021).

208. J. Li, C. Peng, J. Wang, J. Li, and H. Zhang, *Diamond and Related Materials,* **129** 109355 (2022).

209. J. Zhang, T. Zheng, K.-h. Lam, and S. T. Boles, *Electrochimica Acta,* **456** 142437 (2023).

210. B. T. Heligman, K. J. Kreder, and A. Manthiram, *Joule,* **3** (4), 1051-1063 (2019).

211. K. J. Kreder III, B. T. Heligman, and A. Manthiram, *ACS Energy Letters,* **2** (10), 2422-2423 (2017).

212. B. T. Heligman, K. P. Scanlan, and A. Manthiram, *ACS Applied Materials & Interfaces,* **14** (9), 11408-11414 (2022).